

3-21-2013

Three Dimensional Positron Annihilation Momentum Spectroscopy of Lithium Tetraborate Crystals

Stefan B. Fagan-Kelly

Follow this and additional works at: <https://scholar.afit.edu/etd>

Part of the [Nuclear Commons](#)

Recommended Citation

Fagan-Kelly, Stefan B., "Three Dimensional Positron Annihilation Momentum Spectroscopy of Lithium Tetraborate Crystals" (2013).
Theses and Dissertations. 924.
<https://scholar.afit.edu/etd/924>

This Thesis is brought to you for free and open access by the Student Graduate Works at AFIT Scholar. It has been accepted for inclusion in Theses and Dissertations by an authorized administrator of AFIT Scholar. For more information, please contact richard.mansfield@afit.edu.



THREE DIMENSIONAL POSITRON ANNIHILATION MOMENTUM
SPECTROSCOPY OF LITHIUM TETRABORATE CRYSTALS

THESIS

Stefan B. Fagan-Kelly, First Lieutenant, USAF

AFIT-ENP-13-M-09

DEPARTMENT OF THE AIR FORCE
AIR UNIVERSITY

AIR FORCE INSTITUTE OF TECHNOLOGY

Wright-Patterson Air Force Base, Ohio

DISTRIBUTION STATEMENT A.
APPROVED FOR PUBLIC RELEASE; DISTRIBUTION UNLIMITED.

The views expressed in this thesis are those of the author and do not reflect the official policy or position of the United States Air Force, Department of Defense, or the United States Government. This material is declared a work of the United States Government and is not subject to copyright protection in the United States.

AFIT-ENP-13-M-09

THREE DIMENSIONAL POSITRON ANNIHILATION MOMENTUM
SPECTROSCOPY OF LITHIUM TETRABORATE CRYSTALS

THESIS

Presented to the Faculty

Department of Engineering Physics

Graduate School of Engineering and Management

Air Force Institute of Technology

Air University

Air Education and Training Command

In Partial Fulfillment of the Requirements for the
Degree of Master of Science in Nuclear Engineering

Stefan B. Fagan-Kelly, BS

First Lieutenant, USAF

March 2013

DISTRIBUTION STATEMENT A.
APPROVED FOR PUBLIC RELEASE; DISTRIBUTION UNLIMITED.


THREE DIMENSIONAL POSITRON ANNIHILATION MOMENTUM
SPECTROSCOPY OF LITHIUM TETRABORATE CRYSTALS

Stefan B. Fagan-Kelly, BS
First Lieutenant, USAF

Approved:


Larry W. Burggraf, PhD (Chairman)

26 Feb 2013
Date


John W. McClory, PhD (Member)

15 MAR 2013
Date


Maj Benjamin R. Kowash (Member)

15 Mar 2013
Date

Abstract

Previous endeavors in positron annihilation spectroscopy (PAS) at AFIT have resulted in the design and characterization of a second-generation three-dimensional positron annihilation momentum spectroscopy system (3DPAMSS) which combines two-dimensional angular correlation of annihilation radiation (2D ACAR) and coincident Doppler broadening of annihilation radiation (CDBAR) in order to measure electron momentum distributions in samples and thus characterize material defects. The focus of this particular research is to nondestructively measure negative defects in the crystal lattice of copper-doped, silver-doped, and undoped lithium tetraborate by 3DPAMSS spectroscopy using a Na-22 source and two high-purity germanium (HPGe) position-resolvable strip detectors. Lithium tetraborate is a candidate material for novel neutron detectors and characterizing its crystal structure is necessary to fully understand its properties. Several angular deviation and differential energy features are noted, which are translated to potential electron momentum distribution features and crystal defect characteristics.

I dedicate this thesis to my mother, Katherine Ann Fagan, who passed away at the beginning of my Master's program at AFIT.

Acknowledgments

I would like to give great thanks to my thesis advisor, Dr. Larry Burggraf for his intelligent input and constructive guidance; my thesis committee for providing useful feedback and ideas along the way; Mr. Eric Taylor for his expert vacuum system knowledge and willingness to assist; Mr. Dan Ryan at the AFIT machine shop for his accurate and effective work creating my source holder in a short-notice situation; Dr. James Petrosky and Mr. Brian Harcek for their work acquiring the radioactive sources for this experiment; Capt. Stephen Jimenez for his consistent and useful advice with performing the experiment and help with solving coding issues, and Maj. Angelo Bonavita for his help creating and debugging data processing code used in this work.

Stefan B. Fagan-Kelly

Table of Contents

	Page
Abstract.....	iv
Acknowledgments.....	vi
Table of Contents.....	vii
List of Figures.....	x
List of Tables.....	xvii
List of Equations.....	xviii
List of Abbreviations.....	xix
I. Introduction.....	1
1.1 Background and Motivation.....	1
1.2 Positron Physics and Chemistry.....	2
1.3 Sources of Positrons.....	4
1.4 Positron Annihilation Spectroscopy.....	6
1.4.1 Lifetime Spectroscopy.....	8
1.4.2 Angular Correlation of Annihilation Radiation.....	8
1.4.3 Doppler Broadening of Annihilation Radiation.....	10
1.5 Solid State Materials.....	12
1.5.1 Crystal Lattice Structure and Defects.....	12
1.5.2 X-ray Irradiation Effects on Crystal Lattice Structure.....	13
1.6 Lithium Tetraborate (LTB).....	14
1.6.1 Copper-doped Lithium Tetraborate.....	16
1.6.2 Silver-doped Lithium Tetraborate.....	17
II. Literature Review.....	19
2.1 Previous research at AFIT.....	19
2.1.1 2D Momentum Distributions and Feshbach Resonances.....	19
2.1.2 3D Positron Annihilation Momentum Measurements (3DPAMMs) of 6H SiC.....	19
2.1.3 3D Positron Annihilation Spectroscopy System (3DPASS).....	21
2.1.4 EPR and ENDOR Studies of Point Defects in Lithium Tetraborate.....	22
2.2 Positron work done at other institutions.....	22
III. Experimental Equipment.....	24

3.1	Double-Sided Strip Detectors (DSSDs).....	24
3.1.1	<i>DSSD Efficiency Calculations</i>	25
3.1.2	<i>DSSD Resolution Calculations</i>	29
3.2	Electronics.....	31
3.3	Vacuum System.....	33
3.3.1	<i>Vacuum Chamber</i>	33
3.3.2	<i>Vacuum Pump</i>	35
3.3.3	<i>Vacuum Gauge</i>	36
3.3.4	<i>Manipulator Rod</i>	37
3.4	Radioactive Sources.....	38
3.4.1	⁸⁵ Sr.....	38
3.4.2	²² Na.....	38
3.5	Shielding.....	40
IV.	Experimental Procedure.....	42
4.1	Source-Sample Configuration.....	42
4.2	Mounting a Sample.....	46
4.2	Energy Calibration.....	49
4.3	Efficiency Calibration.....	50
4.4	System Alignment with Copper Sample.....	54
4.5	Vacuum Pumpdown.....	58
4.6	Data Collection.....	59
4.6.1	<i>Digital Data Acquisition</i>	59
4.6.2	<i>Data File Parsing</i>	60
4.6.3	<i>Subpixel Interpolation</i>	62
4.6.4	<i>Subpixel Efficiency / Resolution Calculation</i>	64
V.	Data Analysis and Results.....	66
5.1	2D ACAR and CDBAR Calculation.....	66
5.2	Results for Virgin Lithium Tetraborate.....	67
5.3	Results for Copper-Doped Lithium Tetraborate.....	80
5.4	Results for Irradiated Silver-Doped Lithium Tetraborate.....	88
5.5	Electron Momentum Distributions for LTB.....	95
5.6	Translations to Negative Defect Analysis.....	96
VI.	Conclusions and Further Work.....	97
6.1	Conclusions for LTB 3D PAMS.....	97
6.2	Comparison to Previous Work.....	100
6.3	Impact of Results.....	101
6.4	Further Work.....	101
6.4.1	<i>Positron Beam</i>	101
6.4.1	<i>ThO₂ and U:ThO₂</i>	102
6.4.2	<i>Data Analysis</i>	103

Appendix A:	Source-Sample Mount Design	104
Appendix B:	Data Parsing Code.....	105
Appendix C:	Data Analysis Code.....	110
Appendix D:	Equipment and Source Data.....	125
Appendix E:	Additional Information on Positron Beam	126
Bibliography	128
Vita.....	130

List of Figures

	Page
Figure 1: Behavior of the positron as it enters a crystal lattice. Positrons tend to become trapped at vacancy defects. Reproduced with permission from [5].....	3
Figure 2: List of typical reactions in nature in which positive beta particles are emitted. Reproduced with permission from [7].....	5
Figure 3: Radioactive decay of ^{22}Na . Reproduced with permission from [8].	6
Figure 4: Survey of various crystal lattice defects. Positrons tend towards the negative defects listed in green. Reproduced with permission from [11].	13
Figure 5: Basic structural component of the $\text{Li}_2\text{B}_4\text{O}_7$ crystal lattice (left) and a unit cell of $\text{Li}_2\text{B}_4\text{O}_7$ (right) [14].	15
Figure 6: Four $(\text{B}_4\text{O}_9)^{6-}$ units comprising the LTB crystal lattice. Left image is when viewed along the c axis and right image is when viewed along the b axis [14].	15
Figure 7: Lithium tetraborate sample demonstrating its physical characteristics.	15
Figure 8: 2-D ACAR Spectrum for O-ion irradiated 6H SiC from Williams [2], [3]. This shows the correlation of annihilation radiation momentum in two dimensions.	20
Figure 9: Coincidence DBAR (CDBAR) Results for O-ion irradiated 6H SiC from Williams [2], [3]. This shows the 3D momentum lineshape and Doppler broadened momentum lineshape.	21
Figure 10: Picture of one of the Double-Sided Strip Detectors (DSSDs), made by PhDs Co., showing mechanical cooling system, translatable stage, and channel connections.	24

Figure 11: Original Efficiency Matrix of the DSSD as calculated by Williams [3]. Blue indicates low efficiency and red high efficiency. 26

Figure 12: Subpixel mapping of counts detected using a 5x5 subpixel matrix in each pixel for each detector. Deep purple represents zero counts, and the contour value increases by 100 counts for each time the color gets brighter. The maximum contour in the center of some of the pixels is a 300 count contour line. 28

Figure 13: Subpixel efficiency contour plot for each detector, reported as percent values. Horizontal and vertical axes are labeled by pixel number. 28

Figure 14: Resolution contour plot for each detector, reported as FWHM in keV. Horizontal and vertical axes are labeled by pixel number. 30

Figure 15: Spect72 digital data acquisition system. 32

Figure 16: Vacuum Chamber with axes overlaid [18]. 35

Figure 17: Picture of the Pfeiffer HiCube HiPace 80 Eco turbopump and its connection to the vacuum chamber using a mechanical gate valve. 36

Figure 18: 1.0 mCi ^{22}Na B009 capsule source used in this experiment. The radioactive portion is a small disk located at the end of the copper capsule, under a thin titanium film, in the foreground. 39

Figure 19: Overhead layout of the three-dimensional positron annihilation momentum spectroscopy (3DPAMS) experiment. 42

Figure 20: Source-Sample Configuration, adapted from [18]. 43

Figure 21: Newly designed source-sample mount fabricated by the AFIT machine shop. 44

Figure 22: Aligning the sample at a precise 45 degree angle with respect to the base of the mount. 48

Figure 23: Energy calibration for each strip of Detector 1 at 511 keV..... 50

Figure 24: Individual detector response from efficiency calibration run. These datasets were used to generate the efficiency correction matrices which were later applied during the ACAR and DBAR calculations..... 52

Figure 25: Average relative subpixel values calculated for each detector using efficiency calibration data..... 53

Figure 26: Subpixel average relative efficiency for the PhDs DSSD determined by Williams [3]. 54

Figure 27: Performing a visual alignment of the sample in relation with the chamber openings and detectors..... 55

Figure 28: Coincident response across both detector faces for the pure LTB dataset. 68

Figure 29: ACAR calculation for the pure LTB dataset showing deviation from colinearity in the plane transverse to gamma emission. Left picture shows combined 2D plot while right picture shows each dimension individually. 69

Figure 30: ACAR calculation for the pure LTB dataset; left picture shows data with the pixel-normalized efficiency correction and right picture shows the same pixel-normalized efficiency-corrected data, only pixel-filtered. 70

Figure 31: ACAR calculation for the pure LTB dataset; left picture shows data with the detector-normalized (average) efficiency correction and right picture shows with the Williams efficiency correction. 71

Figure 32: Raw ACAR spectrum for the pure LTB dataset plotted as a histogram contour plot using a 1.5 mrad binning resolution in electron momentum units of $10^{-3} m_0c$. Red indicates higher counts and yellow lower counts, with blue being zero. 72

Figure 33: Raw results for counts versus distance from the DSSD crystal center from both detectors for pure LTB. Left image shows horizontal axis and right image shows vertical axis. 73

Figure 34: Results for counts versus distance from the DSSD crystal center from both detectors for pure LTB with the pixel-normalized efficiency correction applied. Left image shows horizontal axis and right image shows vertical axis. 73

Figure 35: Results for counts versus distance from the DSSD crystal center from both detectors for pure LTB with the detector-normalized efficiency correction applied. Left image shows horizontal axis and right image shows vertical axis. 74

Figure 36: Results for counts versus distance from the DSSD crystal center from both detectors for pure LTB with the Williams efficiency correction applied. Left image shows horizontal axis and right image shows vertical axis. 75

Figure 37: DBAR calculation for the pure LTB sample. Left image shows the energies of events in the two detectors graphed against each other; right image shows the energy data from each detector individually. 76

Figure 38: DBAR calculation for the pure LTB sample corrected for efficiency. Left image shows DBAR data with an efficiency correction applied; right image shows the data with an efficiency correction and a pixel filter applied. 76

Figure 39: Coincidence DBAR (CDBAR) results for undoped LTB with swath width $\Delta = \pm 2$ keV on left & ± 4 keV on right for 0.4, 0.5, & 0.6 keV energy binning resolutions. Black is raw data; blue is adjusted for the pixel-normalized efficiency correction... 78

Figure 40: Coincidence DBAR (CDBAR) results for undoped LTB with swath width $\Delta = \pm 2$ keV on left & ± 4 keV on right for 0.4 keV energy binning resolutions; black is raw data and blue is adjusted using the detector-normalized efficiency correction. . 79

Figure 41: CDBAR results for undoped LTB with swath width $\Delta = \pm 2$ keV on left & ± 4 keV on right for 0.4 keV energy binning resolutions; black is raw data and blue is adjusted using the Williams efficiency correction..... 80

Figure 42: ACAR results for the Cu:LTB sample. Left picture shows actual data with misalignment of sample in the chamber. Right picture shows the same data after software alignment correction. 81

Figure 43: ACAR data for Cu:LTB: left image shows raw ACAR data presented by axis and right image shows 2D pixel-normalized efficiency-corrected ACAR data. 82

Figure 44: ACAR results for the Cu:LTB sample; left picture shows data with the detector-normalized efficiency correction and right picture shows with the Williams efficiency correction. 83

Figure 45: Raw ACAR spectrum for Cu:LTB, presented using a histogram contour routine with a 1.5 mrad binning resolution, in electron momentum units of $10^{-3} m_0c$. Red indicates higher counts and yellow lower counts, with blue being zero. 84

Figure 46: DBAR results for Cu:LTB. Left image shows raw DBAR data from both detectors plotted against each other, while right image shows the data from each detector individually. 84

Figure 47: CDBAR results for Cu:LTB with swath half-width of $\Delta = \pm 2$ keV on left and ± 4 keV on right for 0.5, 0.6, and 0.85 keV binning resolutions. Black is raw data; blue is efficiency-corrected using the pixel-normalized efficiency correction..... 86

Figure 48: CDBAR results for Cu:LTB with swath half-width of $\Delta = \pm 2$ keV on left and ± 4 keV on right for 0.6 keV binning resolution. Black is raw data; blue is adjusted using the detector-normalized efficiency correction. 87

Figure 49: CDBAR results for Cu:LTB with swath half-width of $\Delta = \pm 2$ keV on left and ± 4 keV on right for 0.6 keV binning resolution. Black is raw data; blue is adjusted using the Williams efficiency correction. 87

Figure 50: ACAR data for irradiated Ag:LTB. Left image shows raw data while right image shows the data with a subpixel relative efficiency correction. 89

Figure 51: ACAR results for irradiated Ag:LTB; left picture shows data with the detector-normalized efficiency correction and right picture shows with the Williams efficiency correction. 90

Figure 52: Raw ACAR spectrum for Ag:LTB, presented using a histogram contour plotting routine with a 1.5 mrad binning resolution, in electron momentum units of $10^{-3} m_0c$. Red indicates higher counts and yellow lower counts, with blue being zero. 91

Figure 53: DBAR data for irradiated Ag:LTB. Left image shows raw DBAR results for both detectors together and right image shows energy plots for each detector individually. 91

Figure 54: CDBAR results for irradiated Ag:LTB with $\Delta = \pm 2$ keV on left and ± 4 keV on right for 0.3, 0.4, and 0.5 keV energy binning resolutions. Black is raw data and blue is adjusted using the pixel-normalized efficiency correction. 93

Figure 55: CDBAR results for irradiated Ag:LTB with $\Delta = \pm 2$ keV on left and ± 4 keV on right for 0.4 keV energy binning resolution. Black is raw data and blue is corrected using the detector-normalized efficiency correction. 94

Figure 56: CDBAR results for irradiated Ag:LTB with $\Delta = \pm 2$ keV on left and ± 4 keV on right for 0.4 keV energy binning resolution. Black is raw data and blue is adjusted using the Williams efficiency correction. 94

List of Tables

	Page
Table 1: Channel number and subpixel designations	63

List of Equations

	Page
Equation 1: Relationship between angular deviation and electron momentum.....	9
Equation 2: Relationship between energy difference and electron momentum	11
Equation 3: Calculation of subpixel position number from figures of merit	62
Equation 4: Calculation of solid angle for intrinsic efficiency	64
Equation 5: Solid angle for pixels off centerline	64

List of Abbreviations

ACAR	Angular Correlation of Annihilation Radiation
DBAR	Doppler Broadening of Annihilation Radiation
XRF	X-Ray Fluorescence
EPR	Electron Paramagnetic Resonance
AFIT	Air Force Institute of Technology
Ps	Positronium
PAS	Positron Annihilation Spectroscopy
PALS	Positron Annihilation Lifetime Spectroscopy
LTB	Lithium Tetraborate
COM	Center of Mass
PMT	Photo-Multiplier Tube
3DPAMM	3D Positron Annihilation Momentum Measurement
3DPASS	3D Positron Annihilation Spectroscopy System
HPGe	High-Purity Germanium
DSSD	Double-Sided Strip Detector
FWHM	Full-Width at Half Maximum
APBS	Advanced Positron Beam System
HV, UHV	High Vacuum, Ultra High Vacuum
FPGA	Field-Programmable Gate Array
FOM	Figure of Merit

THREE DIMENSIONAL POSITRON ANNIHILATION MOMENTUM SPECTROSCOPY OF LITHIUM TETRABORATE CRYSTALS

I. Introduction

1.1 Background and Motivation

The underlying goal of this research is to structurally analyze candidate nuclear detection materials using simultaneous two-dimensional angular correlation of annihilation radiation (2-D ACAR) and coincident Doppler broadening of annihilation radiation (CDBAR). This work will enable materials negative defect analysis and will complement other characterization methods such as X-ray fluorescence (XRF), cathodoluminescence, thermoluminescence, and surface Raman spectroscopy.

Analyzing and characterizing the atomic structural defects of materials is of vital importance to the Air Force and to all materials engineering processes. For materials which undergo nuclear reactions, the ability to analyze effects of nuclear reactions in particular nuclear materials preparations efficiently and thoroughly opens new doors for nuclear safety and surety, material effectiveness, and component reliability. Lithium tetraborate is a novel candidate material for neutron detection. Its crystal defects in available preparations must be properly characterized in order to fully understand its properties and confirm its usefulness as a luminescent neutron detection material [1].

Positron annihilation spectroscopy is an innovative and unique method to investigate the atomic and electronic structure of materials. With significant modification it could also be applied to look at millisecond timescale radiation effects. Using both 2-D ACAR and CDBAR simultaneously is a relatively new way of taking advantage of the

properties of the positron in order to provide more insight into material microstructure. A practical implementation of this technique was developed at AFIT by Williams and Burggraf [2],[3].

After the introduction, first previous work is discussed. Then positron theory and solid-state crystal lattice structure is given some attention. Afterwards, equipment used in the experiment and the procedure used to mount samples, pump down the chamber, and collect data are explored. Then, data analysis techniques are covered. Finally, works cited in this paper are listed and diagrams and code discussed throughout the paper are listed.

1.2 Positron Physics and Chemistry

The positron (e^+) is the antiparticle of the electron (e^-) and the two annihilate when they come together. The positron is an exotic particle, not commonly found in nature because of its short lifetime, which is created during positive beta decay. The positron is antimatter, the antithesis of the electron (the antielectron) which, in pair production, is formed with an electron from a gamma having energy greater than their summed rest masses. The positron is equal in mass to the electron (511 keV), but opposite in charge (positive rather than negative). When annihilation occurs, an electron and positron vanish usually forming two oppositely directed 511 keV photons. A single detector will show the presence of a 511 keV gamma photon, half of the mass energy of the electron-positron pair prior to annihilation.

In positron annihilation, two particles having mass are converted into gamma photons, which have energy and momentum, but no mass. Normally, two gamma particles are ejected in opposite directions (180 degrees from each other in the center of

mass reference frame) in order to conserve angular momentum, although there is a very small probability that three gammas are emitted (annihilation into three gammas is less than 1% of the two-gamma rate [4]).

The bound state of a positron and electron is called a positronium (Ps) atom, which has two ground states: orthopositronium, in which the particle spins are parallel, having an average lifetime of 140 ns; and parapositronium, in which the particle spins are antiparallel, having an average lifetime of 120 ps. As a positron travels in matter, it undergoes scattering events which cause it to lose energy until it finally thermalizes, diffuses, localizes around an atom or lattice site, and eventually it annihilates with an electron near that location. Because of the positive charge of a positron, when it enters a crystal lattice site it tends to localize in areas with lower positive charge density such as a vacancy or void – areas where nuclei are not present. For this reason, positrons are used for investigating negative defects in materials. Figure 1 depicts how the positron behaves as it enters a crystal lattice.

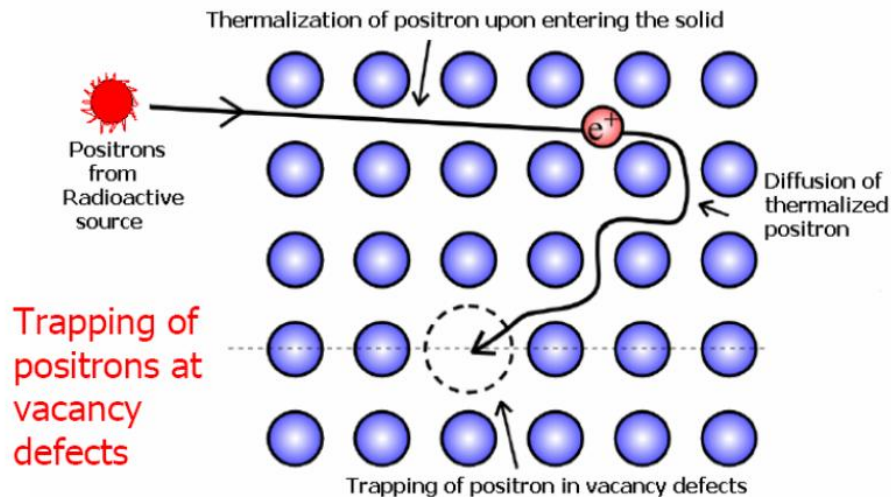


Figure 1: Behavior of the positron as it enters a crystal lattice. Positrons tend to become trapped at vacancy defects. Reproduced with permission from [5].

Upon encountering the surface of a solid, the positron may backscatter. If not, implantation occurs, after which the positron quickly thermalizes by conduction electron scattering, including plasmon and electron-hole pair excitations, and finally by phonon scattering. The time scale for thermalization is roughly 10 ps [6]. Since the probability of annihilation is small unless the velocity of the positron relative to that of the electrons is low, the positron may penetrate somewhat deeply: typical implantation depths range from a few Angstroms to a few microns. The positrons then diffuse through the crystal lattice; typical diffusion lengths in relatively defect-free materials are on the order of 1000 Angstroms [6]. During diffusion the positrons may undergo free annihilation (~100 ps), or encounter an open-volume defect in which trapping and subsequent annihilation (~200-400 ps) may occur. When defects are present, the positron lifetime tends to increase and the diffusion length tends to decrease as compared to a defect-free sample [6].

1.3 Sources of Positrons

The majority of beta decays which occur in nature are negative, meaning they generate a β^- particle, an energetic electron. Reactions which involve positive beta decay are less common, but they do occur, typically in isotopes resulting from proton irradiation. Figure 2 below lists the more common reactions which generate a β^+ particle, an energetic positron. In addition to a positron, positive beta decay generates a neutrino as well (negative beta decay generates an antineutrino).

1.	$p + {}^{11}\text{B} \Rightarrow {}^{11}\text{C} + n$ ($E_T = 2.76$ MeV) ${}^{11}\text{C} \Rightarrow {}^{11}\text{B} + e^+$ ($\tau_{1/2} = 20$ min.)
2.	$p + {}^{13}\text{C} \Rightarrow {}^{13}\text{N} + n$ ($E_T = 3$ MeV) ${}^{13}\text{N} \Rightarrow {}^{13}\text{C} + e^+$ ($\tau_{1/2} = 10$ min.)
3.	$p + {}^{15}\text{N} \Rightarrow {}^{15}\text{O} + n$ ($E_T = 3.53$ MeV) ${}^{15}\text{O} \Rightarrow {}^{15}\text{N} + e^+$ ($\tau_{1/2} = 2.03$ min.)
4.	$p + {}^{17}\text{O} \Rightarrow {}^{17}\text{F} + n$ ($E_T = 3.55$ MeV) ${}^{17}\text{F} \Rightarrow {}^{17}\text{O} + e^+$ ($\tau_{1/2} = 66$ sec.)
5.	$p + {}^{18}\text{O} \Rightarrow {}^{18}\text{F} + n$ ($E_T = 2.45$ MeV) ${}^{18}\text{F} \Rightarrow {}^{18}\text{O} + e^+$ ($\tau_{1/2} = 1.87$ hr.)
6.	$p + {}^{19}\text{F} \Rightarrow {}^{19}\text{Ne} + n$ ($E_T = 4.03$ MeV) ${}^{19}\text{Ne} \Rightarrow {}^{19}\text{F} + e^+$ ($\tau_{1/2} = 18$ sec.)
7.	$p + {}^{26}\text{Mg} \Rightarrow {}^{26}\text{Al} + n$ ($E_T = 5.01$ MeV) ${}^{26}\text{Al} \Rightarrow {}^{26}\text{Mg} + e^+$ ($\tau_{1/2} = 6.5$ sec.)
8.	$p + {}^{22}\text{N} \Rightarrow {}^{22}\text{Na} + n$ ${}^{22}\text{Na} \Rightarrow {}^{22}\text{Ne} + e^+$ ($\tau_{1/2} = 2.6$ years.)

Figure 2: List of typical reactions in nature in which positive beta particles are emitted. Reproduced with permission from [7].

Reaction number eight in Figure 2 above shows that ${}^{22}\text{Na}$ (sodium-22) naturally beta decays with a characteristic positron, with a half-life of 2.6 years. This radioactive isotope is a very common source for positrons in a laboratory environment. Figure 3 below outlines the specific decay mechanism of the ${}^{22}\text{Na}$ isotope.

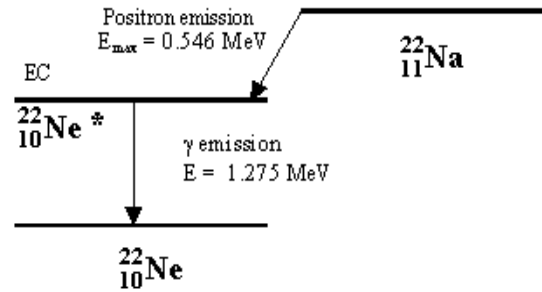


Figure 3: Radioactive decay of ^{22}Na . Reproduced with permission from [8].

^{22}Na undergoes positive beta decay, ejecting a positron which has a rest mass-energy of 511 keV, and a neutrino. The maximum overall energy of reaction is 546 keV. Very quickly after this positive beta emission (3.7 picoseconds) gamma of energy 1.275 MeV is emitted 99.9% of the time (0.1 % of the time ^{22}Na decays directly to ^{22}Ne without converting to an excited state, and the 1.275 MeV gamma is not emitted). Because of the closeness in time in which these two particles are emitted, the 1.275 MeV gamma is referred to as the ‘birth’ gamma, detection of which signifies the birth of the positron. A typical gamma detector spectrum of ^{22}Na will show a large characteristic peak at 511 keV, which represents the annihilation gammas being produced. Positrons do not travel very far in air (most are absorbed in less than a meter) before annihilating with an electron and producing annihilation gamma photons. A second peak will also be present at 1.275 MeV, representing the birth gamma. At energies lower than 511 keV the spectrum will show a Compton continuum along with a characteristic Compton edge.

1.4 Positron Annihilation Spectroscopy

Positron annihilation spectroscopy (PAS) is an investigative microscopic analytical technique which provides information about a material’s crystal lattice

structure. PAS employs the detection of gamma radiation emitted following annihilation of slow (thermalized) positrons in sample materials. The spatial and energy distributions of this gamma radiation provide information about the sample material's structure and bulk properties [9]. Negative crystal lattice defects can be effectively studied in a sample solid material using PAS.

The most basic of PAS techniques, lifetime spectroscopy, is a PAS technique which utilizes the variation in positron lifetime within a material to provide information about the material's electron density throughout its bulk. PAS techniques used to measure the electron-positron ($e^- - e^+$) pair's momentum prior to annihilation have been well-documented in literature, with the most common being ACAR and DBAR. In momentum PAS, the angular deviation and energy differential spectral patterns produced from annihilation radiation provide information about electron momentum distributions and the chemical environment of a material's crystal lattice, which in turn provides information about the material's microscopic structure. Momentum PAS techniques yield more information about the chemical environment (e.g., chemical bonds, lattice structure and defects, electron shell structure and interaction, and potentially oxidation state) of a substance than do lifetime techniques, which simply yield information on electron density. In general with PAS, positrons tend to annihilate more readily with electrons in the outer shells of the atoms of a lattice (e.g. valence electrons) and have a lower probability to penetrate down into the inner shells of lattice atoms (e.g. core electrons). Valence electrons will have less overall momentum than core electrons: core electrons will cause larger deviations in ACAR and DBAR spectra than valence electrons.

1.4.1 Lifetime Spectroscopy

Positron annihilation lifetime spectroscopy (PALS) is a method in which one analyzes the lifetime of positrons interacting inside materials. The positron lifetime τ at a particular annihilation site is determined by the local electron density. The positron lifetime will be longer in regions of a material where electron density is lower and shorter where electron density is higher. The positron has a higher probability to encounter an electron in areas of higher electron density, and will have a higher tendency to annihilate more quickly in such areas. The inverse of lifetime, the annihilation rate λ , is directly proportional to site electron density. The birth of the positron in ^{22}Na is accompanied by simultaneous emission of a 1.275 MeV gamma particle, which serves as the birth signal for lifetime measurements. The death signal is the 511 keV gamma which comes from positron annihilation. The difference between these two timing measurements yields the lifetime of the positron. Although some recent advancements have been made in the areas of position-sensitive lifetime spectroscopy, lifetime spectroscopy is not applied in this work, only momentum techniques are employed.

1.4.2 Angular Correlation of Annihilation Radiation

A momentum PAS technique, angular correlation of annihilation radiation (ACAR) measures the angular deviation between annihilation gamma photons. The purpose of ACAR is to understand thermalization and momentum transfer of positrons and positronium (Ps) in matter. The main application of ACAR is the study of the electron structure of the bulk solid. In the center-of-mass (COM) frame of reference of the positron and electron pair, the gammas created from annihilation leave the site of annihilation with identical energy and in opposite direction. However, in the lab frame,

this is not the case: the expected 180-degree emission angle between the two gammas is slightly deviated. Because of the relativistic transformation from the COM frame into the lab frame, $\theta_1 \neq \theta_2$ (where θ_1 and θ_2 are the angles of each emitted gamma with respect to a common reference axis). Measurement of the deviation from colinearity yields information about the momentum of the annihilating electron-positron pair prior to annihilation (particularly its momentum in the direction transverse to γ emission). From this angular deviation measurement, knowledge of the structural properties of the sample material in which the annihilation occurred can be inferred. The total momentum of the electron-positron pair can be assumed to be simply that of the electron, since the momentum of the positron is very low in comparison to that of the electron (after the positron thermalizes to 0.2-0.3 eV; a valence electron would have a binding energy on the order of 10s of eV and this would increase to 100s of eV closer to the core). The momentum of the positron can be largely ignored. Equation 1 shows how the angular deviation relates to electron momentum in the direction perpendicular to gamma emission:

$$\Delta\theta = \frac{p_{\perp}}{mc} \quad (1)$$

Where:

- $\Delta\theta$ = Angular deviation between annihilation gammas
- p_{\perp} = Electron momentum perpendicular to gamma emission
- m = Mass of an electron (9.11×10^{-31} kg)
- c = Speed of light (3×10^8 m/s)

One-dimensional (1D) ACAR makes use of two detectors and attenuating blocks with slits ('long slit geometry' [9]) in them to allow annihilation gammas to interact only in one dimension. One detector setup is held stationary while the second setup is rotated around the axis centered at the sample. This provides angular correlation in one dimension.

Two-dimensional (2D) ACAR requires the use of two position-sensitive detectors such as an array of discrete scintillator-photomultiplier tube (PMT) detectors, multiwire proportional counters, position-sensitive phototubes, or Anger cameras [9]. The interaction of a gamma with the scintillator causes light to be produced which is subsequently detected and amplified by the PMT. The spatial location of events is determined by the electronics and software of the system [9]. 2D ACAR results in a two-dimensional measurement of the electron momentum distribution in the plane perpendicular to propagation of the annihilation gammas. The results from each detector are combined in order to correlate them.

1.4.3 Doppler Broadening of Annihilation Radiation

Doppler broadening of annihilation radiation (DBAR) is a momentum PAS technique which measures the difference in energy between annihilation gamma photons. DBAR involves accounting for energy resolution of full-energy events in positron annihilation spectra. The broadening of the full-energy peak yields information on the momentum of the electron-positron pair just prior to annihilation (again, assumed to be simply the momentum of the electron) and subsequently information about the electron momentum distribution within the sample. In the center-of-mass (COM) frame of reference of the electron-positron pair, the gammas created from annihilation leave the

site of annihilation with identical energy. However, in the laboratory frame, this is not the case. Instead of having each gamma at 511 keV, one is detected at an energy slightly higher than 511 keV and the other slightly lower. The shift in energy detected, ΔE_γ , is a result of the initial electron momentum in the laboratory reference frame. Doppler broadening results from the bunching up of the gamma photons (when treated as waves) in one direction and the spreading out of these in the other direction. The peak about 511 keV will be broadened in the spectrum as a result. Equation 2 demonstrates how the difference in energy relates to electron momentum in the direction parallel to gamma emission:

$$\Delta E = \frac{cp_{\parallel}}{2} \quad (2)$$

Where:

$$\begin{aligned} \Delta E &= \text{Shift in energy of 511 keV line} \\ c &= \text{Speed of light } (3 \times 10^8 \text{ m/s}) \\ p_{\parallel} &= \text{Electron momentum parallel to gamma emission} \end{aligned}$$

DBAR can be performed using either one detector or two, since all that is required is information about the width of the full-energy peak. Two-detector DBAR is much more accurate than is one-detector: if a second Ge detector is employed an improvement of two or more orders of magnitude in background reduction is possible [9]. In addition to a reduction in background, the resolution is greatly improved. Application of the coincidence DBAR (CDBAR) technique yields a one-dimensional measurement of the e^-e^+ momentum prior to annihilation in a direction parallel to gamma propagation.

Using two detectors this can be done simultaneously to detect only events occurring in coincidence.

1.5 Solid State Materials

1.5.1 *Crystal Lattice Structure and Defects*

An ideal crystalline solid contains atoms which “are tightly bound to one another in a regular periodic lattice by very strong attractive forces [10].” Neighboring atoms are close enough together that their external electron distributions overlap and interact. The atoms are essentially in contact with one another. The density of such matter is very high compared to that of gaseous matter, as an example. Such condensed matter brings with it its own set of physical considerations. In single crystal materials, the crystal is grown with a repeating lattice pattern from a seed to a maximum extent beyond which the crystal could break, cleave, or become polycrystalline.

Many solids do not conform to the ideal model, however. “Lattice imperfections such as lattice vacancies and extra interstitial atoms may be present, along with other defects in the regular periodic structure of the crystal [10].” These microscopic lattice defects can affect the various macroscopic properties of the overall crystal, such as its mechanical, optical, thermal, electrical, and magnetic properties. Figure 4 demonstrates several of the possible crystal lattice defects that may be present in a solid-state material. Because of their positive charge, positrons tend to migrate towards the negative defects listed in green—voids and vacancies, which are areas absent of electropositive nuclei (and also areas of decreased electron density). Positrons can become trapped in such

negative defects, meaning that they would live longer in these areas and annihilation photons would have a higher tendency to originate from electrons around these areas.

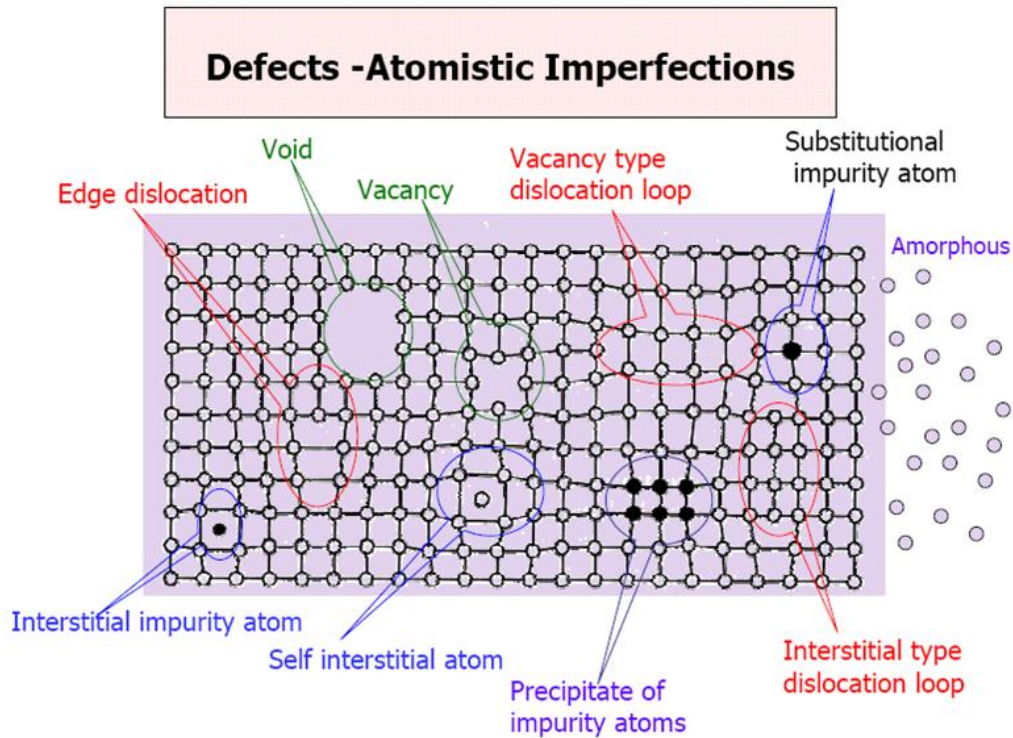


Figure 4: Survey of various crystal lattice defects. Positrons tend towards the negative defects listed in green. Reproduced with permission from [11].

1.5.2 X-ray Irradiation Effects on Crystal Lattice Structure

The crystal lattice structure of a substance may already have defects present. However, introducing various forms of radiation into the substance can create further defects, e.g. by exciting electrons or dislodging atoms.

X-rays are a short-wavelength form of electromagnetic radiation. X-ray radiation is lightly ionizing, highly penetrating, and leaves no activity in the material irradiated [12]. X-ray photons do not directly cause impurities in a crystal lattice. However, they

can “indirectly cause impurity production through chemical bond breakage [13]” which results from excitation of electrons within the atoms of the substance. X-ray photons ionize indirectly, and may cause rare atom displacements via the Compton Effect.

1.6 Lithium Tetraborate (LTB)

Lithium tetraborate ($\text{Li}_2\text{B}_4\text{O}_7$, known as LTB) is a material which appears as a cloudy, glass-like, solid-state, crystalline substance. LTB has a relatively high conductivity and occurs as white hygroscopic monoclinic crystals. LTB is of interest in that it has the potential to be a novel neutron detection material [1]. LTB is a borated salt. Boron occurs naturally with 20% ^{10}B and 80% ^{11}B . Because of the high cross-section of ^{10}B for capturing neutrons, having large natural-abundance boron content produces neutron sensitivity. Characterizing this material will help determine its usefulness as a state-of-the-art neutron detector.

LTB doped with an optically active element (e.g. Ag, Cu) could be used as scintillation material, which is useful for radiation detection. It is also a candidate for high-sensitivity thermoluminescence dosimetry applications. Figure 5 shows a diagram of the basic structural component of the crystal lattice of LTB, and Figure 6 shows how this basic unit is repeated across the entire lattice.

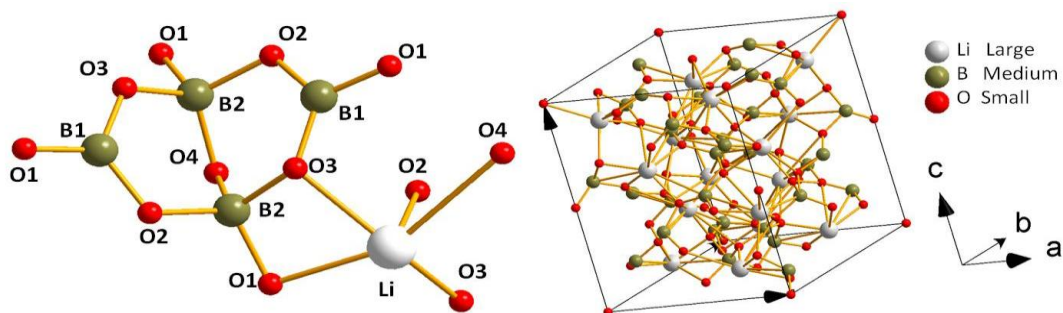


Figure 5: Basic structural component of the $\text{Li}_2\text{B}_4\text{O}_7$ crystal lattice (left) and a unit cell of $\text{Li}_2\text{B}_4\text{O}_7$ (right) [14].

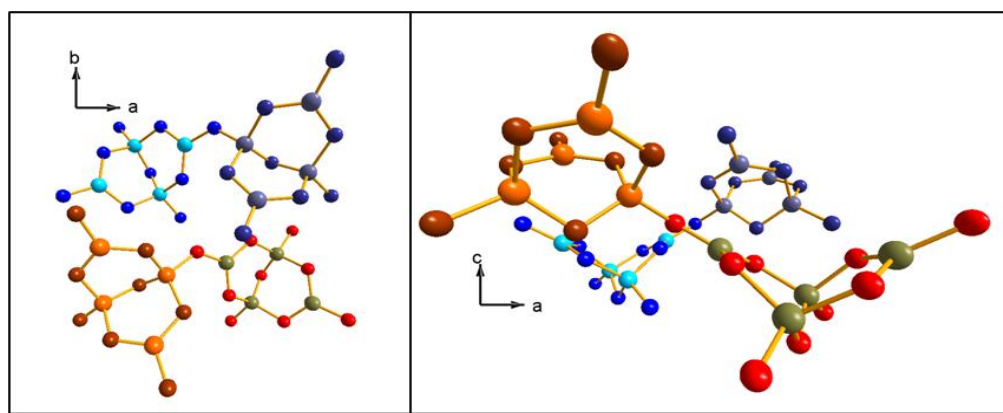


Figure 6: Four $(\text{B}_4\text{O}_9)^{6-}$ units comprising the LTB crystal lattice. Left image is when viewed along the c axis and right image is when viewed along the b axis [14].

Figure 7 below shows an image of a sample of LTB.



Figure 7: Lithium tetraborate sample demonstrating its physical characteristics.

There are large numbers of lithium and compensating oxygen vacancies in the pure LTB crystals [1]. Positrons should localize in the region of the lithium vacancy and on adjacent oxygen atoms in pure LTB. Cu and Ag dopants are near enough to polarize the positron distribution, so that higher angular momenta ACAR features are expected versus the virgin crystal. Cu and Ag dopants will change the layout of the lithium, boron, and oxygen atoms in the crystal lattice of LTB, thus affecting its properties. These dopants can create defects otherwise not present in the virgin material and have the potential to create defects that are easily observed using PAS. The ability to distinguish between various dopants and a virgin sample has great potential.

1.6.1 Copper-doped Lithium Tetraborate

Copper-doped LTB is prepared by doping regular LTB with relatively low levels of Cu in order to create Cu impurities within the crystal structure. The Cu doping can cause LTB to acquire properties desirable of a scintillating material. Cu is significantly higher Z in atomic number than any of the constituents of LTB (Li, B, or O), meaning that ACAR and DBAR spectra measured from this sample should show some higher momentum features versus the undoped sample, although the low doping levels means that the Cu is present in widely dispersed, low concentrations. Higher Z elements contain electrons with higher momentum towards the core of the atom than do lower Z elements.

Known defects in Cu:LTB include the following: Cu^{2+} -Active and $\text{Cu}^{2+}\text{-V}_{\text{Li}}$ that both trap holes ($3d^9$ charge states); electron centers that are $\text{Cu}(0)$ ($3d^{10} 4s^1$) charge states, which are believed to be interstitial copper ions; and Cu^{2+} -Active and the $\text{Cu}(0)$, which are both X-ray radiation induced defects [14]. Corradi et al. characterized the Cu^{2+}

trapped hole center by performing a complete angular dependence study [15]. The hole center was modeled as an $S = 1/2$ hole trapped on a Cu ion substituting for a Li ion and stabilized by a neighboring Li vacancy, thus creating a Cu^{2+} hole center, referred to as the $\text{Cu}^{2+}\text{-V}_{\text{Li}}$ hole center. This seems to be an interesting trap for function of the copper-doped LTB material as a neutron detector. The $\text{Cu}^{2+}\text{-V}_{\text{Li}}$ hole center is always present—X-rays are not required to populate it. Performing electron paramagnetic resonance (EPR) on the material yields a signal of significant magnitude from the $\text{Cu}^{2+}\text{-V}_{\text{Li}}$ hole center without X-ray exposure.

PAS is not likely sufficient to detect Cu^{2+} -Active and $\text{Cu}(0)$ defects. Because the positron is attracted to negative or dipolar sites, the $\text{Cu}^{2+}\text{-V}_{\text{Li}}$ defect is anticipated to be detected by PAS in Cu:LTB. Therefore, PAS may provide complementary information to EPR in order to analyze defects relevant to effectiveness of preparations of Cu:LTB for neutron detection.

1.6.2 Silver-doped Lithium Tetraborate

As with Cu:LTB, doping the LTB crystal during its growth with relatively low levels of Ag introduces impurities in the crystal lattice. These substitutions and vacancies cause the properties of the LTB to be altered. Silver-doped LTB has been characterized using other investigative methods (EPR and ENDOR [14], etc.) and also promises to be a good candidate for behaving as a scintillating detector. Again, the Ag is significantly higher Z than Li, B, and O, meaning it should produce higher electron momentum features in ACAR and DBAR, although the low doping levels once again mean the Ag is widely dispersed in low concentrations.

The Ag:LTB crystal used in this experiment was grown by the Czochralski technique at the Institute of Physical Optics (L'viv, Ukraine), where silver was an as-grown ingredient, meaning that it was not diffused after crystal growth [16]. The crystal contains both interstitial Ag^+ ions and Ag^+ ions substituting for Li^+ ions. A particular defect of interest is the silver electron center that appears in EPR spectra centered at 338 mT. One interesting quality is that there are no Ag^{2+} centers prior to x-ray irradiation [14], so therefore irradiated Ag:LTB may be more interesting to investigate first as opposed to annealed. The silver ion can act as both an electron and hole trap. The silver electron center is paired with the silver hole center. Positrons entering the lattice will most likely be attracted to the Ag when it is acting as a hole trap.

II. Literature Review

2.1 Previous research at AFIT

2.1.1 2D Momentum Distributions and Feshbach Resonances

Two-dimensional momenta measurements were successfully demonstrated along with initial investigation into detection of Feshbach resonances [17] by Maj. Paul Adamson. Feshbach resonances are bound states which occur when the coupling between an internal degree of freedom and reaction coordinates goes away. This coupling can lead to dissociation of the chemical bond. The opposite of a Feshbach resonance is a shape resonance. Future endeavors in this work will build upon these findings. The incorporation of a low-energy positron beam system made by First Point Scientific, Inc. and setup and characterized by Capt. Stephen Jimenez [18] will help while investigating these phenomena by greatly reducing experiment times.

2.1.2 3D Positron Annihilation Momentum Measurements (3DPAMMs) of 6H SiC

Lt. Col. Christopher Williams used PAS to measure 3-D momenta of the ground electronic states in crystalline 6H SiC before and after irradiation with 24 MeV O^{3+} ions to implant oxygen atoms in the lattice. 2-D ACAR and coincidence DBAR spectra were measured and analyzed. A novel technique was illustrated for analyzing 3D momentum datasets in which the parallel momentum component, p^{\parallel} (obtained from the coincidence DBAR measurement) was selected for annihilation events that possess a particular perpendicular momentum component, p^{\perp} , observed in the 2D ACAR spectrum. Figure 8 shows the 2-D ACAR Spectrum for O-ion irradiated 6H SiC from Williams [2], [3]. This shows the correlation of annihilation radiation momentum in two dimensions. The four

noticeable features represent Si-C bonds in the crystal lattice. The O-ion implantation affected the direction of the momentum significantly.

Figure 9 shows CDBAR results for O-ion irradiated 6H SiC from Williams [2], [3]. This shows the Doppler broadened momentum lineshape and the 3D momentum lineshape, which is the lineshape which results from constraining the momentum using the 2D ACAR spectral features.

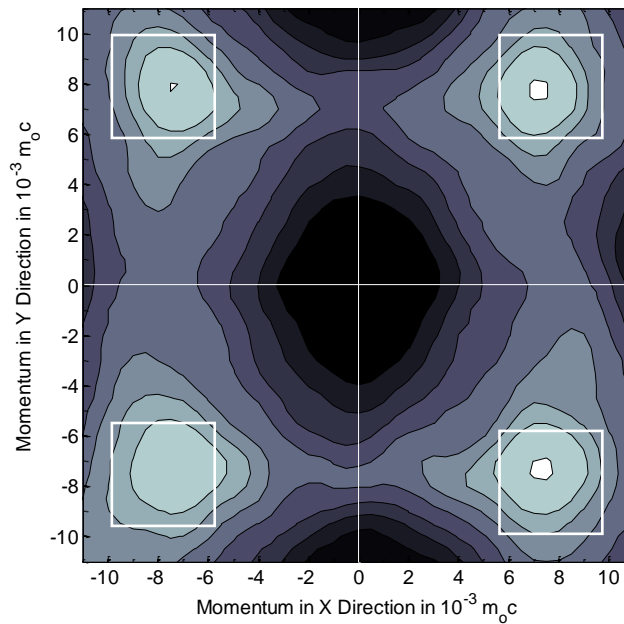


Figure 8: 2-D ACAR Spectrum for O-ion irradiated 6H SiC from Williams [2], [3]. This shows the correlation of annihilation radiation momentum in two dimensions.

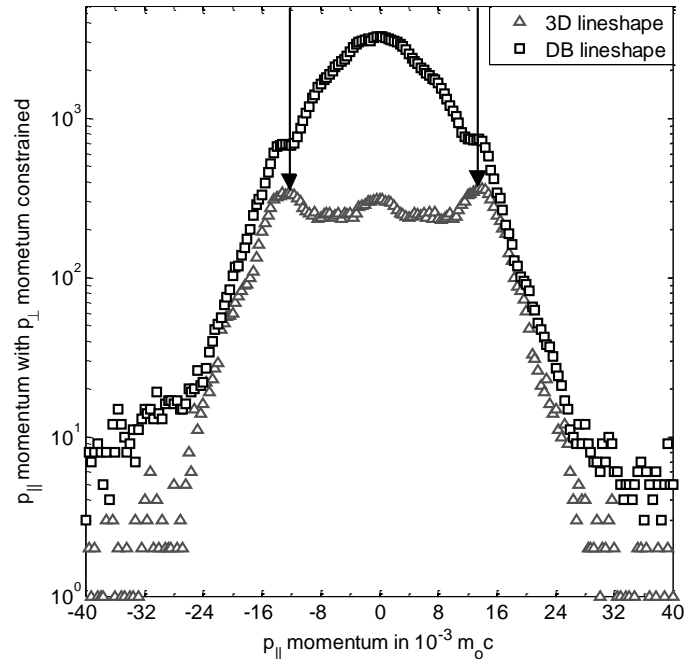


Figure 9: Coincidence DBAR (CDBAR) Results for O-ion irradiated 6H SiC from Williams [2], [3]. This shows the 3D momentum lineshape and Doppler broadened momentum lineshape.

2.1.3 3D Positron Annihilation Spectroscopy System (3DPASS)

Design and characterization of the 3DPASS, a unique PAS system based on the novel technique developed by Lt. Col. Christopher Williams, using a low energy positron beam (<50 eV) was accomplished by Capt. Stephen Jimenez [18]. The components of the beam system were designed, assembled, and characterized and but connection with the test chamber was not completed for use to test materials. A low-activity ^{22}Na source was used inside the test chamber (instead of the positron beam) to calibrate and characterize the system using virgin copper as a sample material. Virgin copper is a standard sample for aligning, testing, and characterizing momentum PAS systems because its ACAR and DBAR spectral features are well-known. This characterization and calibration

demonstrated the ability of the system to perform accurate measurements and prepared it for experimentation with additional samples.

2.1.4 EPR and ENDOR Studies of Point Defects in Lithium Tetraborate

Maj. Douglas Buchanan successfully identified several important point defects in various samples of virgin and transition metal-doped LTB using electron paramagnetic resonance (EPR), a spectroscopy technique for measuring materials with unpaired electrons, and electron-nuclear double resonance (ENDOR), a method described as EPR-detected nuclear magnetic resonance (NMR) which makes use of electron-nuclear hyperfine couplings [14]. The defects identified are useful in characterizing the structure and behavior of LTB, especially when it is doped with materials which add scintillating properties. The defects identified are used as a starting point for this work.

2.2 Positron work done at other institutions

Although not an overly common research topic in the field of nuclear science, work with positrons is slowly gaining more attention throughout the community. Much of the work in this field was performed several decades ago, with several materials being adequately characterized by means of PAS. However, work in this field became somewhat less common once the limits of technology seemed to be reached. More recently, advancements in detector technology along with the improved ability to interpret ACAR and DBAR results concurrently with results from other measurement techniques have allowed scientists the ability to revisit momentum PAS techniques. Work done by researchers such as A.C. Kruseman [19], investigating specific materials with defects while using some of the newer technology available to perform both ACAR and

DBAR calculations, has laid a good foundation for positron science. The work done by A. Baranowski et al. to design and characterize a new system for Doppler-broadened spectroscopy [20] showed the use of two-detector DBAR which reduced the background and allowed an energy resolution of 1.1 keV. Work designing, fabricating, and using a low-energy positron beam and trap to control positrons for use in PAS studies was accomplished by R. Greaves and C. Surko [21],[22]. The positron beam present at AFIT is modeled after this work. The foundations of the ideas used in the 3DPASS was based off of much of this previous work, with it being used as a springboard into trying novel techniques to make use of positrons as a means of characterizing materials.

III. Experimental Equipment

3.1 Double-Sided Strip Detectors (DSSDs)

The system incorporates two large high-purity germanium double-sided strip detectors (HPGe DSSDs). They are identified as Detector 0 and Detector 1. These detectors each have individual HPGe strips laid next to each other such that one face has 16 strips aligned vertically (AC side) and the other face has 16 strips aligned horizontally (DC side), creating a 16 x 16 matrix for spatially resolvable radiation detection of gamma particles. The names AC and DC are simply a naming convention. Figure 10 shows a picture of the DSSD, as mounted on a specially-designed translatable stage.

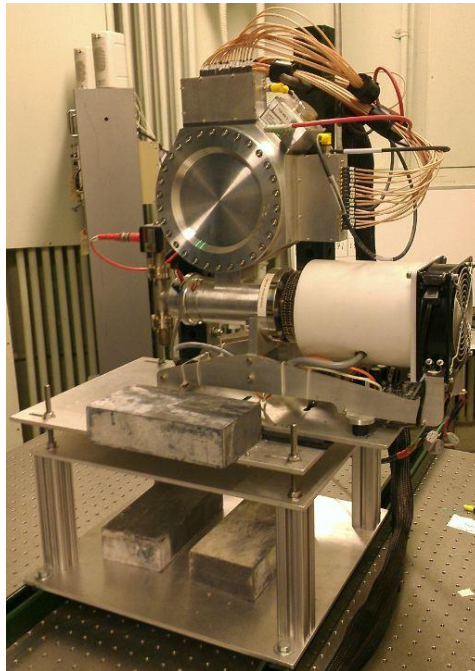


Figure 10: Picture of one of the Double-Sided Strip Detectors (DSSDs), made by PhDs Co., showing mechanical cooling system, translatable stage, and channel connections.

Two rubber padding sheets, each 1/8-in thick, were cut to size and inserted in between the DSSD and the stage on which it was mounted in order to attempt a reduction in vibrations throughout the detector through dampening. These vibrations degrade the minimum-achievable resolution of the crystals. Several lead bricks were placed in various locations around the stage as an attempt to help in dampening vibrations and reducing some of the radiation background.

For the DSSD, a larger detection matrix is actually present when subpixel interpolation is taken into account—for example, with 5 substrips per pixel, this would make an 80 x 80 matrix, useful for accurate determination of spatial charge deposition. The HPGe crystal provides the capability of achieving the energy resolution sufficient for CDBAR measurements (1.6 keV FWHM resolution), and the DSSD design takes advantage of subpixel interpolation methods which provide the spatial resolution required for 2D-ACAR and combined 3D-PAMMs.

3.1.1 DSSD Efficiency Calculations

Knowledge of the efficiency of each pixel and subpixel is necessary for proper characterization of the DSSDs and for properly interpreting data collected by them. For ACAR calculations, the subpixel efficiency directly affects the ability to spatially resolve locations of radiation events on the face of the detector, which affects the ability to detect small spatial variations necessary for an accurate ACAR spectrum. Figure 11 shows the original efficiency matrix of the DSSD as calculated by Williams et al. [3]. This map represents the long-term behavior of the DSSD. Clearly the most efficient part of each intrinsic pixel is its center. In other words, the subpixels located in the center of each pixel are more efficient at detecting incident radiation than the outer subpixels, because

of gaps in between strips on both the AC and DC sides. The strips themselves are 4.75 mm wide, and there is 0.25 mm of gap space in between each strip. A relative or normalized matrix can be developed which records the ability of each subpixel to detect radiation relative to the center subpixels, which can then be used to correct datasets for this decreased ability of outer subpixels to detect radiation as efficiently.

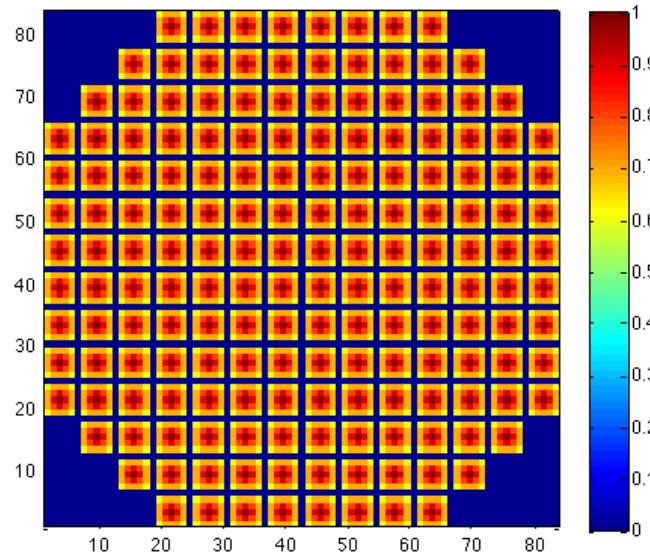


Figure 11: Original Efficiency Matrix of the DSSD as calculated by Williams [3]. Blue indicates low efficiency and red high efficiency.

Using a Mathematica code written by Maj. Angelo Bonavita, which is listed in Appendix C, new subpixel efficiency calculations were performed for the DSSDs. A ^{85}Sr source, which produces a 514 keV gamma very close to the desired 511 keV annihilation gamma, was placed 18 inches from each detector face for a period of eight hours per detector. After importing subpixel data already filtered for 2-strip simultaneous occurrence and for energy (514 ± 10 keV) in the Matlab parser, this Mathematica code bins the data into a matrix of pixels and then a matrix of subpixels. It then calculates the

mean efficiency and resolution across the detector with associated standard deviations. The extreme outer pixels have artifacts because of the lack of sufficient adjacent transient charge for subpixel interpolation on the outer edges, and therefore these can be discarded to give a more accurate result. Figure 12 below shows the contour mapping of counts detected across each detector in this experiment. The highest contours appear in the center of the pixels, which are 300 counts and higher. The contours decrease by 100 counts for each contour while moving away from the pixel centers. This map makes use of the subpixel data and the axes are labeled by subpixel location, making use of a 5x5 subpixel matrix within each pixel. The subpixel efficiency is clearly not uniform over the entire detector face for this dataset, although the general tendency is that each pixel appears to have the highest efficiency in or near the center. These maps would tend towards the calculated average efficiency matrix if the source was left for longer time periods (on the order of days). However, because of the shortened nature of this dataset a large relative error is introduced between pixels. The total number of counts in Detector 0 was 492,586 with 2786 the maximum in any one pixel; for Detector 1 the total was 483,695 with 2441 the maximum in any one pixel.

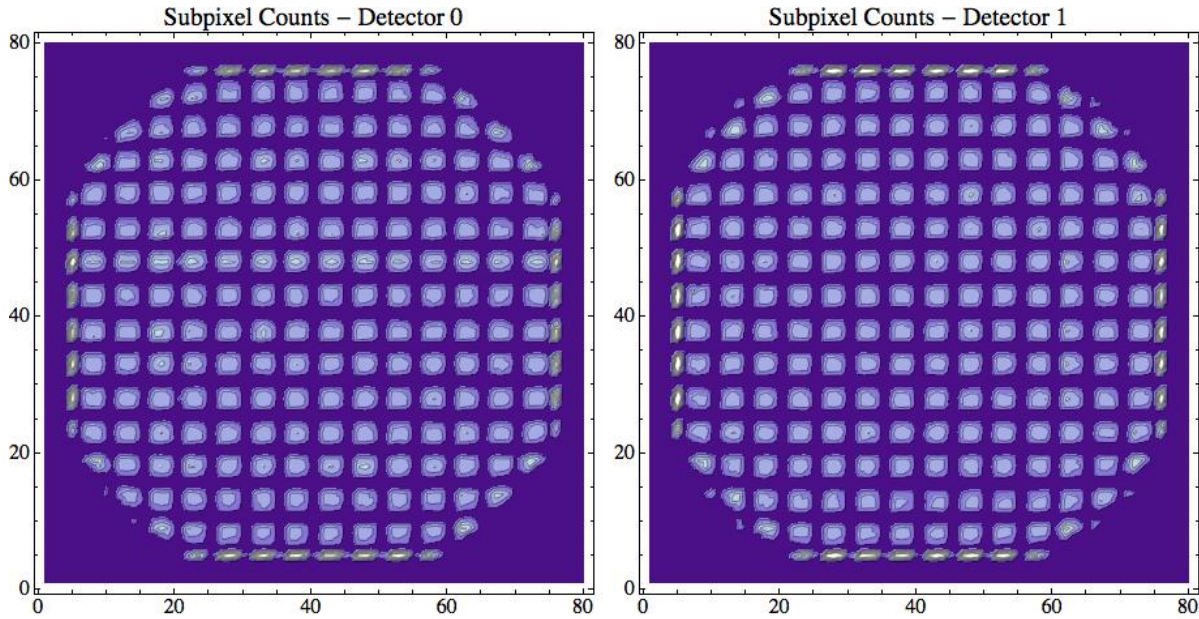


Figure 12: Subpixel mapping of counts detected using a 5x5 subpixel matrix in each pixel for each detector. Deep purple represents zero counts, and the contour value increases by 100 counts for each time the color gets brighter. The maximum contour in the center of some of the pixels is a 300 count contour line.

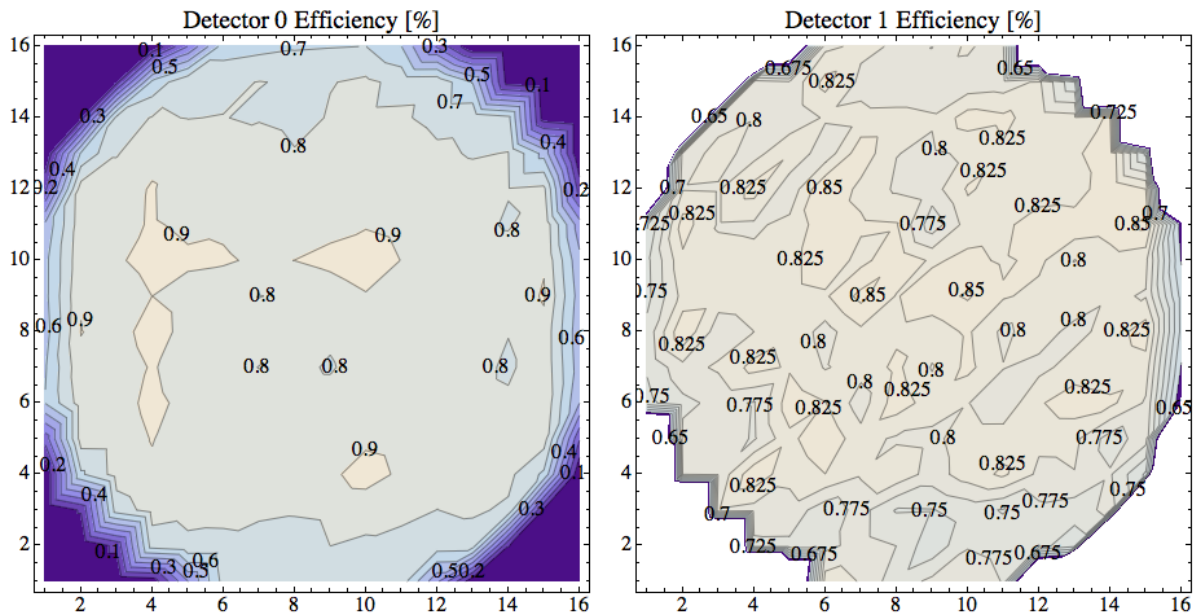


Figure 13: Subpixel efficiency contour plot for each detector, reported as percent values. Horizontal and vertical axes are labeled by pixel number.

Figure 13 shows a contour plot of efficiency values for the two detectors using the same subpixel data from the Sr-85 8-hour runs. These values, labeled by pixel location, are expressed as the percent of particles detected in each location versus the number of particles incident upon that location (intrinsic efficiency). Clearly, the overall efficiency of these detectors is relatively low because of the nature of germanium and relatively small thickness (~1 cm) of the sensitive area of the detector. However, their ability to spatially resolve in an efficient manner is invaluable for ACAR. Specifically, for Detector 0 the average efficiency across the entire detector face is $0.670 \pm 0.309\%$. The average efficiency with data from the outer two strips of each direction removed (such that strips 1, 2, 15, and 16 are removed from both the AC and DC sides for a ‘dense’ efficiency to correct for spurious data on the edges which results from the subpixel interpolation) is $0.847 \pm 0.042\%$. For Detector 1, the average efficiency across the entire face was $0.665 \pm 0.284\%$ and the ‘dense’ average efficiency, calculated as above, was $0.809 \pm 0.023\%$. Therefore, the efficiency appears to be essentially the same (uniform), within counting error, across the central pixels in each detector.

3.1.2 DSSD Resolution Calculations

Investigating the subpixel resolution across the face of each detector is important for knowing about both the capabilities and potential issues of the detectors. Specifically, for DBAR, the ability for the detector to distinguish between energy peaks which are very close together is vital. Again using the Mathematica code written by Maj. Angelo Bonavita (Appendix C), subpixel resolution calculations for the DSSDs were performed. Figure 14 demonstrates a contour plot of resolution values expressed as full-width at half-

maximum (FWHM) in keV for each detector, also calculated using the subpixel data acquired during the 8-hr runs with the Sr-85 source.

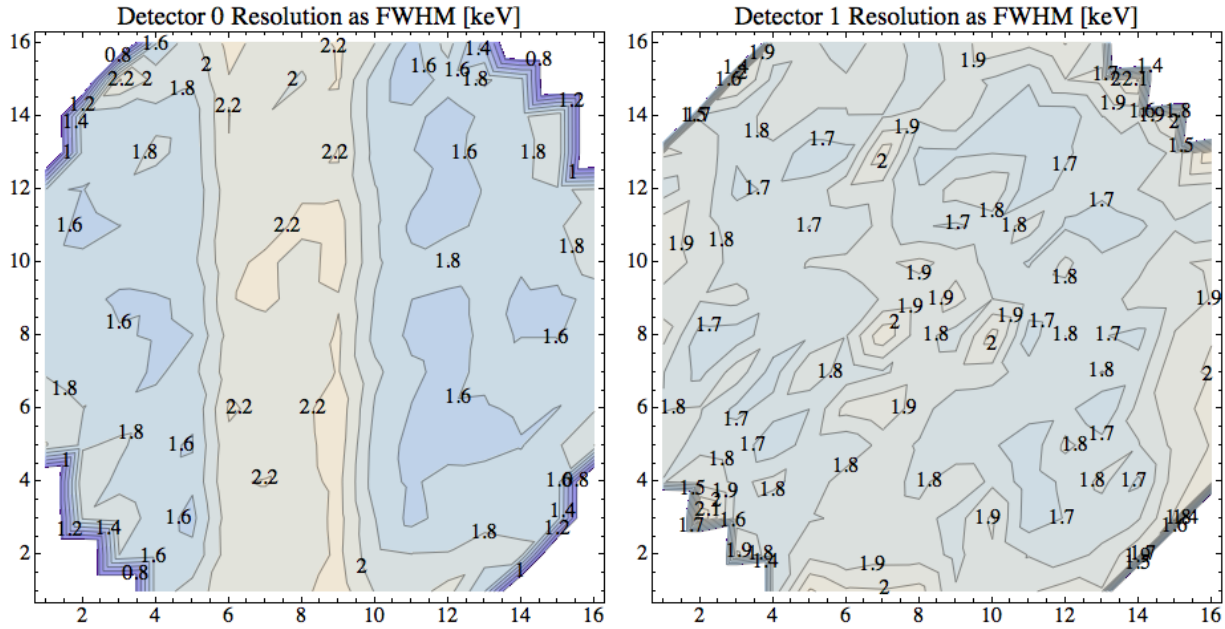


Figure 14: Resolution contour plot for each detector, reported as FWHM in keV. Horizontal and vertical axes are labeled by pixel number.

The resolution values reported for detector 1 are fairly uniform, although being somewhat larger than what is expected for this type of detector. Alternatively, there is a noticeable spike in the resolution values for several of the AC (vertical) strips on Detector 0 where the resolution is degraded as compared with the rest of the detector. This degradation in resolution capability could be indicative of a few of the AC strips being faulty or improperly connected, but is more likely due to the vibrational coupling of the strips with the mechanical cooling motor. This decrease in resolution for Detector 0 will negatively affect the results of the experiment, particularly for DBAR calculations. The average FWHM across all of Detector 0 was 1.631 ± 0.615 keV and the average across the ‘dense’ detector face with 2 outer strips removed on all four sides was 1.827 ± 0.252

keV, somewhat higher. For Detector 1, the average FWHM across all strips was 1.643 ± 0.540 keV and across the 'dense' face was 1.769 ± 0.088 keV. Therefore, the average resolution across the detectors was largely the same between the two detectors.

3.2 Electronics

A novel electronics package called Spect72 is used which provides for accurate and timely digital data gathering all in one convenient, low-footprint unit. The Spect72 interface box contains all necessary electronics for data gathering. It has the ability to receive 72 separate input signals. Its built-in digital electronics convert analog to digital in order to provide for spectral analysis. The associated Imager software allows for efficient data analysis with the ability to test and monitor each strip and to save multiple data types for each strip from each run. There is an autocalibrate feature for easy calibration of energy peaks. Figure 15 below shows a picture of the Spect72 with all 64 detector channels connected. The highest 8 channels of the Spect72 are unused.

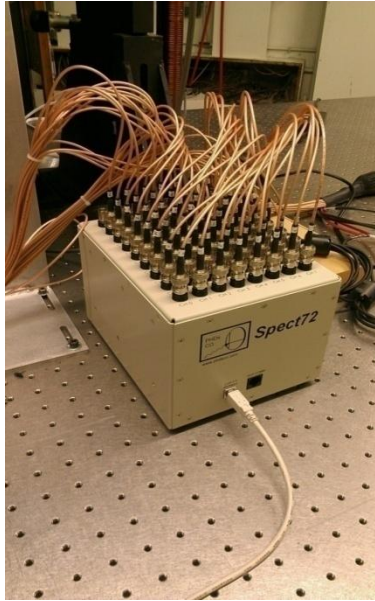


Figure 15: Spect72 digital data acquisition system.

The Spect72 has a motherboard with nine daughter boards. The inputs from each of the 72 separate input channels are distributed evenly across the daughter boards (8 channels per daughter board). Each daughter board has a 12-bit analog-to-digital converter (ADC) and two field-programmable gate arrays (FPGAs). The motherboard has a 20 ns clock cycle, meaning that the shortest measurable timing window between events in multiple strips is 20 ns.

The DSSDs themselves contain preamplifiers which condition the waveforms from the strips before they are amplified and sent to the Spect72. Separate power controller boxes are used to turn the preamp power on and off, control the high voltage (HV) bias, and other settings on the DSSDs. The HV bias setting used in this work was -600 V for each detector, a negative voltage bias. The preamp power must be energized prior to HV being applied.

3.3 Vacuum System

3.3.1 Vacuum Chamber

The vacuum chamber used in this experiment is a medium-sized chamber made from stainless steel by MDC Corporation. Air is evacuated from the chamber in order to reduce contamination in the signal from annihilations occurring with the air. This is important since there is about a 0.5 cm gap in between the source and the sample. This gap is necessary because of the requirement to shield the source and not the sample from the detectors. In its current configuration, it is able to pump down to around 5×10^{-5} Torr and maintain that pressure indefinitely with the vacuum pump in continuous operation. Falling in the high-vacuum (HV) range, this pressure is the highest vacuum achievable for this setup because of some of the bolts and nuts being old, stripped, and/or overused; the presence of a rubber gasket in the flange where the manipulator controls are connected; the use of large quantities of lead inside the chamber which outgases and contaminates chamber surfaces easily; and a lack of enough bolts to completely fill every single flange hole when sealing the chamber. When these problems are corrected or alleviated the chamber could achieve a lower pressure, which will be necessary for beam use. The beam section will be at around 10^{-7} Torr or lower, and this difference in multiple orders of magnitude would make beam operation impossible.

The target chamber contains multiple openings of different sizes designed to provide access points for experimental processes, measuring and monitoring equipment, and internal access. The two main openings, which are sealed by custom-made 8-in. steel conflat flanges during normal operation, are located with their centers along the detector axis of the setup on opposite sides of the chamber. These circular flanges have most of

the steel in their immediate centers (3-4 cm diameter) bored away except for a relatively thin (2-3 mm thickness) portion so that desired annihilation gammas may pass through relatively uninhibited while maintaining a vacuum seal on the system. On the side of the chamber closest to the positron beam is a grouping of five 4.5-in. circular openings which are oriented at different angles with respect to the center of the chamber. Four of these are sealed with thick glass flanges for observing the inside while maintaining pressure inside the chamber, while the fifth one has a gate valve and the vacuum pump connected to it. Of the 4.5-in openings on the beam side, the one which lies along the beam axis of the setup (directly perpendicular to the detector axis), is the opening that will be used to connect the positron beam to the target vacuum chamber. A 61.2 cm-long tube with a solenoid coil surrounding it and a separate bellows connector will bring the beam and the target chamber together so that the entire system may be under high vacuum, around the same pressure. The remaining openings (either 2.5 in or 4.5 in) are either sealed with a steel flange, a glass flange for observation, or a flange which connects the two vacuum pressure gauge instruments. The chamber allows the possibility of connecting an ion pump as well, which would further reduce the pressure. Figure 16 shows a picture of the vacuum chamber with the layout of the axes overlaid.

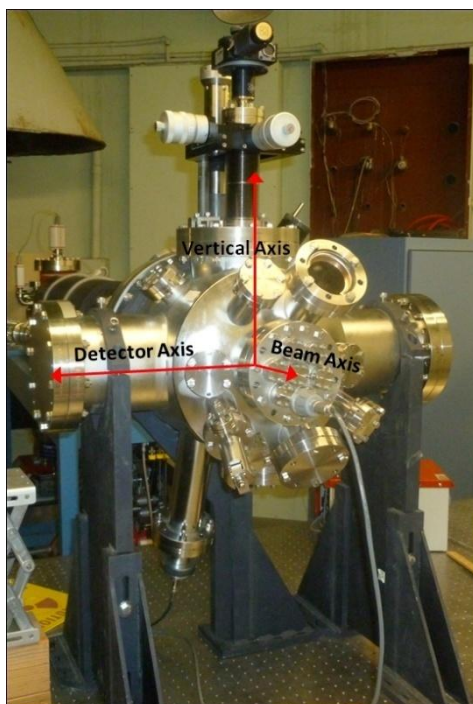


Figure 16: Vacuum Chamber with axes overlaid [18].

3.3.2 Vacuum Pump

The Pfeiffer HiCube HiPace 80 Eco pump (see Appendix D), was used to pump down the vacuum chamber. It is a turbopump made in Germany, and typically operates at 1500 Hz. In order to get up to full speed and maintain pump-down, the vacuum chamber must be able to sustain a pressure of at most 1×10^{-3} Torr. If the pump does not achieve at least 1200 Hz within a few minutes, it will automatically shutdown to prevent overwork. If it cannot cycle up further to 1500 Hz after a significantly longer period of time it will likewise turn off. The pump was connected to the chamber via a manual gate valve, which has a hand crank used to open and close the valve. If the chamber could maintain a pressure over an extended period of time, this valve would be used to seal off the chamber and thus the pump could be removed. This was not achieved in this work, as

the pressure would increase by a few orders of magnitude not long after the pump was turned off. Ultimately, under ideal circumstances in the volume to be pumped down, this pump is capable of achieving 10^{-11} Torr minimum pressure. The pump and the manner in which it was connected to the vacuum chamber are shown in Figure 17.

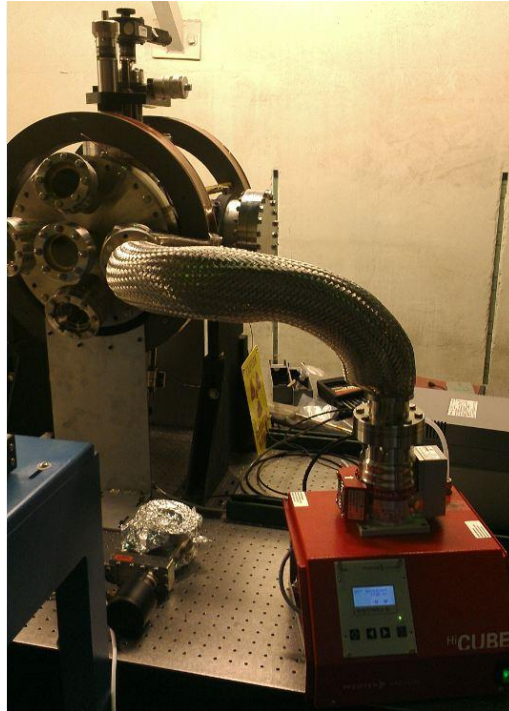


Figure 17: Picture of the Pfeiffer HiCube HiPace 80 Eco turbopump and its connection to the vacuum chamber using a mechanical gate valve.

3.3.3 Vacuum Gauge

The vacuum gauge monitoring unit used in this experiment was the Varian XGS-600 (see Appendix D). This unit was used with two separate gauge instruments attached into the vacuum chamber in customized flange connections. First, the ConvecTorr P-type thermocouple vacuum gauge (referred to as CNV1), was used for monitoring the higher range of pressures while pumping down from atmosphere (760 Torr) to 1.0×10^{-4} Torr, which is the lower limit of this gauge. Second, the IMG-300 inverted magnetron gauge

(referred to as IMG1) was used for the lower range of pressures ranging from 1.0×10^{-3} to 1.0×10^{-11} Torr. The two gauges were connected to the monitoring unit with cables and could be activated and deactivated independently, although the lower range gauge should not be turned on while the pressure is too high as it could cause damage.

3.3.4 Manipulator Rod

The vacuum chamber has an attached manipulator rod which can precisely position a sample inside the chamber using four dimensions: X, Y, Z, and rotation angle θ . For this experiment, X is taken to mean the beam axis, or the axis which runs parallel with the positron beam; Y is taken to mean the vertical axis, or the axis which runs perpendicular to the optics table on which the experiment is mounted; Z is taken to mean the detector axis, or the axis which runs perpendicular to the detector faces (from one detector through the sample to the other detector); and θ is taken to be the rotation angle of the sample around the vertical axis.

This manipulator rod can be controlled from outside the top of the chamber, even while the chamber maintains its vacuum pressure inside. It appears to be made from steel or a similar substance. Throughout the course of this work it was decided to use lead to shield the manipulator rod from the detectors so stray positrons finding their way into the rod and subsequently annihilating would not contaminate the signal. Unfortunately, this was not done for the Cu-doped sample, which was the first to be tested; it was only done for the virgin and the Ag-doped samples, which were tested later.

3.4 Radioactive Sources

3.4.1 ^{85}Sr

For energy and efficiency calibrations in PAS the radioactive isotope ^{85}Sr (strontium-85) works well because it naturally produces a 514 keV gamma particle, which is very close in energy to the 511 keV annihilation gamma photon. It produces these gammas without also producing beta particles, which allows for less radiation interference and exposure. For this experiment a 100.8 μCi nominal ^{85}Sr source assayed in July 2012 and made by Isotope Products Laboratories as number 1613-11 was used (Appendix D). A planchette source, this source contains a rather small radioactive portion inside a larger plastic disk and is labeled on the surface of the disk. The disk itself is 2.5 cm in diameter and 5 mm thick. This ^{85}Sr source was used in performing the energy calibration with the two HPGe DSSDs over a 24 hour period. It was used again with each DSSD individually once the energy calibration was applied in order to perform the efficiency calibration over an 8-hour period for each detector. The source was placed 18 inches from each detector face on a platform during the efficiency calibration runs.

3.4.2 ^{22}Na

^{22}Na , as a natural source of positrons through positive beta emission, was used to passively project positrons onto the samples tested in this experiment. Several ^{22}Na sources were available, but the one used throughout data collection was a 1.0 mCi nominal ^{22}Na source, assayed on 10 January 2012, designated B009 (Appendix D). Produced by North American Scientific, this was the strongest available ^{22}Na source for the passive annihilation source-sample configuration. Over the course of data gathering,

this source ranged from 760-780 μCi in actual activity. Figure 3 shows an image of the B009 ^{22}Na capsule source, extended from its tungsten container.

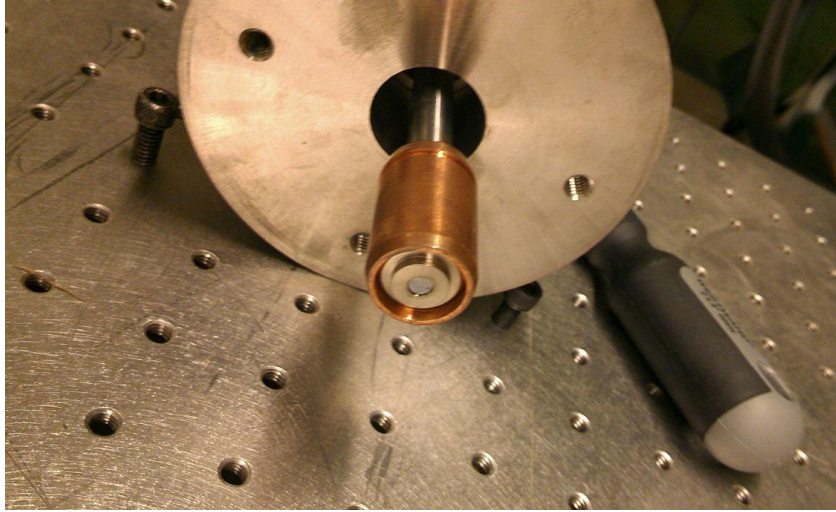


Figure 18: 1.0 mCi ^{22}Na B009 capsule source used in this experiment. The radioactive portion is a small disk located at the end of the copper capsule, under a thin titanium film, in the foreground.

Additional sources were available and are listed in Appendix D. All three of the sources with lower activity than the 1.0 mCi nominal source were determined to be too weak for reasonable counting times and therefore not used. Sources B009 and B008 were both capsule sources, with the active portion a small, thin disk with a hollow center under a thin 10 μm titanium foil on one end of a larger copper, cylindrical, bullet-shaped capsule. The capsule itself was 3.2 cm long and 2.5 cm in diameter. The fact that the strongest source was in this configuration drove the redesign of the source-sample mounting piece. Sources 115163 and 115162 were both a thin film disk design with large diameters. Since these disks resembled planchettes, they could have easily been mounted in the original source-sample holder, but they were far too weak.

One additional ^{22}Na source available was the Cu Standard Source (CuSS): this contained 23.3 μCi of $^{22}\text{NaCl}$ solution on two identical Cu samples placed in a sandwich configuration; this was assayed on 18 Jan 2012 [18] and was originally used to properly align the sample between the two detectors. However, it was determined that this source was too weak to be of any use in this work. Additionally, although the pieces of copper in the CuSS were pure, they could not be used with the stronger 1.0 mCi ^{22}Na source for alignment because the CuSS was sealed with a plastic laminate. Betas would tend to annihilate with the plastic before penetrating to the Cu inside. Alignment was performed using a piece of copper cut from a Cu gasket instead.

3.5 Shielding

The primary material used for shielding was lead. This material is dense enough to block gamma radiation of the kind present (511 keV and 1.275 MeV gammas) with relatively low thickness of material. In previous work on this system [18], a configuration of thin sheets of malleable, layered lead which were folded to wrap around the original source-sample configuration whilst hanging from the manipulator rod, were positioned in such a manner that they blocked most of the radiation originating in the positron source from the detectors but allowed radiation originating in the sample material to pass to the detectors relatively unabated. Through system characterization it was determined that the total thickness of the layered lead on either side of the source was insufficient to completely block annihilation radiation origination from within the source itself, and therefore an improved configuration was adopted.

In this work, a lab jack was placed inside the vacuum chamber and allowed to sit on the floor of the chamber. It was raised up to the appropriate level and smaller lead bricks were placed on the lab jack and around the source/sample holder in such a manner that the newer source could adequately be blocked while the annihilation gammas originating from the sample were allowed to freely pass to the detectors. The lead bricks were 3 in x 2 in x 1 in. Placing three of these depth-wise on either side of the source allowed 3 inches total of lead shielding on each side. The characterization performed in [18] showed that 3 in of lead is sufficient to block the 511 keV gamma and the 1.275 MeV gamma. Additional bricks were used to shield gammas coming from the manipulator rod and the copper sample support wire. Another brick was placed width-wise on its side to provide shielding in the direction where the lab worker would most commonly be. In addition to removing contamination of the spectral signal, the lead serves to lessen exposure in the immediate area of the chamber. One potential issue with the lead in this configuration is that it is not angled along the direction moving radially away from the sample. It simply is flat, which could reduce the amount of coincident gammas detected on the lower portions of the detector faces or could even potentially reduce some of the higher angular deviations seen in the data.

IV. Experimental Procedure

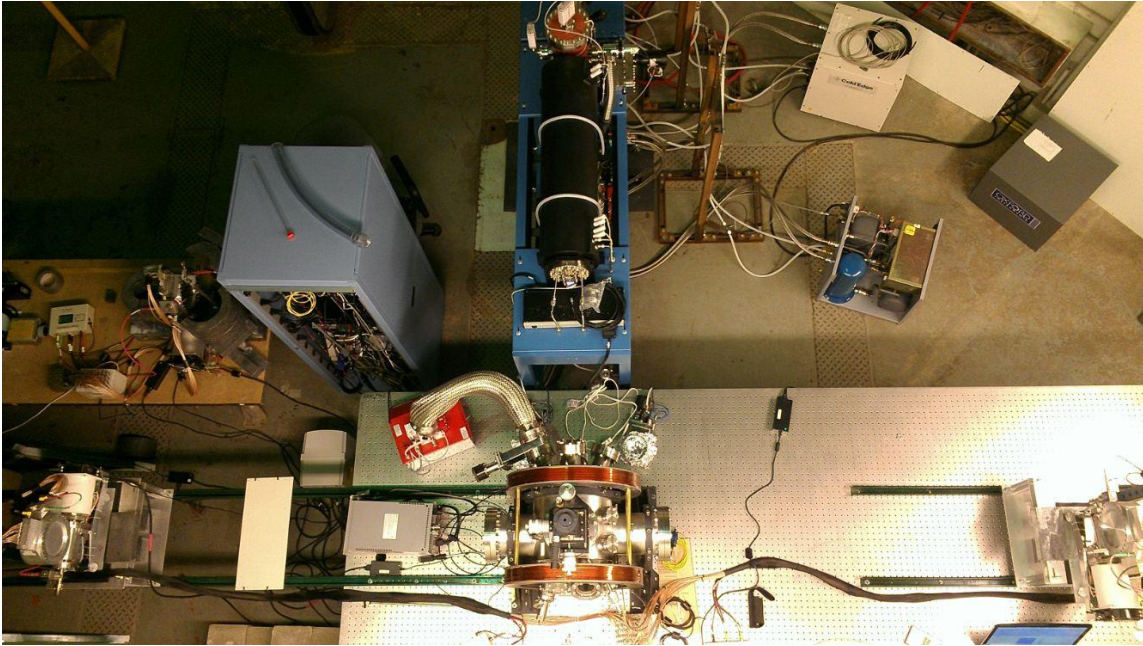


Figure 19: Overhead layout of the three-dimensional positron annihilation momentum spectroscopy (3DPAMS) experiment.

4.1 Source-Sample Configuration

The system can be used by placing the source right next to the sample in the source-sample configuration. In this way, annihilation is passively accomplished. The annihilation rate of positrons within the sample, and therefore the full-energy coincident event count rate, depends upon source strength. Figure 20 below shows the layout of the source-sample configuration in more detail.

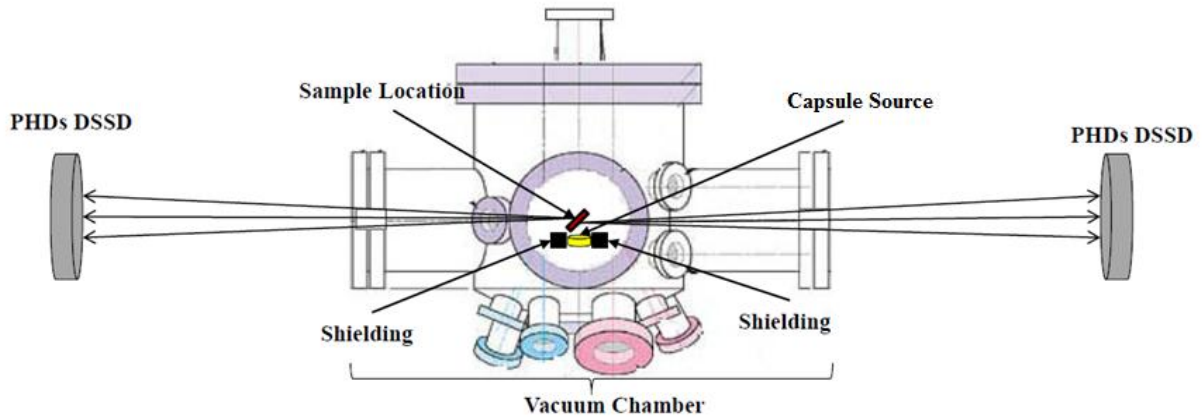


Figure 20: Source-Sample Configuration, adapted from [18].

Originally a source-sample holder was designed out of plastic which hung from the manipulator rod such that a planchette source could be inserted at a 45 degree angle to a flat sample. This holder allowed the source to be shielded from the detectors by lead which hung over it while allowing the sample to be in direct line with the centerline of the two detector faces and unshielded. This holder is described in [18].

The flat sample would be exactly parallel to the detectors faces so that if it were a crystal cut at a known plane, that plane would be what was visible to the detectors. It has been proven that the crystallographic orientation of the sample can affect the location of momenta features in samples [18].

Because of the size and shape of the newer, stronger 1.0 mCi nominal ^{22}Na source, the source-sample holder required a redesign for this work. The limiting factors of the redesign included: the cylindrical, bullet-like shape of the source; the source's width and height; the fact that the source contained its radioactive portion in a thin disk on one end so that the most intense point would be directly over that end; and the fact that the source needed to be shielded by sufficient amounts of lead. An image of the new

source-sample holder, made from aluminum and fabricated by the AFIT machine shop, is shown in Figure 21.

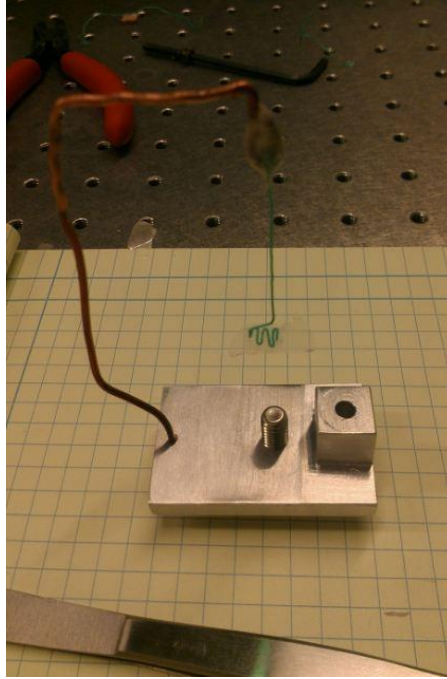


Figure 21: Newly designed source-sample mount fabricated by the AFIT machine shop.

This new source-sample holder needed to have the sample on the opposite side of the manipulator rod as compared with the older plastic holder because of the limits in the horizontal (beam) axis and the width of the source. This holder pushes the lower limits of the vertical axis of the rod because of the necessity to have the source located below the sample for ease of shielding. The holder would extend even further downward to allow more room for movement in the negative vertical axis direction except that the lab jack on which the lead bricks are supported can only move so far downward. The sample is hung directly over the source at a 45-degree angle in order to maximize the surface area of the sample being exposed to the source and the surface area of the sample being

presented to the detector faces simultaneously. The sample is hung over the source using a combination of two types of wire. A thicker, 1/16" diameter (AWG 14), stiff copper support wire attached to the base of the mount comes up roughly 5 in and then bends over at a 90 degree angle towards the center of the mount. Another bend allows it to provide a mounting hook directly over the center of the source below, in the center of the mount's base. A very thin, easily bendable but sturdy insulated electrical wire (0.5 mm diameter) is hung from this mounting hook and the sample itself is taped to the end of the thin wire. A second alternative for the copper support wire would be to attach it directly to the manipulator rod at the proper height, but this method was not used due to difficulty in proper sample alignment.

The simplicity of this first-iteration design for the new source means that while the source and sample are at 45 degrees to one another, the sample is at 45 degrees with respect to the detector faces and therefore for thin crystal samples cut at known planes, the exact plane being presented to the faces is not precisely known. This plane could be guessed knowing that the sample has been rotated 45 degrees from a known plane in one of two directions, but the exact plane would be unknown. A further iteration of this design would require that the holder be designed to accommodate mounting the source at a 45 degree angle with respect to the horizontal axis and the sample straight up and down (along the vertical). This would allow the 45 degree angle between the source and sample to be maintained while keeping the known crystal face parallel to the detector faces.

4.3 Mounting a Sample

The older source-sample holder allowed relatively quick source and sample insertion, requiring removal of only one of the mid-sized 6 in flanges for access to the holder mounted inside the chamber. The mount could be left on the manipulator rod and simply rotated around for access to each of the two insertion points – one for the source and the other for the sample. The sample would always be at the same location in reference to the manipulator rod. The rod would then be set at the proper location using the controls at the top of the chamber to ensure that the sample is correctly aligned. Then the folded lead sheets would be placed over the source side of the mount, although it was proven that the amount of lead that could be mounted in this fashion was insufficient to completely block all gammas originating from within the source [18]. This process would take about 20-30 minutes to complete a sample exchange if the chamber was sealed and pumped down to start with. This doesn't include the extra time required to reseal the chamber with a new gasket and pump it down to the necessary pressure.

The newer aluminum source-sample holder requires a significantly longer amount of time to mount a sample properly. Sample exchange takes more on the order of 2 to 2.5 hours, starting from a sealed system and not including time to reseal and pump down again. Because of the design constraints with the larger source and the use of additional lead shielding, more work is necessary for a sample exchange. One of the larger, 8 in conflat flanges must be removed. The lead bricks surrounding the source must be carefully removed, and the lab jack lowered and pushed aside. After carefully removing the source and securing it inside its Tungsten holder for safety in order to minimize exposure time while working, a 9/32-in Allen wrench is used to remove the aluminum

source-sample mount with the sample still attached. The old sample is carefully removed from the wire. For the new sample, a new thin hanging wire is used. Its end is bent and folded into an accordion shape for maximum surface area and then double-sided tape is used to secure the back of the sample crystal to the accordion-shaped end of the hanging wire. Great care must be used to ensure that the sample itself completely blocks all mounting items from the source below—neither the double-sided tape nor the hanging wire may extrude beyond the perimeter of the sample. Other PAS experiments have used different methods to ensure that the signal is not contaminated by annihilation gammas originating in the mounting material or source. For example, an experiment performed by A.C. Kruseman [19] showed the use of small sticks to mount the sample, with the source hanging above the sample and the sticks below the sample. In Kruseman's work everything but the sample was shielded from the detectors by large quantities of solid lead inside the chamber, angled for gamma emission swath allowance. The sample is thick enough (~2-3 mm) so that it shields the sticks from the positrons incident from the source.

Continuing in this work, the sample and hanging wire are attached to the copper support wire. Having drawn an extended 45 degree angle on paper using a protractor, the sample wire is bent so that the sample perfectly aligns with the 45 degree line as compared to the horizontal. Figure 22 shows this process.

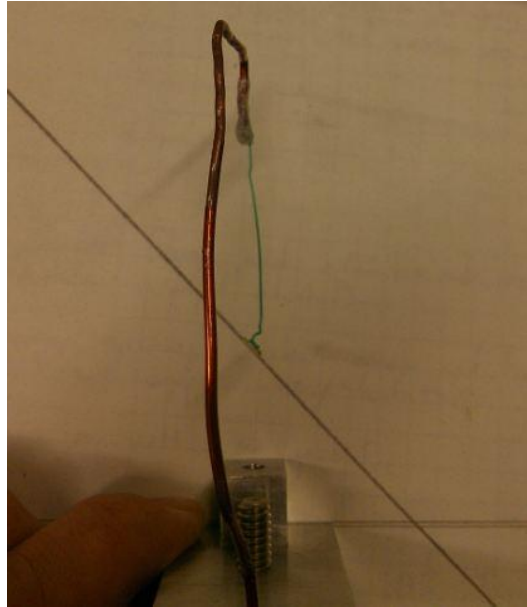


Figure 22: Aligning the sample at a precise 45 degree angle with respect to the base of the mount.

All samples in this work were mounted with the top of the sample rotated towards Detector 1 and the bottom rotated towards Detector 0. The sample was hung using a careful process to ensure proper sample positioning, with the sample center being a specified distance from the bottom mount shelf and also from the edge of where the manipulator rod would be. This was done since the wire was bendable and part of it was replaced each time a sample was exchanged. With known values on the manipulator rod and known distances of the sample center from parts of the holder, the sample's precise location would be known in each run and could be adjusted if need be for proper alignment. The sample would end up being directly over the center of the source, and about 0.5 cm above it.

The aluminum mount with the sample attached would then be reattached to the manipulator rod. The lab jack would be moved into place after placing the source back on

the screw which held it in place on the center of the aluminum mount shelf. The lead bricks would be placed in their appropriate locations and the lab jack would be raised to the correct height to shield the source, but not the sample. A visual check would be done to ensure basic qualitative sample and lead brick alignment. After this rather lengthy exchange process, then the chamber could finally be resealed with a new gasket and pumped down. Only with processed data can one truly tell the exact sample alignment.

4.2 Energy Calibration

Prior to any actual data collection taking place, the entire system must be run in its normal configuration using the ^{85}Sr source in order to calibrate the detectors for energy. Because of manufacturing processes, environmental and background influences, electronics and software processes, power fluctuations, and equipment connections, there is potential for the detectors to become improperly calibrated. Each strip in each detector has the potential to see incident particles of identical energies in a different manner, so they will most likely report different energy values for a source of a single known energy. This is corrected using an energy calibration. The 514-keV gamma produced by ^{85}Sr is close enough in energy to the desired 511 keV gamma that the calibration at that energy is correct for the desired energy.

The ^{85}Sr source was placed inside the vacuum chamber, in the source-sample holder where the sample would normally go. A 24-hr data set was taken with both detectors simultaneously, which showed many of the 64 total strips with energy peaks deviated from 514 keV, although some of the strips were precisely on 514 keV. The typical deviation was around ± 6 keV. The autocalibrate feature was then used in Imager

to correct each strip individually by inputting guesses for base to height ratio and FWHM of the peak along with values for the minimum number of counts to consider in the peak. After correcting all 64 channels, the complete settings file and a separate calibration file were saved for this configuration. The calibration file itself is a text file which records correction values for each channel of the spectrum and converts those values to keV. In all subsequent data collection runs, these settings and calibration files were applied prior to beginning each run. Figure 23 shows how the 32 strips from Detector 1 all clearly report the peak at 511 keV correctly for 24 hours worth of actual data from one of the samples due to application of the energy calibration.

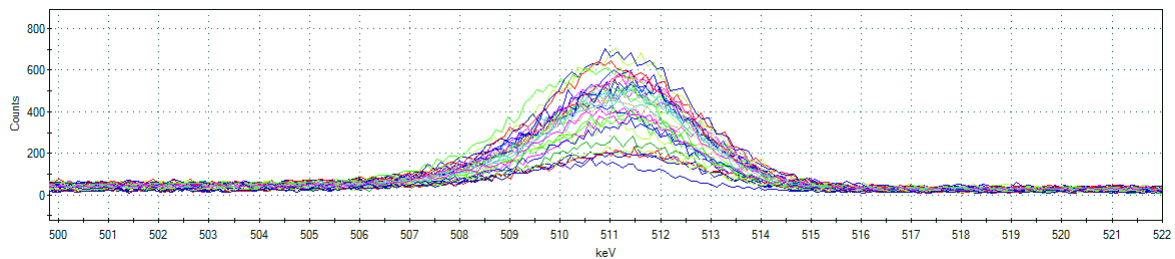


Figure 23: Energy calibration for each strip of Detector 1 at 511 keV.

4.3 Efficiency Calibration

Upon achieving a correct energy calibration, the next step was to acquire data for an efficiency calibration, again using the ^{85}Sr source. Ideally, this would be done over a sufficiently long period of time (on the order of the same amount of time for measuring an actual sample, 10-18 days or so) with the source in the same position as the sample would be inside the chamber and on the source-sample mount. Time constraints required this process to be accomplished by placing the ^{85}Sr source in front of each detector

individually at a significantly closer distance. Since radiation fields fall off quickly with distance, moving the source closer to each detector increased the exposure rate and solid angle at the expense of getting precisely correct efficiency data for the eventual location of the sample.

The data taken using ^{85}Sr for the efficiency calibration was the same data used for the DSSD efficiency calculation discussed earlier. This was done with data collection taking place for both detectors, but the code used to process the data sorted through it so that data was correctly attributed to its location of occurrence. The Matlab efficiency correction code entitled `ThreeDPASSEfficiencyCalc`, written by Capt. Stephen Jimenez (listed in Appendix C) was used to read in all 2-strip events from these data runs after file parsing. This code then generated pixel-normalized efficiency matrices for each detector based on the locations of the 2-strip events. These matrices were saved for later application in the combined ACAR and DBAR calculations. Figure 24 below shows the normalized efficiency values determined for each subpixel by the `ThreeDPASSEfficiencyCalc` routine for the two 8-hour ^{85}Sr datasets combined into one large dataset. In this work, there were three main ways in which the data for LTB samples were later corrected for efficiency: using a pixel-normalized subpixel efficiency correction, a detector-normalized average subpixel efficiency correction, and the average subpixel efficiency values calculated by Lt. Col. Christopher Williams [3].

The first method, the pixel-normalized efficiency correction (specific to each pixel), made use of the matrices as calculated from the `ThreeDPASSEfficiencyCalc` routine. In this method, the subpixel containing the maximum number of counts in each

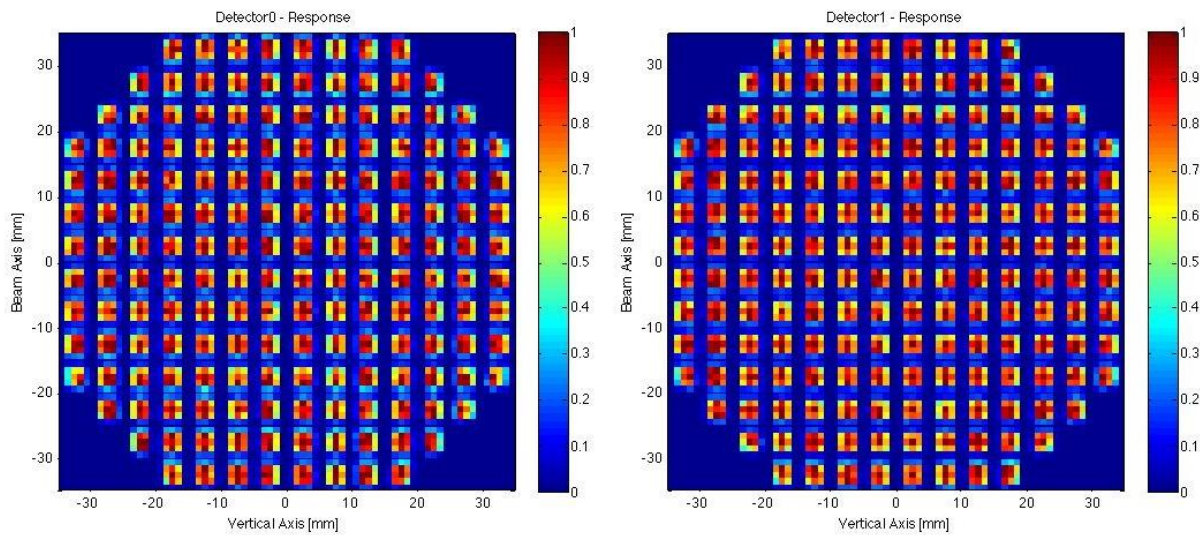


Figure 24: Individual detector response from efficiency calibration run. These datasets were used to generate the efficiency correction matrices which were later applied during the ACAR and DBAR calculations.

pixel is assigned a normalized value of one, and the other subpixels in that pixel are assigned values based on the ratio of number of counts in each of those subpixels as compared to the maximum number of counts in that pixel. In this method, each pixel is treated individually to account for differences between pixels. The resulting normalized matrix correction is used to ‘boost,’ or compensate for, the subpixels with low efficiency for better analyzing datasets with sample materials by normalizing counts detected in datasets by the efficiency correction. Because of the limited nature of the calibration run with ^{85}Sr (imperfect statistics over only 8-hour runs), the pixels across each detector face yield very different patterns, and this results in a rather noisy correction with high error due to variability between pixels.

The second method, the detector-normalized average subpixel efficiency correction, made use of the number of counts in each subpixel for a particular detector

from the ^{85}Sr data in order to calculate an average subpixel efficiency matrix for all pixels in that detector. Because of the relatively uniform efficiency across the central portions of each detector face, as was calculated in subsection 3.1.1, one can take the counts in a particular subpixel and average it with all the other count values from subpixels in the same location across all pixels in a particular detector, and then have an average count value in that subpixel. This is done for all 25 subpixels, and then the average count values in this 5x5 matrix are normalized such that the highest number in the central subpixel is assigned a value of one and the others are given ratio values as compared to this central average count value. Then, this averaged normalized matrix can be used across all the pixels, assuming all pixels will be the same across the detector. This tends to reduce error in the correction by compensating for the statistical uncertainty in the limited ^{85}Sr data runs, but at the same time the error associated with each subpixel is propagated across the entire detector face. Figure 25 shows the average subpixel efficiency correction matrices for each detector, calculated using data from the ^{85}Sr efficiency calibration runs.

Detector 0					Detector 1				
0.02	0.18	0.22	0.17	0.02	0.02	0.16	0.18	0.15	0.01
0.06	0.78	0.95	0.72	0.05	0.04	0.75	0.91	0.69	0.03
0.06	0.83	1	0.77	0.05	0.04	0.82	1	0.77	0.03
0.05	0.71	0.88	0.64	0.04	0.04	0.70	0.87	0.64	0.03
0.02	0.18	0.22	0.16	0.02	0.02	0.15	0.17	0.14	0.01

Figure 25: Average relative subpixel values calculated for each detector using efficiency calibration data.

The third method used for generating a correction for efficiency was applying the same average subpixel efficiency correction matrix calculated by Lt. Col. Christopher Williams for the original PhDs Co. DSSD [3]. Figure 26 below shows this matrix. This method, although proven to be effective in previous work, is less reliable here because it does not make use of the ^{85}Sr data collected with these particular DSSDs in this particular configuration, but is useful for comparison.

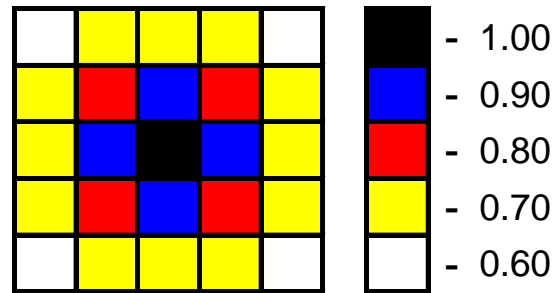


Figure 26: Subpixel average relative efficiency for the PhDs DSSD determined by Williams [3].

4.4 System Alignment with Copper Sample

The sample itself must be properly aligned such that its center is directly in line with the centerline of the two detector faces which extends along the detector axis. At first the sample is placed roughly in the center of the chamber by looking from the approximate center of one detector face and looking through the opening of one end of the vacuum chamber (with the 8-in conflat flanges off) to see how well the sample sits in relation to the approximate center of the 8-in openings (utilizing the concept of perspective). Then the sample is adjusted as necessary. Figure 27 shows a picture of how this alignment appears. This is useful to get an idea of how the sample ultimately sits inside the vacuum chamber.



Figure 27: Performing a visual alignment of the sample in relation with the chamber openings and detectors.

Afterwards a distance-measuring laser is used to get a more accurate reading. The laser is placed with one end in the approximate center of one detector face and it is shot through the approximate visual center of the chamber to the approximate center of the opposite detector face in order to see if it passes through or hits the sample. The laser is also used to gain knowledge of distances from each detector face to the sample location (manipulator rod) to ensure the distances are equal on each side. The sample is then adjusted accordingly. A more accurate way to ensuring alignment using the laser beam would be to shoot the beam down the center line and place the sample holder at four separate (X, Y) locations, making a square in totality, around four of the limiting corners

of the laser beam. The manipulator settings for each location are noted. The exact location for placement along the centerline is known to be within those four locations. The two 8-in openings of the chamber would have saran wrap on them with a hole or marked circle in the precisely measured center for the beam to pass through on either end. This particular ‘square’ method was not used in this work; only the visual perspective method with a laser for verification was used for aligning the sample. However, this ‘square’ method was used in [16] to initially align the detectors with the chamber, and this work made use of the same sample-detector alignment.

Once the approximate visual method is complete for getting a general alignment, a more precise technique is used for getting a perfect alignment. Previously, gathering data with the CuSS was performed to see exactly where the center of the sample was located. This is possible since virgin Cu ACAR spectrum is well known: Cu has its most intense ACAR peak exactly at the center of an ACAR spectrum, meaning that the majority of annihilation radiation coming from within the Cu has no angular deviation between the two gamma particles. Cu is a commonly available material in the lab and is easy to work with. The nature of the new source required a new Cu piece to be used: a roughly 1cm x 1 cm piece was cut using a low-velocity diamond saw from a used copper vacuum gasket. The piece was a keystone shape due to the circular nature of the gasket. This piece was put in place in the same configuration as a sample, hanging above the positron capsule source and data sets were recorded. The larger size and thickness of this Cu sample made it easy to generate large numbers of coincident events in a short time period for quick processing and subsequent realignment. An initial 24 hour data set was taken, showing misalignment by about 10 mm towards the beam in the X (beam)

direction and 2 mm downwards towards the optics table in the Y (vertical) direction, which was largely consistent with the misalignment that had been seen in the Cu:LTB sample (shown later graphically in the Cu:LTB results section), which had been measured already prior to using this Cu gasket piece to confirm the misalignment. This was followed by a three hour data set with the sample moved by 2 inches along the beam axis closer towards the beam. The newer set clearly showed a better alignment, such that the sample was moved an additional 0.3 in towards the beam and then a 22-hr data set was taken to verify proper alignment. When the Cu sample was properly centered, the exact manipulator settings were recorded, as well as the exact distances from the bottom shelf of the mount to the center of the sample and from the edge of the manipulator rod to the center of the sample. In this way, the exact location of the sample for proper alignment would be known and could be consistently applied.

The first sample measured, the Cu:LTB, was taken without properly aligning the sample beforehand. Moving this sample slightly in the X or Y directions did not seem to change the ACAR spectrum at all. This was most likely due to not moving the sample significantly enough to affect a change in the data output. The decision to use the Cu gasket piece to align was made after learning this. Moving the Cu gasket piece by a significant amount did in fact change the ACAR spectrum and the location of annihilation gammas on the detector faces significantly. Knowledge of the proper center location meant that samples measured subsequently (pure LTB and Ag:LTB) were measured in the correct location.

The alignment of the sample can also be corrected in the software, if the amount of sample misalignment is known. The correction factor is simply hardcoded in so that the spectrum is centered.

4.5 Vacuum Pumpdown

Due largely to the small 0.5 cm gap between the source and the sample, in which stray annihilations with air could occur which would contaminate the signal, the air was evacuated from the chamber. Air throughout the entirety of the chamber would reduce the efficiency of the system overall.

During pump down of the vacuum chamber after inserting a new sample, great care was taken in making sure new copper gaskets are used and that the bolts securing the conflat flanges in place were tightened as much and as evenly as possible so that leaks in the system are minimized. During pump-downs, the motor would have to be run for a while and then restarted several times in order to evacuate the large quantity of air from the relatively large chamber before lower pressures necessary for pump operation could be achieved. Having numerous lead bricks inside the chamber leads to possible outgassing and spread of particulate inside the chamber, which the pump must deal with. The largest concern when pumping down over several pump cycles was ensuring that the bearing in the pump motor did not increase in temperature higher than 48-50 degrees Celsius, as this would cause damage to the bearing. The motor temperature itself was of less concern than the bearing temperature. Since the target chamber was inherently leaky and not as clean as it could be inside, this would cause the pump to overwork itself trying to pump down, which would require it to be restarted. If the bearing temperature

increased too much, the pump would be left alone for several minutes to allow the bearing to cool down before attempting to pump down again. After an iterative process of tightening the nuts on the flanges, attempting to pump down, and repeating, the maximum number of cycles per second that the pump motor could reach would continually increase until it was able to reach the necessary 1500 Hz. From this point the bearing temperature was monitored to ensure it was not gradually increasing, but instead was gradually decreasing. Then the motor could be left unattended. Typically after a sample exchange, this pump down process was an additional 3-4 hours. The pressure was typically in the range of 10^{-3} Torr right after achieving a stable pump down, and after 12 hours was in the range of 10^{-5} Torr. As long as the pump was left on throughout data collection, this pressure could be maintained indefinitely.

4.6 Data Collection

4.6.1 Digital Data Acquisition

The PhDs Co. DSSDs and accompanying Spect72 and Imager processing software operate on the principle of taking individual analog pulse signals from the strips themselves and converting them into digital data which can then be stored, displayed, and analyzed as desired. The waveforms coming from the strips of the DSSDs are digitized according to user-defined settings in Imager. The software is used to program the FPGAs and record information from the individual channels based on the time integral of the detector pulses.

The Spect72 data acquisition unit is connected to a laptop via USB which contains Imager software that is specifically designed to control the data acquisition

process with this setup. This software records and optionally parses the data collected from the Spect72. The Spect72 system can capture data as events or as waveforms, providing the user with several options. The user can request the collection of all data events, all events within an energy range, or all events coincident with collection from multiple strips. There are three ways to save data from a data run: first, as energy-filtered data files; second, as raw event files; and third, as raw data files. For the purposes of this experiment, only the raw event files were of use. The energy-filtered data was not sufficient enough nor was it filtered in the manner necessary for combined ACAR and DBAR, and the raw data files were too large and encompassing to be of any use—they were too general and not specific enough by event. The raw event file gave information most useful, where it reports energy-specific charging events resulting from radiation and their associated location and timing. The specific format of the raw event file is clearly explained in [18].

Data files can become very large, into the hundreds of megabytes and even gigabytes, requiring the user to parse the data down to only the most important information. In the data parsing system devised by Capt. Stephen Jimenez, first only events from the raw event file which were coincident on either 2 or 4 strips simultaneously are extracted using a stream editor command in a UNIX bash shell. The reduced file is then parsed further and analyzed using Matlab.

4.6.2 Data File Parsing

After data has been acquired with the system, the next action is to use a bash script (listed in Appendix B) which reduces the raw event files to only events which occur in either two strips at once for the purposes of efficiency calculations or four strips

at once for ACAR and DBAR calculations. This process quickly eliminates useless excess data. Events which occur in two strips are useful for yielding a position of interaction with both an AC and a DC strip for a full-energy event in one detector. This is sufficient to provide information about detector efficiency, but does not contain anything about events coincident in both detectors. Events which occur in four strips are the only events known to be coincident for certain assuming the charge deposition occurred in one AC and one DC strip in each detector exactly. For the samples measured in this work, a 24-hr dataset (around 3.6-3.8 GB) typically took about 5 to 10 minutes to run through the bash script.

After selecting events only in 2 or 4 strips depending on the desired information, the resulting file is run through a Matlab parsing code (Appendix B) which parses the coincident events by energy by using a window around the annihilation photon energy of 511 keV. For this work the window used was 511 ± 12 keV, which was more than enough to capture all useful events. All of the energy peaks analyzed were actually constrained within 511 ± 8 keV, but a bit more was added to the window as a buffer. For the samples measured in this work, a 24-hr dataset (around 3.6-3.8 GB) typically took about 2.5 to 3 hours to run through this Matlab parser. The large file sizes required the system RAM to be used at its maximum capacity; the computer resorted to memory swapping during this process, where it would continually switch back and forth between using the system RAM and space on the hard disk. The resulting file is then run through either the efficiency/resolution calculator if one is characterizing the detector or through a series of codes which provide ACAR/DBAR information and apply a subpixel efficiency correction. The code used for the alternative ACAR analysis written by Maj. Angelo

Bonavita parses and processes data in a similar manner, but is able to run through a dataset significantly faster (24 hrs of data processed in around 10 minutes).

4.6.3 Subpixel Interpolation

The Imager software does present a 2D colormap of radiation interactions across the detector face (rotated at 90 degrees counterclockwise from reality due to what is most likely a programming error) on the main screen according to what appears to use a 7 x 7 subpixel array in each pixel for presenting the data. However, this does not suffice. The parsing code mentioned above reads the data in and determines which subpixel each event occurred in based on a user-defined number of substrips per strip for it to use. The way in which the data acquisition software assigns locations to charge events makes use of a proprietary figure of merit (FOM), which is proportional to the area of the HPGe strip on which charge deposition occurred. Equation 3 below shows how the subpixel position number is calculated using the FOMs of the strips adjacent to the strip in question.

$$N_{sp} = N_{substrip} \left[N_{chan} + \frac{FOM_{succ}}{FOM_{succ} + FOM_{pred}} \right] \quad (3)$$

Where:

- N_{sp} = Subpixel position number
- $N_{substrip}$ = Number of substrips per pixel
- N_{chan} = Channel/strip number
- FOM_{pred} = Figure of Merit for predecessor strip
- FOM_{succ} = Figure of Merit for successor strip

The successor strip is defined as the strip adjacent to and higher in number than the strip in question. The predecessor strip is defined as the strip adjacent to and lower in number than the strip in question. The strips run from 0-15 for the DC side and 16-31 for the AC side. Table 1 below shows the channel numbers (Spect72) and subpixel designations (DSSDs) assigned for the setup used in this research. All data collected was parsed using a 5 x 5 subpixel array in each pixel, which was shown in [3] to be the best array to use for maximum subpixel resolution without losing information.

Table 1: Channel number and subpixel designations

Detector	Side	Channels	Subpixels
1	DC	0-15	1-80
1	AC	16-31	81-160
0	DC	32-47	161-240
0	AC	48-63	241-320

Using 5 substrips per strip means that across all 16 strips on the detector face, there are a total of 80 substrips per detector side.

4.6.4 Subpixel Efficiency / Resolution Calculation

The subpixel efficiency was calculated in the Matlab efficiency correction by making use of a simple solid angle concept, assuming that radiation was directly incident upon each pixel at an angle normal to the surface, in order to calculate the intrinsic efficiency of each pixel and therefore subpixels. Equation 4 shows this solid angle calculation:

$$\Omega = \frac{w^2}{4\pi d^2} \quad (4)$$

Where:

- w = Width of a pixel (4.75 mm)
- d = Distance from sample to detector face
- Ω = Solid angle subtended by a pixel

This equation is exactly correct for a pixel on the centerline from the sample to the detector face, and is a reasonable approximation for the other pixels on the face. However, to get a more exact calculation, one must use Equation 5 to calculate the solid angle subtended by pixels off the centerline, which is how the Mathematica efficiency calculation (written by Maj. Angelo Bonavita) works:

$$\Omega_{offCL} = \Omega_{CL} \frac{d}{\sqrt{d^2 + (g + w)^2 ((n - 8) - 0.5)^2 + ((m - 8) - 0.5)^2}} \quad (5)$$

Where:

- Ω_{offCL} = Solid angle subtended by a pixel off the centerline
- Ω_{CL} = Solid angle subtended by a pixel on the centerline
- d = Distance from sample to detector face (2.0 m)
- g = Gap in between pixels (0.25 mm)
- w = Width of a pixel (4.75 mm)
- n = AC strip number of the pixel

$m =$ DC strip number of the pixel

This equation takes into account the fact that with a 16 x 16 matrix, the centerline falls in between pixels 8 and 9 in either direction.

The subpixel resolution calculation was performed simply by binning a particular full-energy peak, and searching for the energy values on either side of the peak energy value which fall close to the half value of the peak maximum number of counts. In this way, the FWHM for energy events in each subpixel was calculated.

V. Data Analysis and Results

5.1 2D ACAR and CDBAR Calculation

After the raw event files for each data run for each sample are filtered by energy and coincidence and they are subpixel-interpolated, the resulting Matlab matrix file (.mat) may be used to perform the 2D ACAR and CDBAR calculation. A raw data version is also created, which is not subpixel-interpolated. This can be used to gain a general understanding of the dataset but will not provide adequate information for ACAR and DBAR calculations. Appendix C contains the Matlab code named ThreeDPASSCalc3 which performs the calculation and applies the subpixel efficiency correction. The basic functionality of the code is as follows: first, the 4-strip event subpixel data from the parsing code is loaded; second, the events found in the outer pixels (outer two strips) of either detector are removed; third, relative efficiencies (based on one of the three efficiency correction methods) are assigned to each event based on subpixel location; fourth, the deviation from colinearity in vertical and beam axes is calculated; fifth, the energies of the events in both detectors are binned and correlated; and lastly, the raw and relative-efficiency-corrected histograms for 2D-ACAR and CDBAR are calculated and plotted. Actual counts are divided by relative efficiency values based on their location within the pixel and possibly, depending on the type of correction used, within the detector, in order to compensate for low efficiency subpixels on the edges of pixels.

This code, originally written by Capt. Stephen Jimenez, required extensive debugging because Detector 1 was rotated by 180 degrees around the vertical axis for this research. The code was originally written with the AC side of Detector 0 and the DC side of Detector 1 facing inwards, but since the AC sides of the DSSDs seem to have better

efficiency than the DC sides, Detector 1 was rotated such that its AC side faced inwards and DC side outwards. This, along with the fact that some of the cables connecting the various channels to the Spect72 were swapped around, led to the debugging necessity. The ACAR calculation makes use of the small angle approximation when calculating the angular deviation. An alternative plotting approach for ACAR, developed by Maj. Angelo Bonavita in Mathematica, was also applied.

5.2 Results for Virgin Lithium Tetraborate

The virgin, undoped, single-crystal LTB sample tested in this work was a relatively large piece cut from a larger circular crystal manufactured by New Light which was cut along the (001) plane. The sample had been cut from a larger, originally circular crystal and measured roughly 1.7 cm along one side, 0.8 cm along the other, and 1 mm thick. It was roughly rectangular but with uneven edges and corners. These dimensions, if a true square, would give about 1.36 cm² of surface area. This was by far the largest crystal measured in this work and yielded the highest coincident count rates over long time periods.

The total dataset acquired for this sample yielded 17,380 events, after filtering for energy and coincidence, over a total period of 276 hours, or 11.5 days. This equated to an average of 1511.3 coincident events per 24-hr time period. The majority of data runs contributing to the dataset were taken over either 30-hr or 24-hr periods and afterwards all runs were summed together to gain the full dataset. Figure 28 below shows the coincident response of the two detectors for the entire virgin LTB dataset. In Figure 29 the ACAR calculation results for pure LTB are shown. These graphs show the deviation

from colinearity in the plane transverse to gamma emission. The left picture shows combined 2D plot while right picture shows each dimension individually. Important to note here is how the highest intensity in the ACAR occurs in the center, where there is no

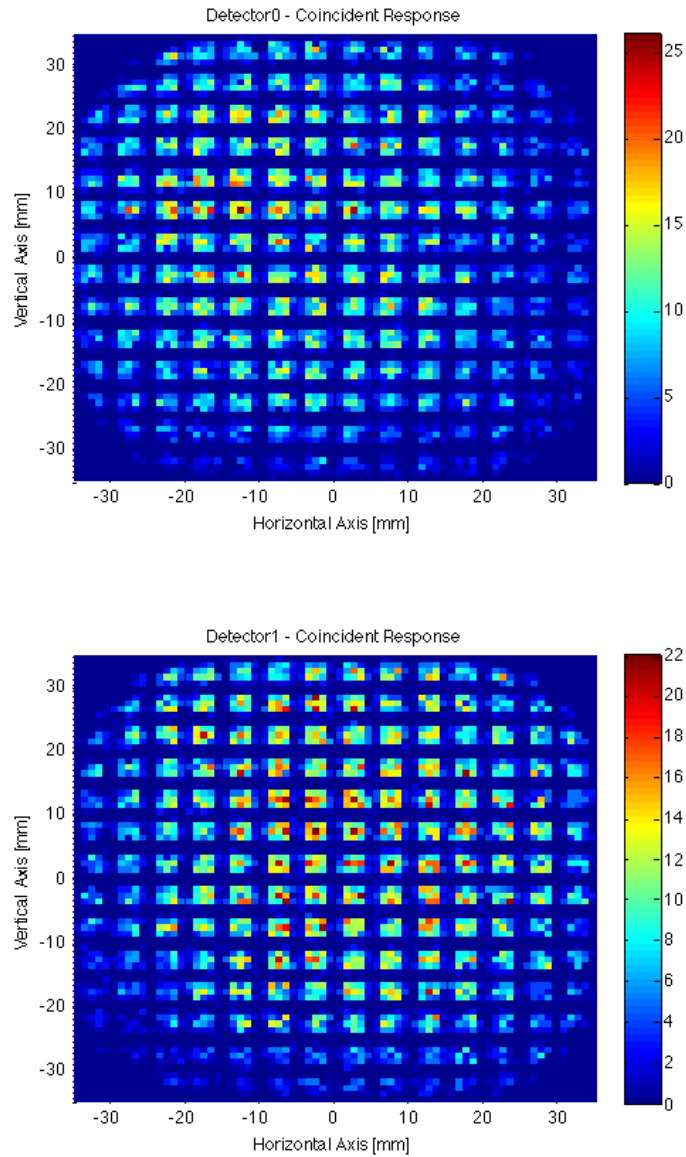


Figure 28: Coincident response across both detector faces for the pure LTB dataset.

angular deviation, and the graph drops off from there as it moves outward. For the pure LTB, the greatest extent of the higher-deviation gammas is around ± 11 mrad, and it is cut off somewhat outside of that circle. The highest concentration of events occurs towards the center, with fewer events occurring with larger angular deviations. It should be noted that the ACAR spectrum here has been corrected in software for a slight misalignment by moving its center 2 mrad in the positive X direction and 8 mrad in the negative Y direction. Even though the pure LTB was measured after a better alignment was accomplished following measurement of the Cu:LTB (which was significantly off-center), the pure LTB and Ag:LTB samples were still somewhat off center.

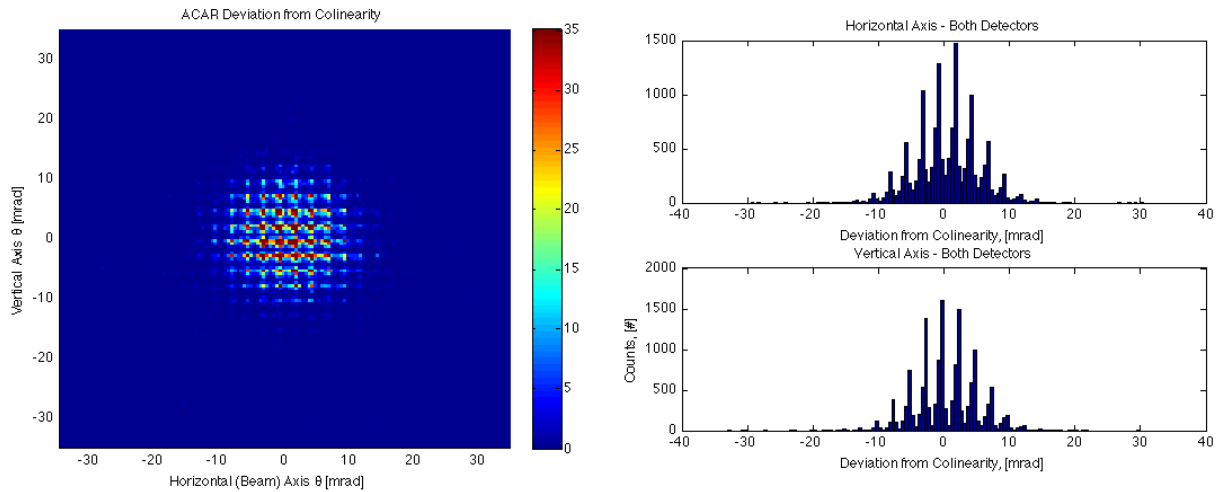


Figure 29: ACAR calculation for the pure LTB dataset showing deviation from colinearity in the plane transverse to gamma emission. Left picture shows combined 2D plot while right picture shows each dimension individually.

Figure 30 below includes additional information about the ACAR calculation: the left picture shows ACAR data with the pixel-normalized subpixel efficiency correction applied and the right one shows data that is pixel-filtered using a mask after applying the

pixel-normalized efficiency correction. Figure 31 demonstrates the application of two additional efficiency correction methods to the same ACAR dataset for the pure LTB, with the left picture showing the result of the detector-normalized, average relative subpixel correction, and the right picture showing the result of the Williams average relative subpixel correction. Clearly, the efficiency correction methods do not seem to add much useful information in the way the raw data is presented. A different way of analyzing the ACAR data before applying the efficiency correction must be accomplished in order to decipher potential identifying features. There seems to be a common diamond shape present in all of the raw and corrected ACAR plots, however, and further analysis may refine this shape. One more thing to note is that because of the flipping of one of the detectors, the code seems to be generating an artifact where the axes are flipped only after the efficiency correction is applied.

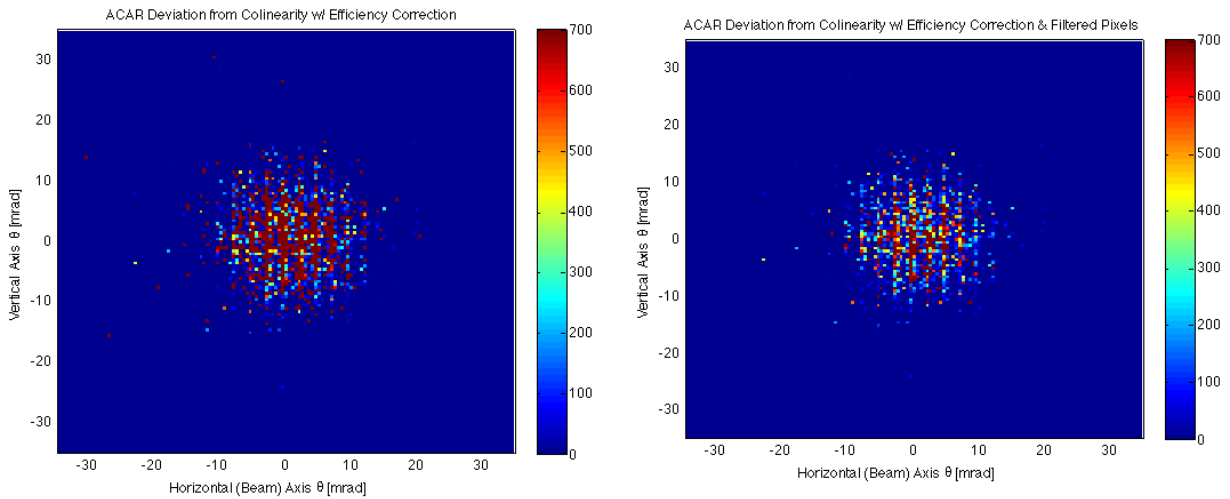


Figure 30: ACAR calculation for the pure LTB dataset; left picture shows data with the pixel-normalized efficiency correction and right picture shows the same pixel-normalized efficiency-corrected data, only pixel-filtered.

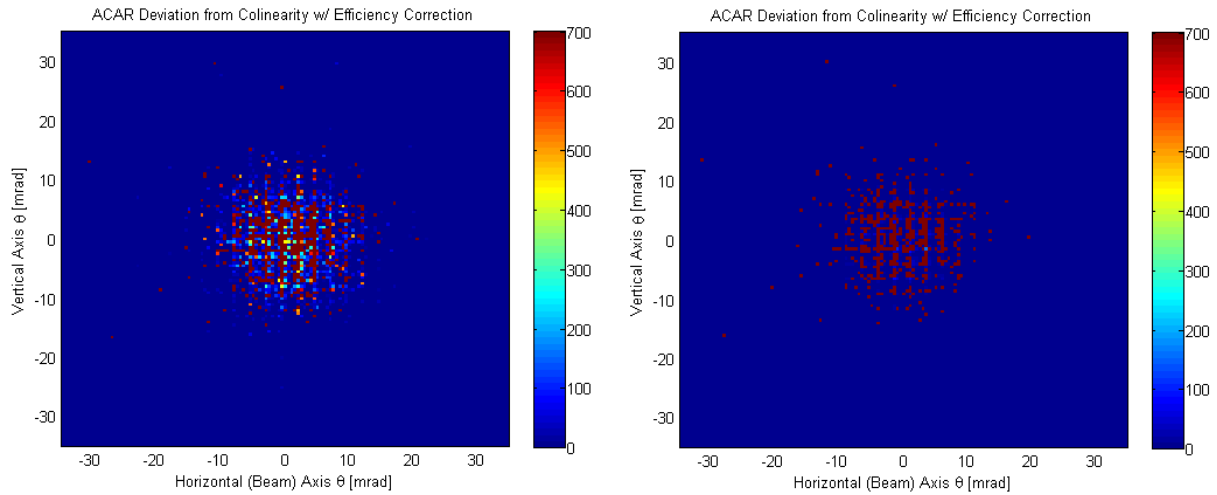


Figure 31: ACAR calculation for the pure LTB dataset; left picture shows data with the detector-normalized (average) efficiency correction and right picture shows with the Williams efficiency correction.

Next, raw ACAR results are presented utilizing an alternative plotting routine established by Maj. Angelo Bonavita in Mathematica, which processes the data in a manner very similar to the Matlab files listed in Appendices B and C, according to the method of Lt. Col. Christopher Williams [3]. This ACAR plot is generated using a 1.5 mrad binning resolution. The main difference here is that the results are plotted using a histogram contour plot, which makes the data appear to be smoother as opposed to the plots heretofore, which have been discrete, segmented histograms. Figure 32 below shows the ACAR spectrum for the pure LTB sample.

The LTB ACAR spectrum is interesting, but difficult to analyze. There are definitely some indications of momenta features. However there are not sufficient counts to cause these features to stand out. Using symmetry as a guide for LTB, the approximate momenta peaks appear to be (in units of $10^{-3} m_0c$): (0,0) (-12,0), (+12,0),

(0,-12); (-10,-12), (-10,+12); (-18,+5), (-5,+18); (-18,-18), (+18,+18). These are potential electron momenta features in the plane perpendicular to gamma emission.

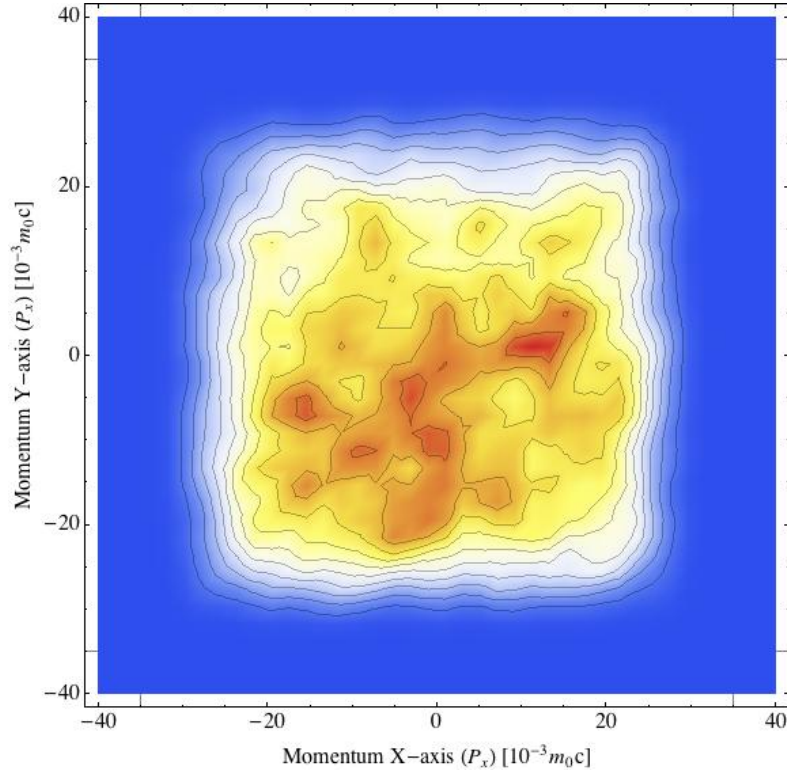


Figure 32: Raw ACAR spectrum for the pure LTB dataset plotted as a histogram contour plot using a 1.5 mrad binning resolution in electron momentum units of $10^{-3} m_0 c$. Red indicates higher counts and yellow lower counts, with blue being zero.

Figure 33, which follows, demonstrates raw results for counts versus distance from the DSSD crystal center from both detectors for the pure LTB sample. Here the left image shows the horizontal axis and the right image shows the vertical axis. Results for counts versus distance from the DSSD crystal center from both detectors for pure LTB with the pixel-normalized efficiency correction applied are shown in Figure 34. The left image shows the horizontal axis and the right image the vertical axis. This figure clearly

shows the large relative error introduced by correcting by means of individual subpixel as opposed to average values.

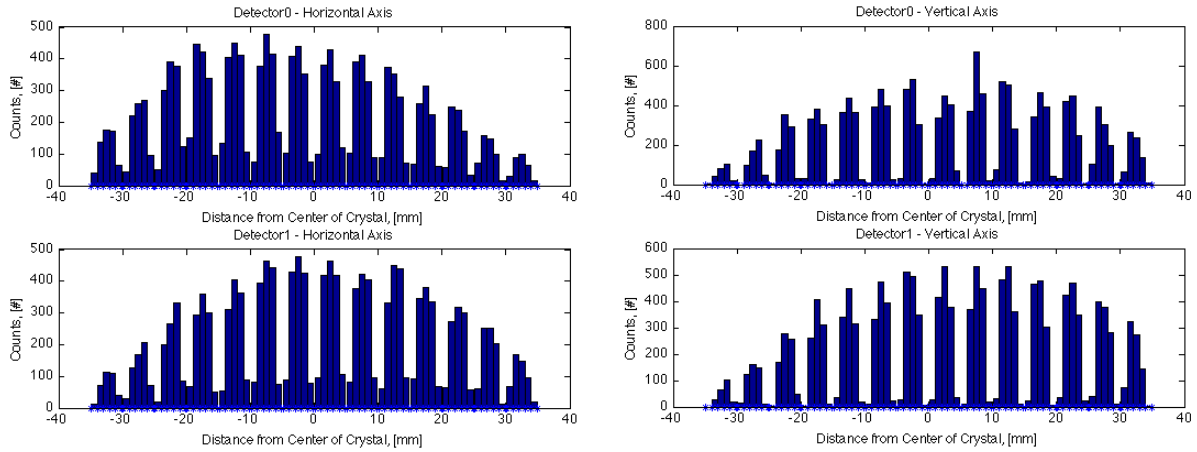


Figure 33: Raw results for counts versus distance from the DSSD crystal center from both detectors for pure LTB. Left image shows horizontal axis and right image shows vertical axis.

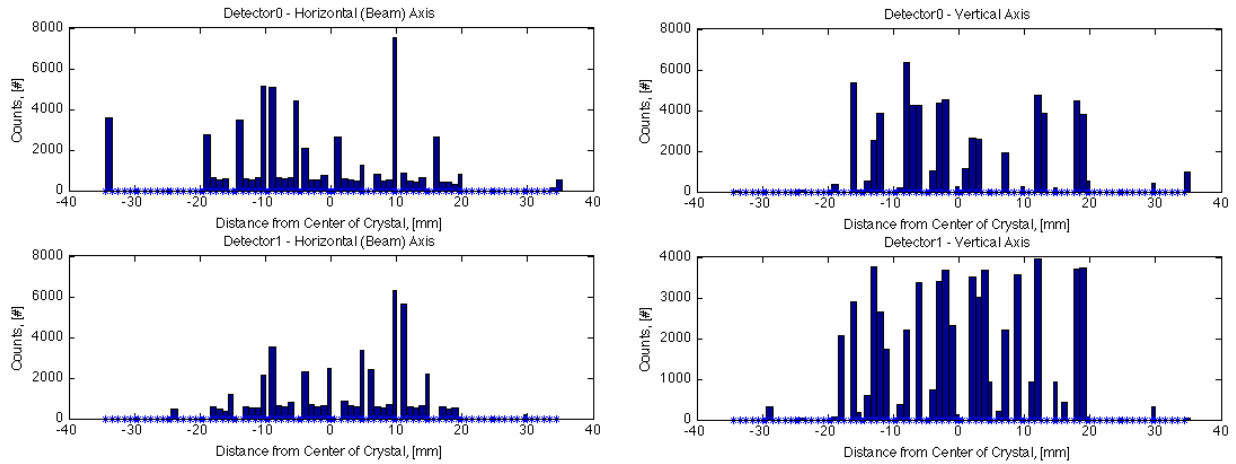


Figure 34: Results for counts versus distance from the DSSD crystal center from both detectors for pure LTB with the pixel-normalized efficiency correction applied. Left image shows horizontal axis and right image shows vertical axis.

Figure 35, which follows below, shows the results of applying the detector-normalized average relative subpixel efficiency correction to the counts detected versus the distance from the center of the crystal. This correction is less noisy than the previous one. One thing to note is that in the horizontal axis the subpixels closest to the gaps are boosted, but in the vertical axis they are not. Afterwards, Figure 36 shows the result of applying the Williams efficiency correction to the data. This appears to boost more uniformly, as expected.

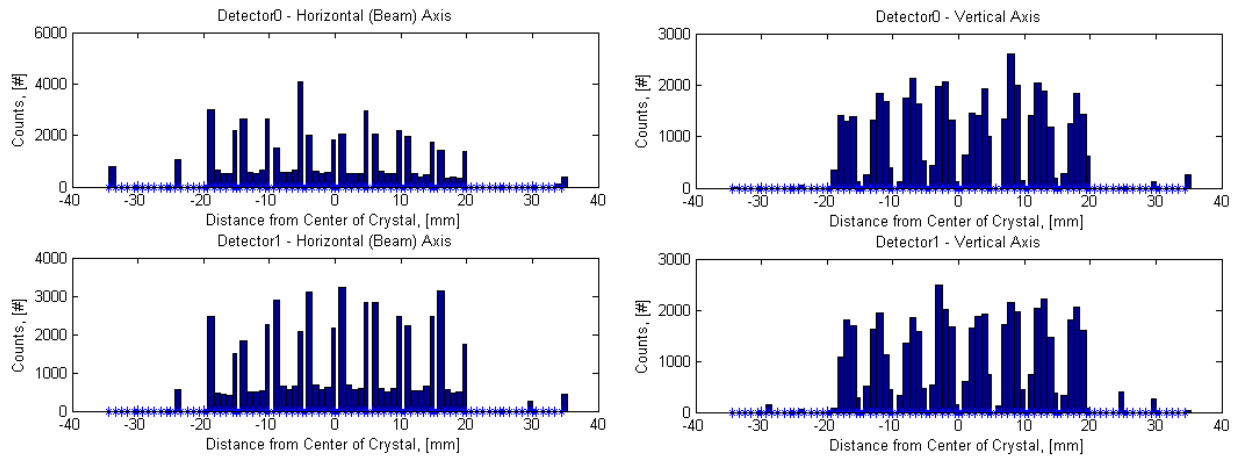


Figure 35: Results for counts versus distance from the DSSD crystal center from both detectors for pure LTB with the detector-normalized efficiency correction applied. Left image shows horizontal axis and right image shows vertical axis.

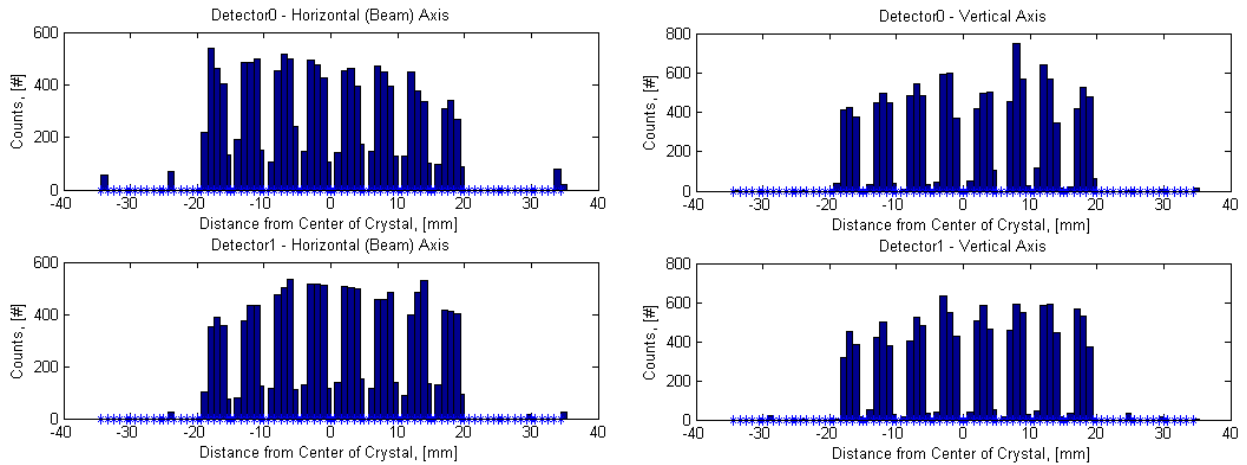


Figure 36: Results for counts versus distance from the DSSD crystal center from both detectors for pure LTB with the Williams efficiency correction applied. Left image shows horizontal axis and right image shows vertical axis.

The raw DBAR results for pure LTB are seen in Figure 37, with the left image showing the energies of events in the two detectors graphed against each other and the right image showing the energy data from each detector individually. Following these images, Figure 38 shows ways in which the efficiency correction was applied. The picture on the left shows the result of applying the pixel-normalized (individual subpixel) efficiency correction to the raw DBAR data. The picture on the right shows the result after a mask is applied to filter some of the pixels from the data corrected with the pixel-normalized matrices. These DBAR plots do not immediately show additional information, although they may be able to be used in further analysis for more accurate selection of the swath width. Results for the detector-normalized and Williams corrections are not shown.

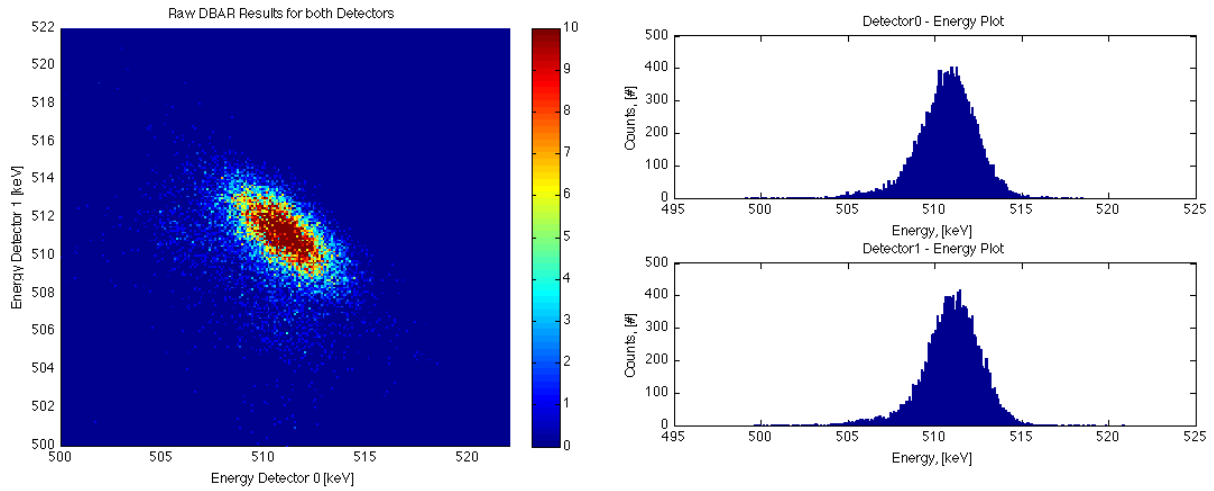


Figure 37: DBAR calculation for the pure LTB sample. Left image shows the energies of events in the two detectors graphed against each other; right image shows the energy data from each detector individually.

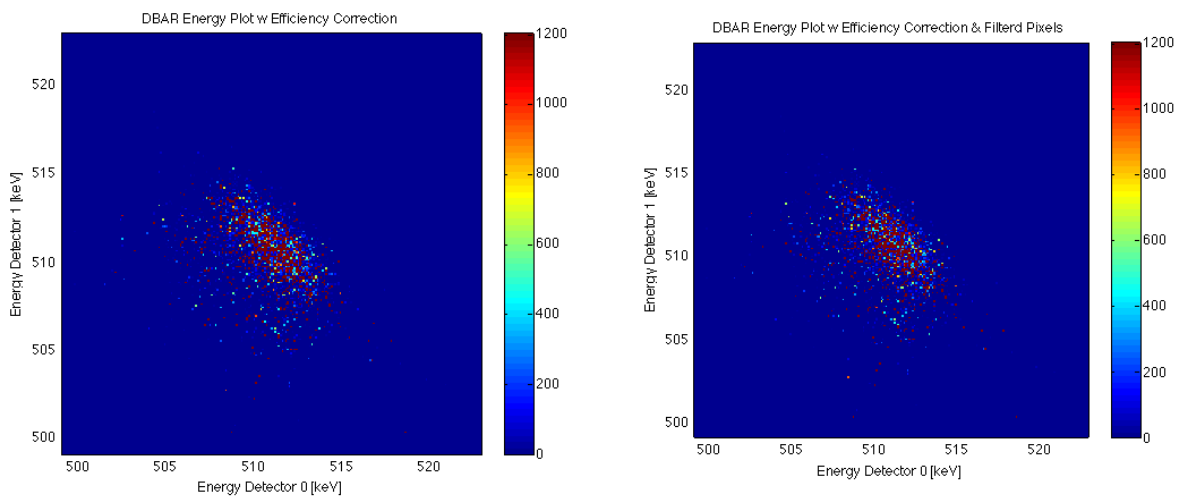


Figure 38: DBAR calculation for the pure LTB sample corrected for efficiency. Left image shows DBAR data with an efficiency correction applied; right image shows the data with an efficiency correction and a pixel filter applied.

Taking the DBAR results from both detectors, one can plot a coincidence Doppler - broadened lineshape across the 45-degree swath line which extends from the top left of the DBAR plot to the bottom right of the plot. Events within a certain swath width or window which lie on this line represent real information about the material in which

annihilation took place. Events below this swath line represent incomplete charging events and those above the line are indications of charge-pile up. Figure 39 shows plots of this 45-degree swath line for the pure LTB sample, known as a coincidence DBAR (CDBAR) graph. These plots are histograms of correlated energy events occurring where the total energy detected in both detectors is constant (equal to 1022 keV). The appearance of these graphs depends upon the binning energy resolution used and the width of the 45-degree swath used. In previous work [3], C.S. Williams showed that a binning resolution of 0.1 keV was typical for datasets with very large numbers of coincident events. In this work, larger binning resolutions (0.3-0.8 keV) were necessary to show good results because of lower count rates. Fairly large swath widths, defined using the quantity Δ , where Δ is one half-width of the full swath, were used in order to include enough relevant information across the diagonal without getting too much into the incomplete charge or charge pile-up regions. Plots here in Figure 39 are shown using a $\Delta = \pm 2$ keV half width in the left column and a $\Delta = \pm 4$ keV half width in the right column for energy binning resolutions of 0.4, 0.5, and 0.6 keV. The black line is the original data and blue is the data plotted with the pixel-normalized subpixel efficiency correction, which is rather noisy. There seems to be an artistic component of choosing the binning resolution and the swath width to best display data from the DBAR calculation. If the binning resolution is too small, there is a lot of noise. Too large, and there is no useful information. If the delta chosen is too small, not enough vital information is included. If it is too large, too much useless noise is included. For further analysis, perhaps a line tracing routine could be used to more accurately select the desired events along the swath.

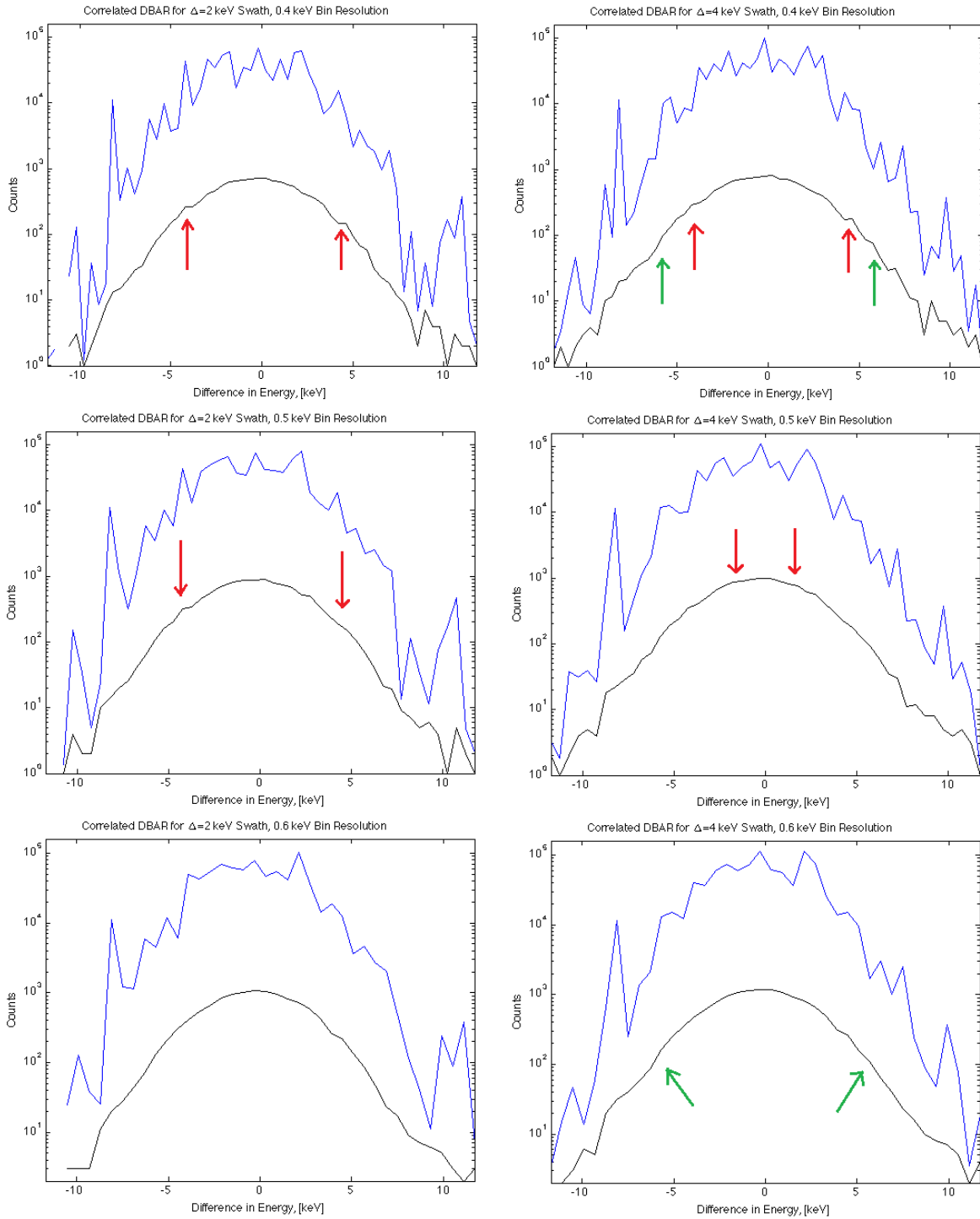


Figure 39: Coincidence DBAR (CDBAR) results for undoped LTB with swath width $\Delta = \pm 2$ keV on left & ± 4 keV on right for 0.4, 0.5, & 0.6 keV energy binning resolutions. Black is raw data; blue is adjusted for the pixel-normalized efficiency correction.

The plots in Figure 39 above show likely symmetrical momentum features, as denoted by colored arrows, at ± 2 keV, ± 4 keV, and ± 6 keV; There is a slight possibility of a feature at ± 8 or 9 keV. Figure 40 below shows the plots for $\Delta = \pm 2$ keV and ± 4 keV swath half-widths at 0.4 keV binning resolution again, chosen for their clarity, only now plotted with the detector-normalized average subpixel efficiency correction. This method of correcting for efficiency does clearly smooth out the blue data curves by reducing noise and showing the presence of (potentially confirming) some noticeable symmetrical features, as denoted by colored arrows.

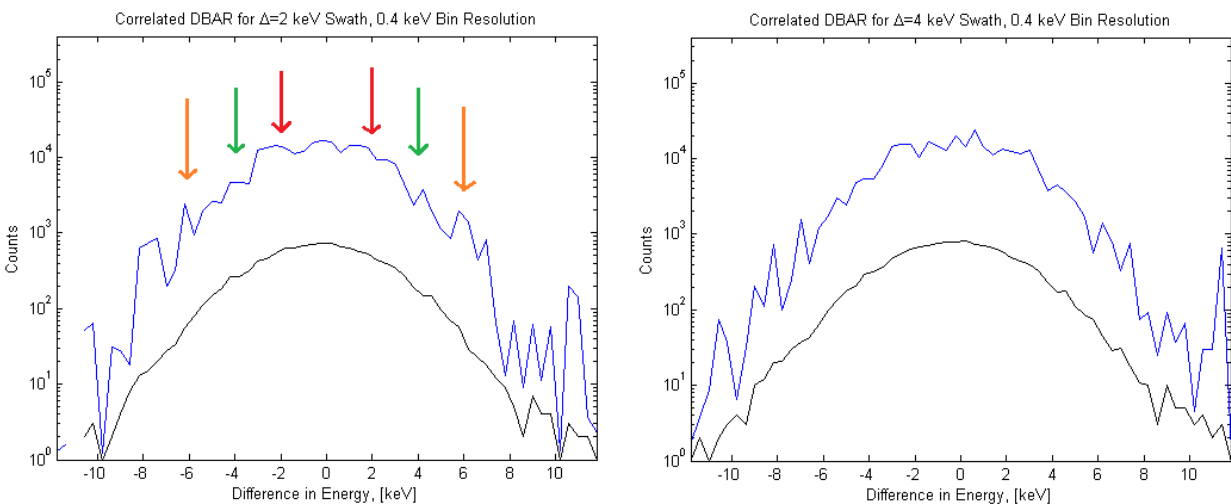


Figure 40: Coincidence DBAR (CDBAR) results for undoped LTB with swath width $\Delta = \pm 2$ keV on left & ± 4 keV on right for 0.4 keV energy binning resolutions; black is raw data and blue is adjusted using the detector-normalized efficiency correction.

Continuing with the pure LTB CDBAR data, Figure 41 again shows the raw data plotted using the same parameters as in Figure 40, except now the efficiency correction plot uses the Williams average relative subpixel efficiency matrix. Clearly, this method

causes the efficiency-corrected data to closely mirror the original data with only minor alterations present.

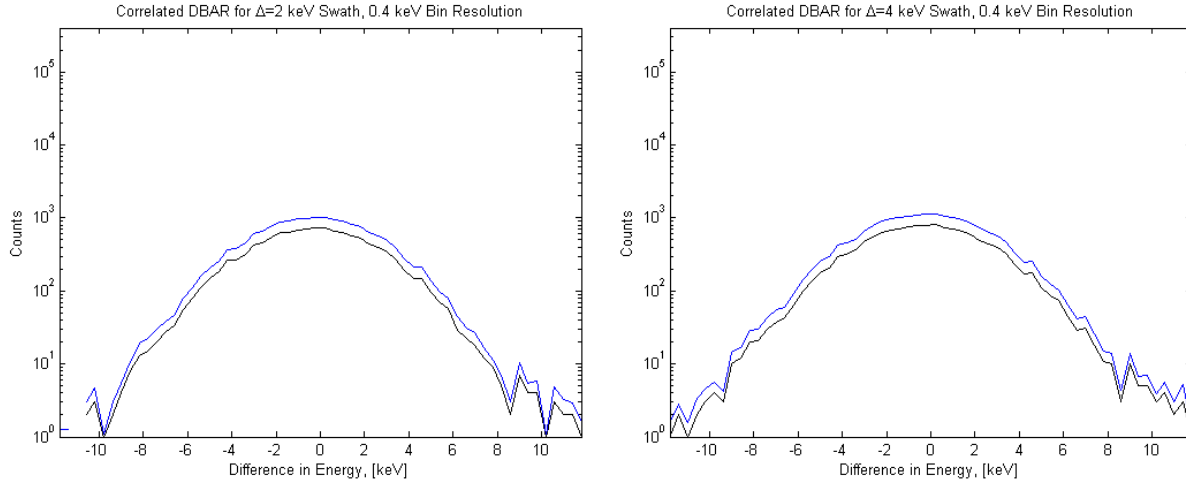


Figure 41: CDBAR results for undoped LTB with swath width $\Delta = \pm 2$ keV on left & ± 4 keV on right for 0.4 keV energy binning resolutions; black is raw data and blue is adjusted using the Williams efficiency correction.

5.3 Results for Copper-Doped Lithium Tetraborate

The copper-doped single-crystal LTB sample tested in this work was a half-moon shape with smooth edges. It was 1.3 cm long, 5 mm wide at its widest point in the center, and 1 mm thick. This would roughly be about 0.33 cm^2 in surface area, which is rather small. This small size led to low coincident counting rates. This crystal was doped with Cu at 0.015%, which is a very low doping amount.

The total dataset acquired for this sample yielded only 5,913 total coincident, full-energy events (after filtering for energy and coincidence) over a total period of 312.5 hours, or 13.021 days. This equated to an average of only 454.11 coincident events per 24-hr time period. The majority of data runs contributing to the dataset were taken over

roughly 24-hr periods and afterwards all runs were summed together to gain the full dataset.

This sample was the first crystal to be measured in this work. Because of time constraints, this sample was not able to be precisely centered in the vacuum chamber. The resulting ACAR plot was off-center by about 14 mrad along the horizontal axis (towards the beam), and by about -4 mrad along the vertical axis (down towards the table). Figure 42 shows the raw ACAR data for this sample to the left along with the same data after being corrected in software to the right. One notices immediately the presence of higher-momentum features which may be due to the presence of the higher-Z Cu in the LTB. Instead of being constrained to ± 11 mrad, there are coincident events occurring at ± 16 through ± 18 mrad. Since in this run the manipulator rod and sample mounting wire were not completely shielded as they were in the other two runs, there is a possibility that one of these, more likely the steel in the manipulator rod, could be contributing to these higher momentum features.

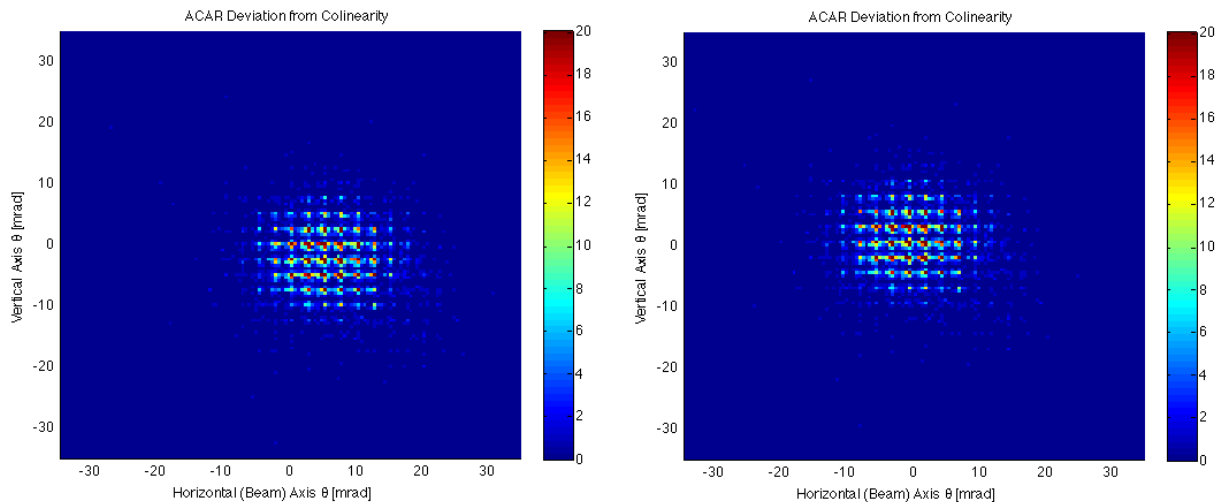


Figure 42: ACAR results for the Cu:LTB sample. Left picture shows actual data with misalignment of sample in the chamber. Right picture shows the same data after software alignment correction.

Figure 43 below demonstrates additional ACAR information for the Cu:LTB sample. The left graph is a plot of raw ACAR data according to each axis and the right graph is the ACAR data presented with the pixel-normalized efficiency correction applied. Additionally, in Figure 44 the ACAR data for the Cu:LTB dataset is presented with both the detector-normalized efficiency correction applied (left image) and the Williams efficiency correction applied (right image). The low count rate associated with this sample make the efficiency corrections less useful.

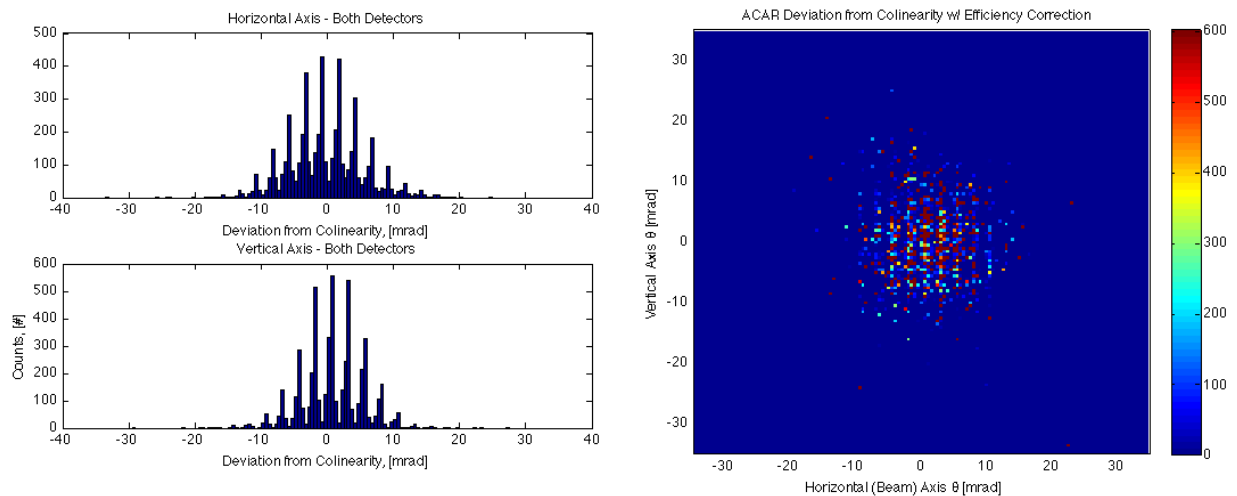


Figure 43: ACAR data for Cu:LTB: left image shows raw ACAR data presented by axis and right image shows 2D pixel-normalized efficiency-corrected ACAR data.

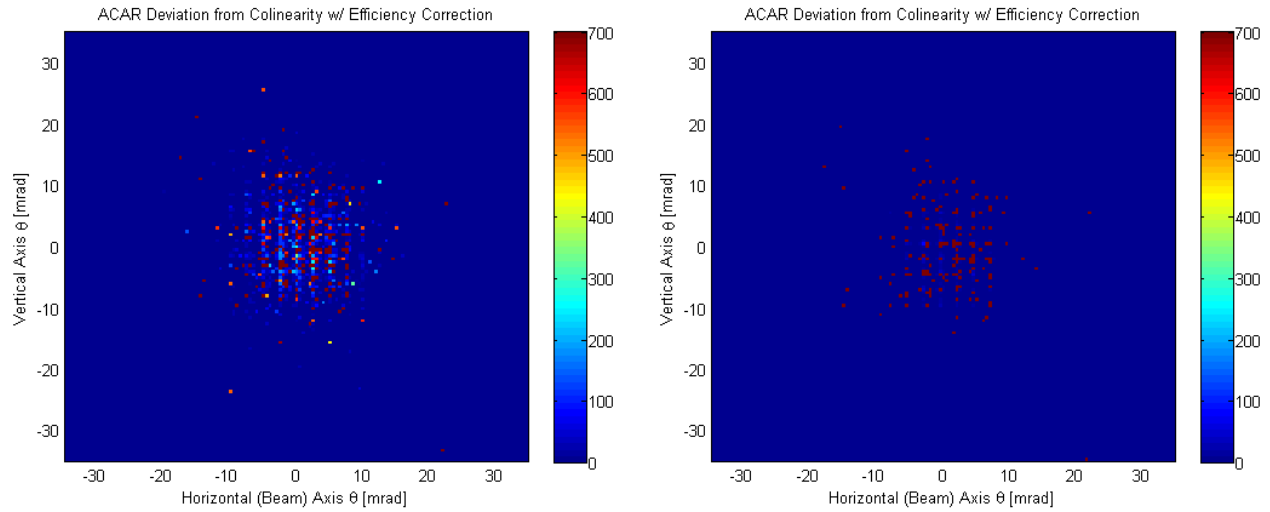


Figure 44: ACAR results for the Cu:LTB sample; left picture shows data with the detector-normalized efficiency correction and right picture shows with the Williams efficiency correction.

Again making use of the alternative plotting approach of Maj. Angelo Bonavita, Figure 45 below shows the raw ACAR spectrum for the copper-doped LTB sample. This plot presents the data using a histogram contour plot which appears to smooth the results and make features more noticeable. The Cu:LTB shows some differences from the pure sample. Again using symmetry as a guide, one notices several momenta features (in units of $10^{-3} m_0c$): a strong (0,0) feature as in LTB; (-12,0), (+12,0) as in LTB but also (-12,0), (+12,0). Some unique features are (-8,-8), (-8,+8), (+8,-8), (+8,+8). There is a hint of (-18,-18), (-18,+18), (+18,-18 doublet), and possibly a (+18,+18 doublet). Interestingly, the strongest features appear to occur in a circular pattern around the center. The features in the plot represent electron momenta in the plane perpendicular to gamma emission.

Following this, Figure 46 contains DBAR results for Cu:LTB, with the left image showing raw DBAR data from both detectors plotted against each other, and the right

image showing the data from each detector individually.

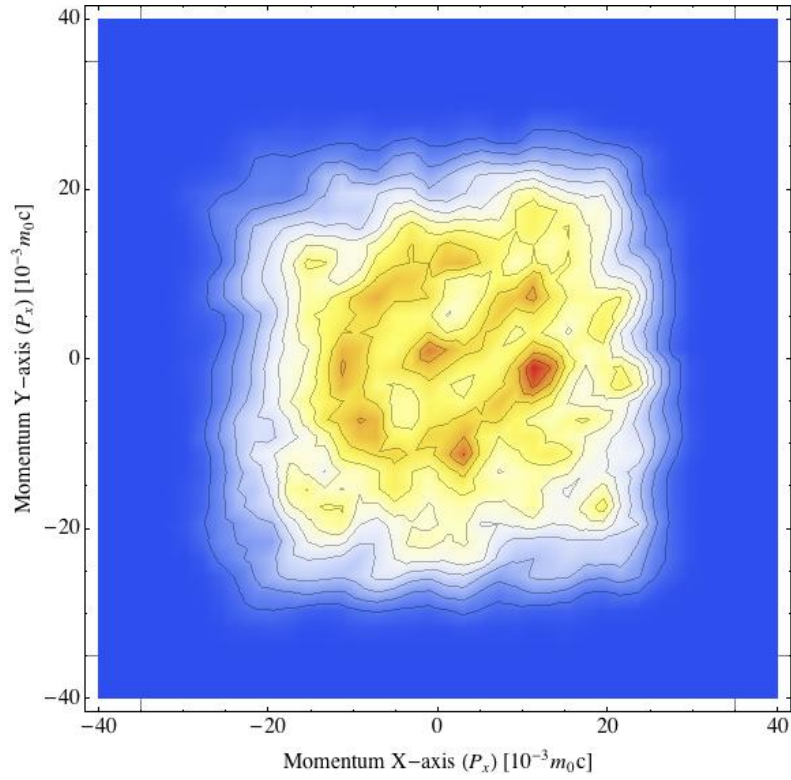


Figure 45: Raw ACAR spectrum for Cu:LTB, presented using a histogram contour routine with a 1.5 mrad binning resolution, in electron momentum units of $10^{-3} m_0 c$. Red indicates higher counts and yellow lower counts, with blue being zero.

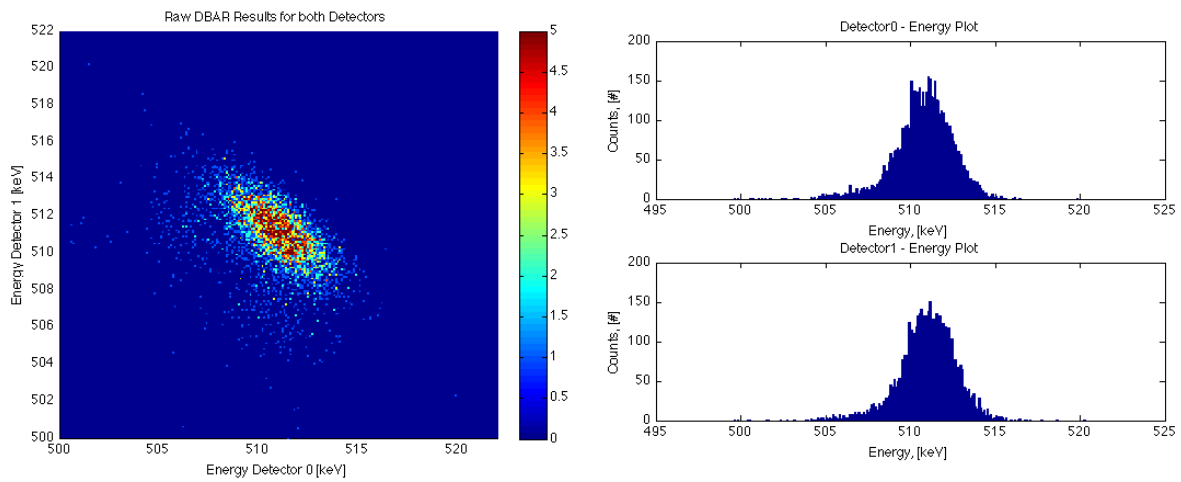


Figure 46: DBAR results for Cu:LTB. Left image shows raw DBAR data from both detectors plotted

against each other, while right image shows the data from each detector individually.

Figure 47, which follows, presents CDBAR data for the Cu:LTB crystal, showing graphs of the DBAR data along the 45-degree swath and associated efficiency correction. The data is plotted with a swath half-width of $\Delta = \pm 2$ keV in the left column and $\Delta = \pm 4$ keV in the right column for energy binning resolutions of 0.5, 0.6, and 0.85 keV. The graphs presented in Figure 48 once again show the CDBAR results for Cu:LTB, with only the plots for the 0.6 keV binning resolution for $\Delta = \pm 2$ keV and ± 4 keV swath half-width shown for clarity, but here the blue line represents the result after applying the detector-normalized average relative efficiency correction. This correction does reduce the noise somewhat, but because of the lower overall number of counts in this data set it does not smooth it as significantly as in the pure LTB dataset. Figure 49 shows the same plots as in the previous figure, except for showing results after applying the Williams efficiency matrix correction, which once again closely mirrors the raw data.

As pointed out with colored arrows in Figure 47, there are noticeable possible symmetrical electron momentum features located at ± 4 keV and ± 6 keV, along with a possible feature at ± 2 keV and an apparently symmetrical feature centered on 0 keV difference in energy (roughly ± 0.75 keV) which appears in a few of the graphs. These features are descriptive of recurring electron momentum values in the crystal structure of the Cu:LTB crystal.

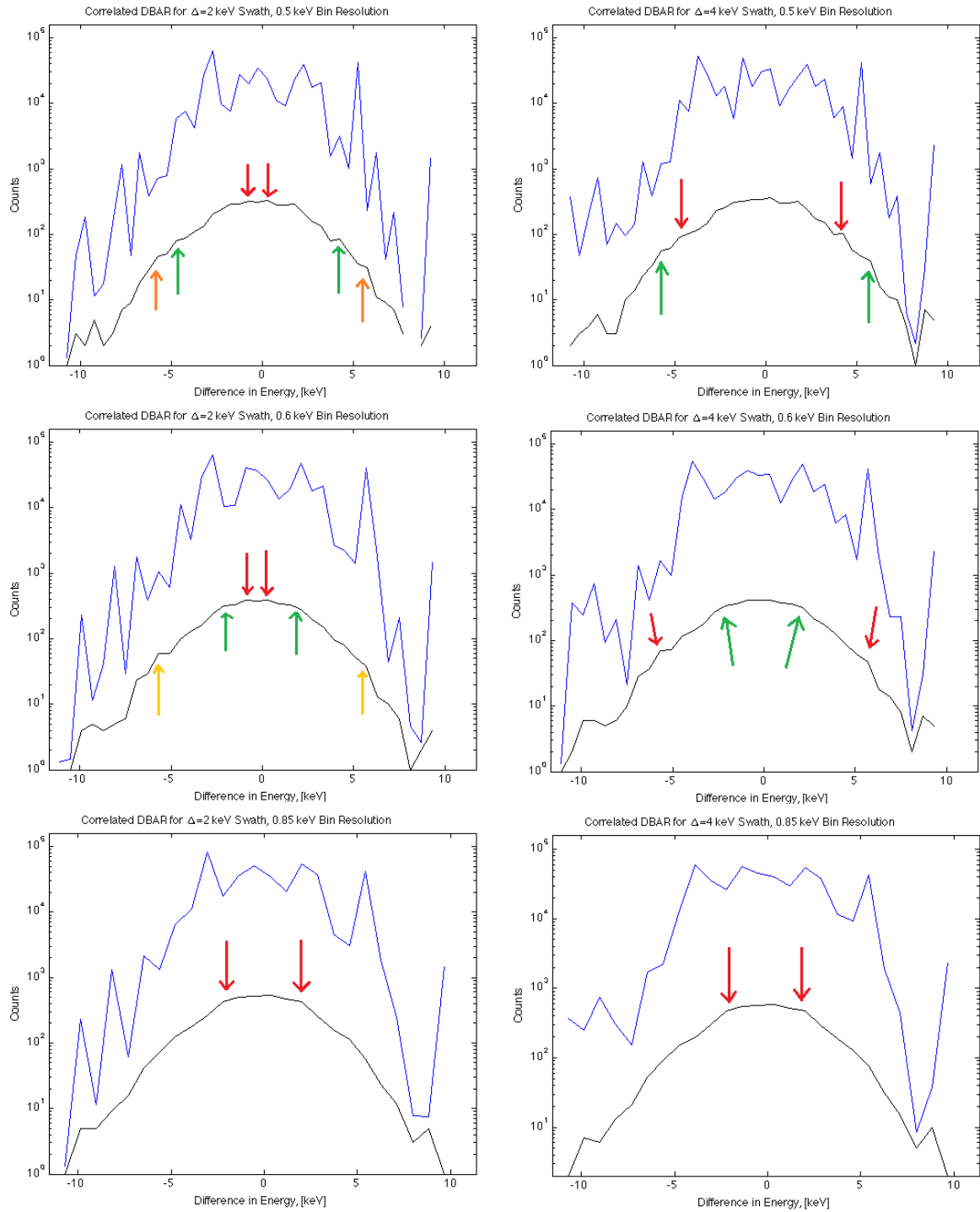


Figure 47: CDBAR results for Cu:LTB with swath half-width of $\Delta = \pm 2$ keV on left and ± 4 keV on right for 0.5, 0.6, and 0.85 keV binning resolutions. Black is raw data; blue is efficiency-corrected using the pixel-normalized efficiency correction.

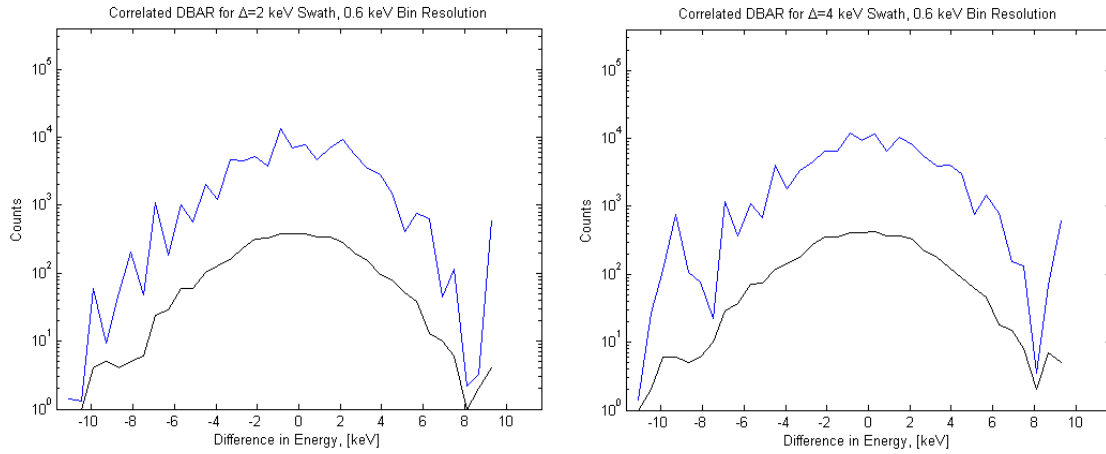


Figure 48: CDBAR results for Cu:LTB with swath half-width of $\Delta = \pm 2$ keV on left and ± 4 keV on right for 0.6 keV binning resolution. Black is raw data; blue is adjusted using the detector-normalized efficiency correction.

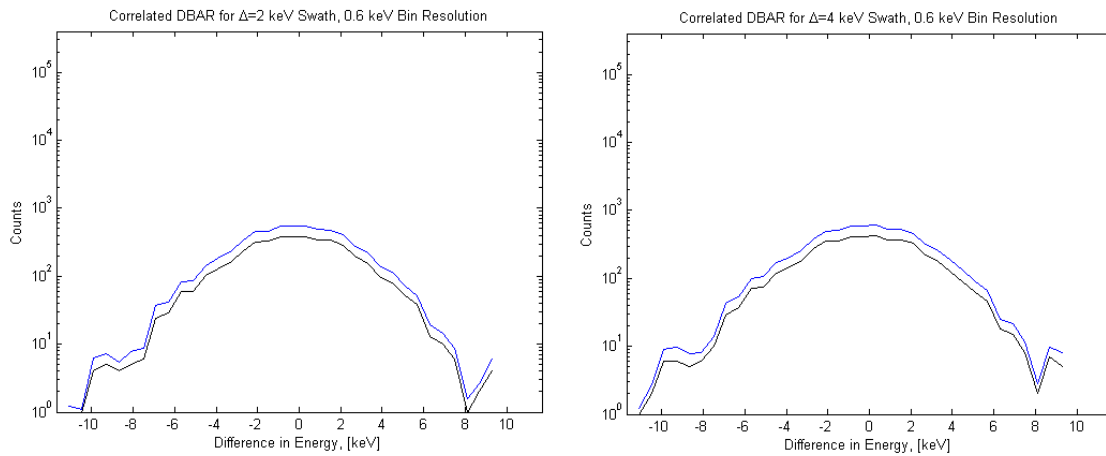


Figure 49: CDBAR results for Cu:LTB with swath half-width of $\Delta = \pm 2$ keV on left and ± 4 keV on right for 0.6 keV binning resolution. Black is raw data; blue is adjusted using the Williams efficiency correction.

5.4 Results for Irradiated Silver-Doped Lithium Tetraborate

The Ag:LTB crystal tested in this work was a square shape with very smooth edges. It measured 5 mm on each side, and was 1 mm thick. This would equate to 0.25 cm² in surface area, which was even smaller than the Cu:LTB sample tested. However, due to better alignment and positioning of the Ag:LTB sample and its square shape, the coincident count rate with this sample was higher than that of the Cu:LTB sample. Because of a previous long irradiation several months earlier and a more recent 10-minute X-ray irradiation using a Bremsstrahlung X-ray machine at AFIT, this crystal appeared green in hue, although still translucent. The irradiation causes the green coloration, which can be considered in and of itself a material defect. This results from the excitement of electrons in the atoms of the crystal and subsequent chemical changes within the crystal.

The total dataset acquired for this sample yielded 28,483 total coincident events (after filtering for energy and coincidence) over a total period of 659 hours, or 27.458 days. This equated to an average of roughly 1037.33 coincident events per 24-hr time period. The majority of data runs contributing to the dataset were taken over either 30-hr or 24-hr periods and afterwards all runs were summed together to gain the full dataset. Figure 50 shows the ACAR data for irradiated Ag:LTB, both raw and with the pixel-normalized efficiency correction applied. This ACAR data is corrected by 2 mrad in the positive X direction and 8 mrad in the negative Y direction, which was the same as for the pure LTB sample. It is important to note the presence once again of higher-momentum electron features (gamma deviations), which extend out to about ± 15 or 16 mrad at their largest. This did not appear to be the case in the pure sample. In addition,

the concentration of events is spread out more from the center, meaning that a slightly larger number resulted in higher angular deviations than in the pure sample, potentially indicating the presence of Ag. Figure 51 shows the Ag:LTB dataset corrected using the detector-normalized average subpixel method on left and the Williams average subpixel method on right. It appears as though the most useful efficiency correction method is the detector-normalized one, which makes use of the average relative values across each detector face and has less error than the pixel-normalized or subpixel-specific method. The Williams efficiency matrix seems to only remove some of the background in the spectrum, and this seems less accurate since the matrix was calculated using a different system setup.

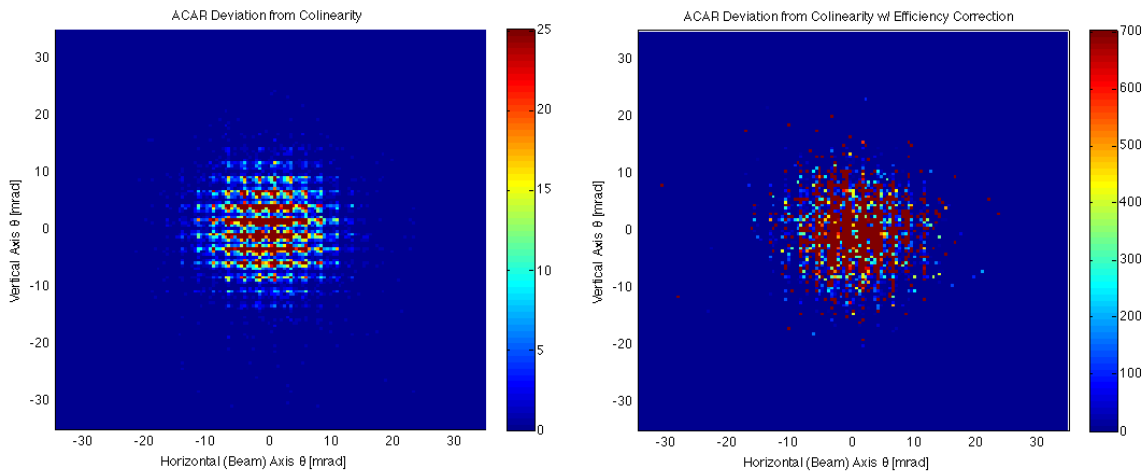


Figure 50: ACAR data for irradiated Ag:LTB. Left image shows raw data while right image shows the data with a subpixel relative efficiency correction.

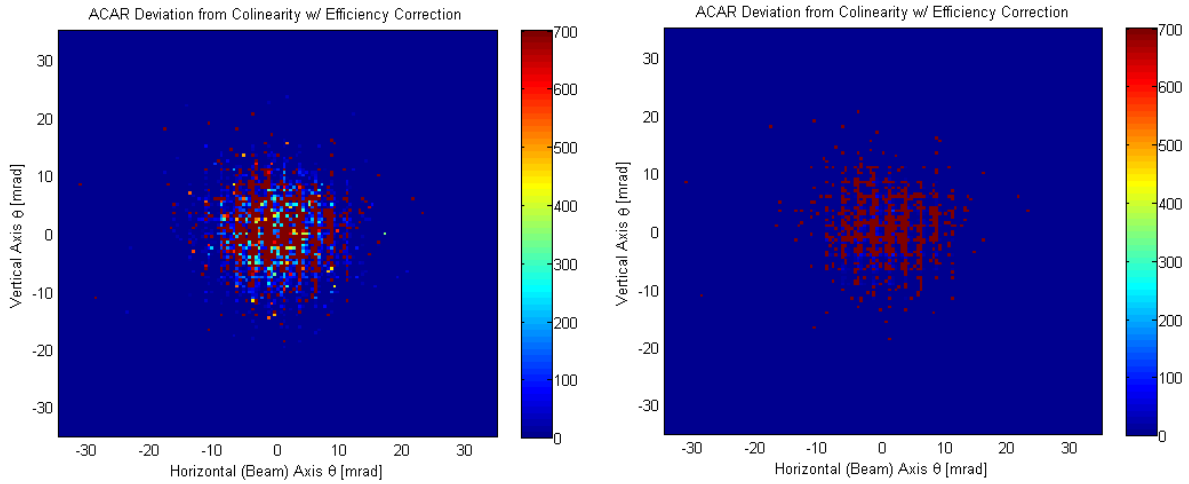


Figure 51: ACAR results for irradiated Ag:LTB; left picture shows data with the detector-normalized efficiency correction and right picture shows with the Williams efficiency correction.

The alternative plotting approach for ACAR with the silver-doped, irradiated sample yields Figure 52 below. Again, this plot presents the raw data using a histogram contour plot which appears to smooth the results and make features more noticeable. Making note of symmetrical electron momenta features (in units of $10^{-3} m_0c$) for Ag:LTB, which vary a bit from pure LTB, one finds: (-5,-5), (-5,+5); (-5,-18), (-5,+18), (+5,-18), (+5,+18); (+10,0), +10,0); (-18,-18), (-18,+18); There is less evidence of a (0,0) feature than in pure LTB (for Ag:LTB the (0,0) feature is very small), so it seems that, surprisingly, the Ag defects have less s-shell electron (low momenta) contributions. Additionally, the (5,18) momenta pattern seems to be altered. Otherwise, the Ag:LTB is only very little different from the pure sample. It does vary more so from the Cu:LTB sample. Again, these features represent electron momenta in the plane perpendicular to gamma emission.

Figure 53, which follows, portrays the DBAR information for the irradiated Ag:LTB sample. The image on the left shows a rather clean raw DBAR spectrum for both detectors together; the image on the right shows energy plots for each detector on its own.

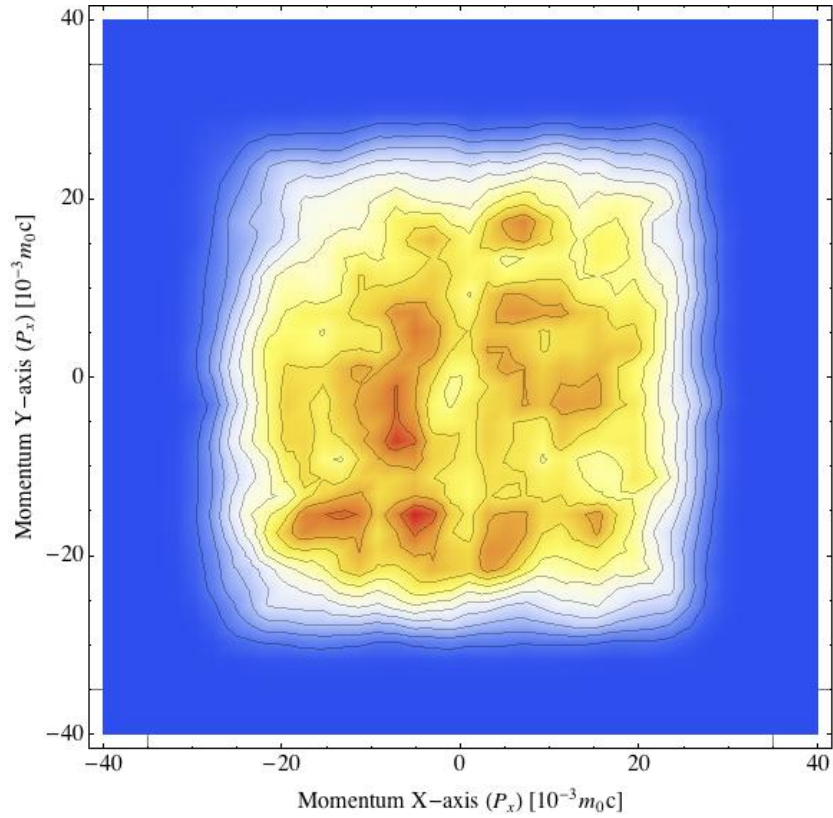


Figure 52: Raw ACAR spectrum for Ag:LTB, presented using a histogram contour plotting routine with a 1.5 mrad binning resolution, in electron momentum units of $10^{-3} m_0 c$. Red indicates higher counts and yellow lower counts, with blue being zero.

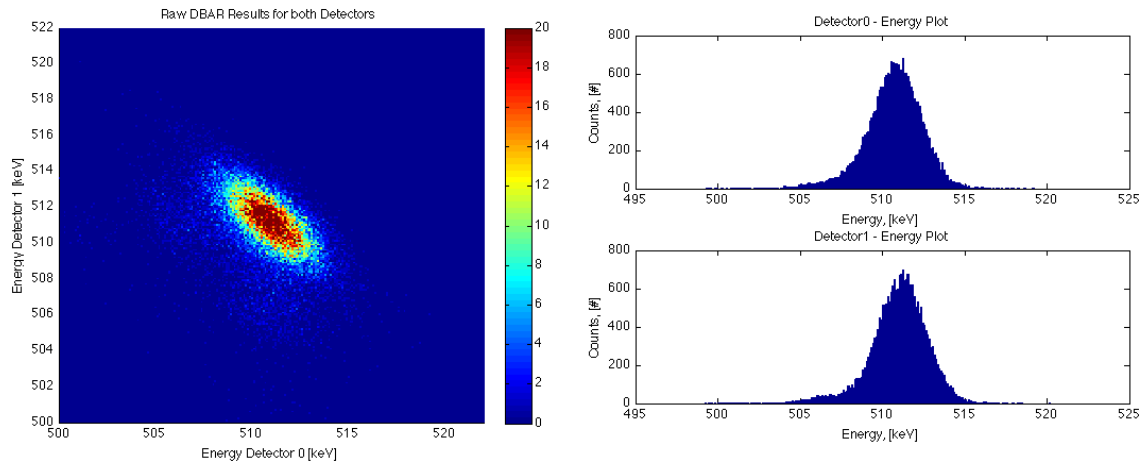


Figure 53: DBAR data for irradiated Ag:LTB. Left image shows raw DBAR results for both detectors together and right image shows energy plots for each detector individually.

Figure 54 below displays a series of plots representing CDBAR information about the X-ray-irradiated Ag:LTB sample. This data is plotted using a half-width of $\Delta = \pm 2$ keV in the left column and $\Delta = \pm 4$ keV in the right column for 0.3, 0.4, and 0.5 keV binning resolutions. As pointed out on the graphs themselves, there are several possible differential energy features located at ± 2 keV, ± 4 keV, ± 6 keV, and possibly around ± 8 keV. Again, the method in which these histograms are generated affects the Doppler-broadened lineshape.

Following this collection of plots is Figure 55, which depicts CDBAR graphs for the Ag:LTB dataset using only a 0.4 keV bin resolution for swath half-widths of $\Delta = \pm 2$ keV and ± 4 keV, for clarity. The blue lines in this figure are corrected for efficiency using the detector-normalized correction, which does smooth them reasonably (lower the error) as compared with the pixel-normalized correction and even seems to confirm some of the features noticed in the raw dataset as shown by the colored arrows. Figure 56, which follows, again depicts the same data as in the previous figure except now the blue lines represent correcting for efficiency using the average subpixel matrix calculated by Williams. Again, these tend to simply mirror the raw data, without boosting lower efficiency subpixels much at all.

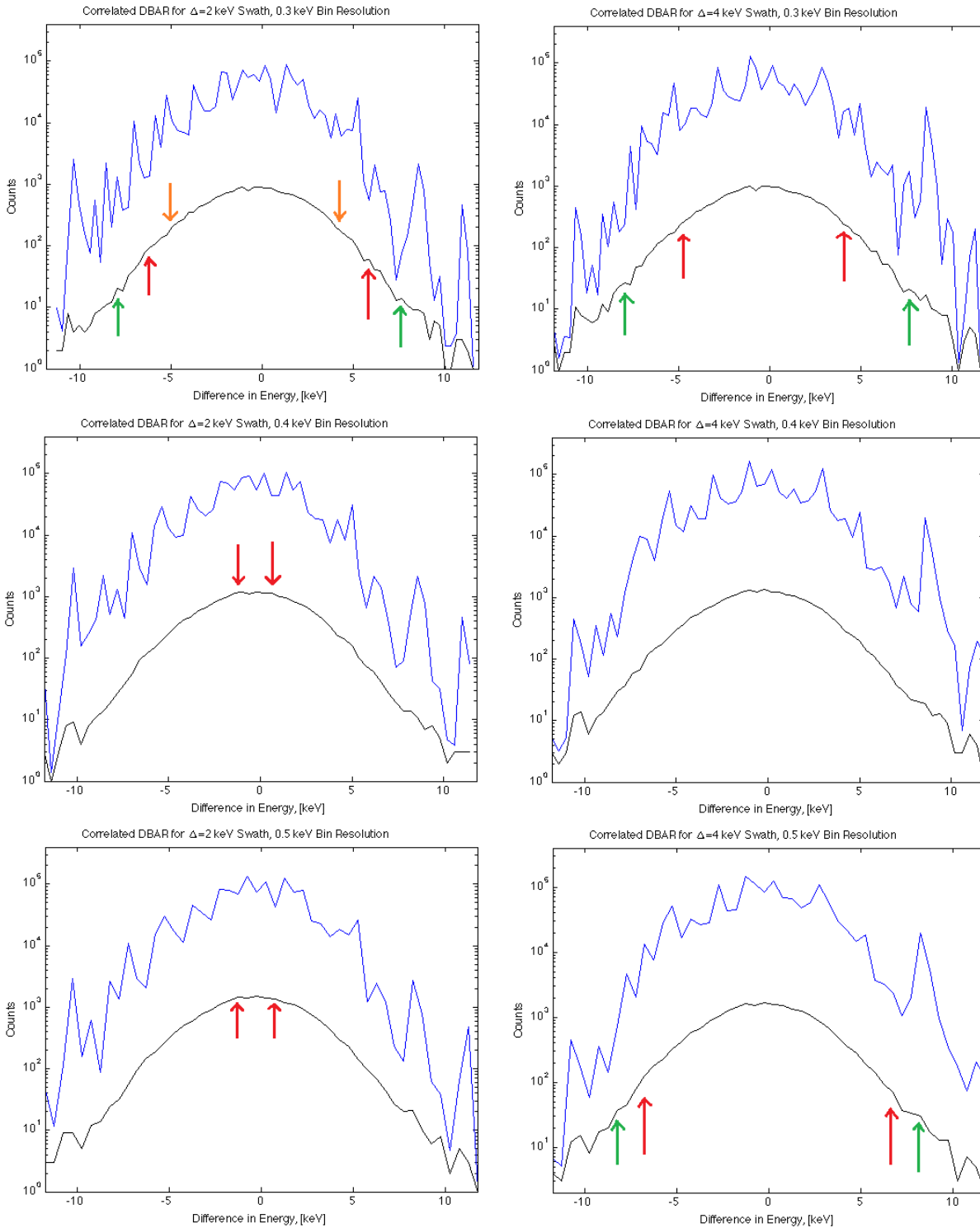


Figure 54: CDBAR results for irradiated Ag:LTB with $\Delta = \pm 2$ keV on left and ± 4 keV on right for 0.3, 0.4, and 0.5 keV energy binning resolutions. Black is raw data and blue is adjusted using the pixel-normalized efficiency correction.

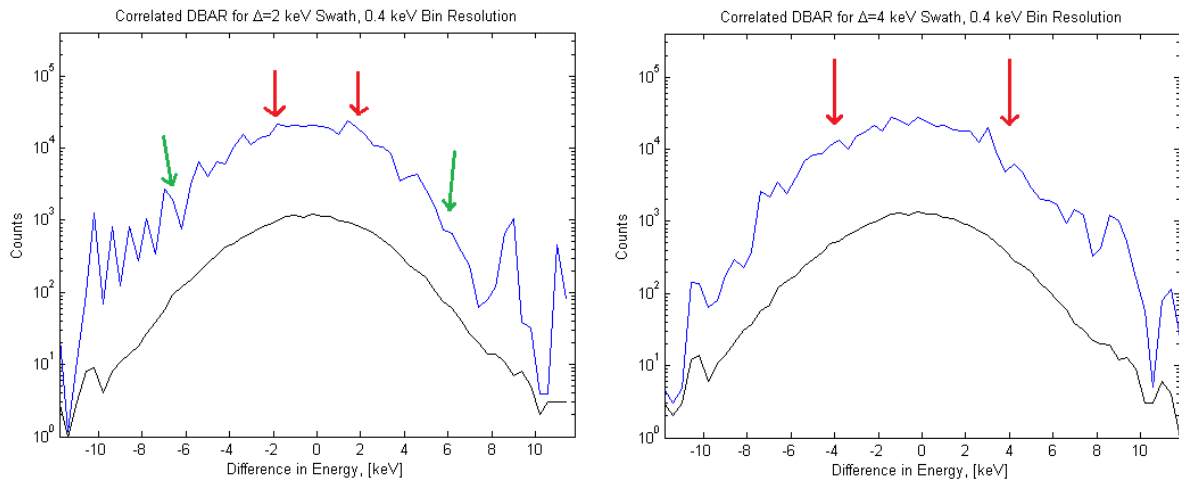


Figure 55: CDBAR results for irradiated Ag:LTB with $\Delta = \pm 2$ keV on left and ± 4 keV on right for 0.4 keV energy binning resolution. Black is raw data and blue is corrected using the detector-normalized efficiency correction.

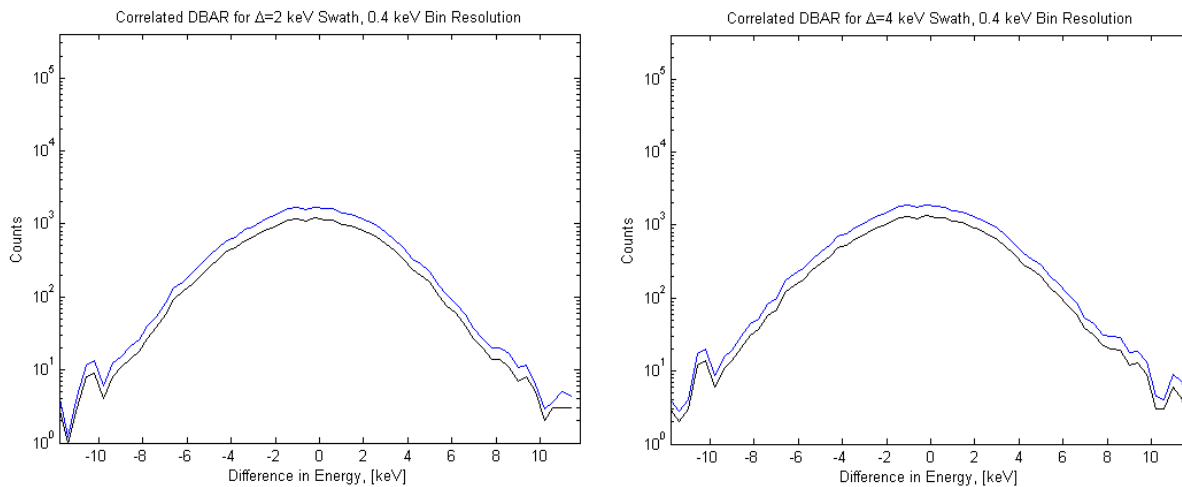


Figure 56: CDBAR results for irradiated Ag:LTB with $\Delta = \pm 2$ keV on left and ± 4 keV on right for 0.4 keV energy binning resolution. Black is raw data and blue is adjusted using the Williams efficiency correction.

5.5 Electron Momentum Distributions for LTB

Using the equivalency for angular deviation with electron momentum in ACAR and energy difference with electron momentum in DBAR noted in section 1.4, it is possible to translate potential features determined in experiment to actual electron momentum distribution features for LTB and its doped variants.

For the discrete ACAR plots, using Equation 1, a maximum angular deviation of ± 11 mrad for the virgin sample would mean that the electrons in the sample along the plane measured have at most $\pm 11 \times 10^{-3} m_0c$ momentum units in the (X,Y) direction. Likewise for the doped samples, this would mean the Cu-doped crystal has higher-momentum features up to $\pm 16 \times 10^{-3} m_0c$ or $\pm 18 \times 10^{-3} m_0c$ and the Ag-doped crystal has features up to about $\pm 15 \times 10^{-3} m_0c$. The smooth contour plots of the ACAR datasets generated in Mathematica show the electron momentum distributions in momenta units already. The features noted in the preceding sections for each sample for these contour plots tell us about recurring incidences of electron momenta values in the plane perpendicular to gamma emission, which provides a look at the overall electron momentum distribution in the respective sample for the specific orientation tested.

For DBAR, making use of Equation 2, the possible energy features located at ± 2 keV, ± 4 keV, ± 6 keV, and ± 8 keV would translate to $\pm 7.83 \times 10^{-3} m_0c$, $\pm 15.66 \times 10^{-3} m_0c$, $\pm 23.48 \times 10^{-3} m_0c$, and $\pm 31.31 \times 10^{-3} m_0c$ in the vertical direction, respectively. It is interesting to note that these features seem to appear in all three of the samples tested. The signal-to-noise ratio of the DBAR plots does not appear to allow determination of significant differences between samples. The fact that values close to $\pm 8 \times 10^{-3} m_0c$ appear in both ACAR and DBAR for the Cu:LTB sample is of interest.

5.6 Translations to Negative Defect Analysis

The spatial mapping of annihilation gamma radiation in two dimensions and the measurement of Doppler broadening of this radiation together will give a three-dimensional mapping of the momentum of the electrons in the sample prior to annihilation. From this, insight is gained into the electronic structure and chemical environment inside the sample material. In turn, the electronic structure tells about negative material defects such as electron vacancies and voids. It may also be useful in detecting impurity substitutions. The electron momenta features reported for the ACAR and DBAR results are indicative of the presence of defects in the LTB crystals. All the crystals were reportedly grown with the same intended defects. Similar ACAR and DBAR features do appear in the three crystals. The dominant mechanism is annihilation with valence electrons, as it is harder for the positron to penetrate down into the core electrons. In a semiconductor, the electrons are able to move freely around if excited to the conduction band. The electron momentum in the direction parallel to gamma emission would represent one-third of the total electron momentum, so features noted by DBAR would be 1/3 of the total momentum, just as features noted by ACAR would be 1/3 of total for each of the two directions. Confirmation of noted features and confident interpretation of applicability to electron structure and defect analysis can be performed by further correlating the DBAR lineshape curves with the ACAR plots. Constraining the DBAR data just by apparent features in the ACAR data would greatly improve the interpretability and significance of the results.

VI. Conclusions and Further Work

6.1 Conclusions for LTB 3D PAMS

The 3D PAMS experiment performed in this work on several different lithium tetraborate crystals resulted in a fairly significant amount of data. However, the count rates achieved in terms of coincident, full-energy events for each data set were lower than had been hoped, resulting in very long count times. Using PAS as an additional materials characterization method was important in investigating LTB, since other spectroscopic techniques have been or are currently being performed on this substance, and insight gained here can be combined with current and future knowledge of the structure of LTB crystals.

The ACAR spectra produced from the LTB samples were of some interest. Initially, it was uncertain how the crystal defects would be detected by positron annihilation spectroscopy because of the very low-Z nature of LTB, meaning there would be mainly low momentum electrons for interaction with positrons. The fact that the majority of coincident events recorded for LTB occurred with relatively little angular deviation makes sense because of its low-Z nature. When dopants were present, more events took place with higher angular deviations since Cu and Ag are higher in atomic number and therefore contain more electrons with higher momentum. Also, the defects created by the addition of the dopants seemed to add to the higher momentum features.

Unfortunately, the efficiency corrections used in this work were only correct for the central 8 x 8 pixels of the detector face because of interpolation issues in the outer strips. This, combined with the low count rates achieved, meant that correcting for efficiency did not contribute all that much to improving the ACAR results for the

discretely binned plots. The ACAR spectra generated in this work could potentially be ‘hiding’ information: many ACAR interpretation methods involve the use of a momentum sampling function [19], where because events representing lower momentum electrons are oversampled towards the center of the spectrum, a function can be developed based on the particular system which removes this oversampling ‘background’ effect and reveals stronger, distinct ACAR features below. The discretely binned ACAR plots do show some indication of an apparent diamond shape. Application of the momentum sampling function is highly recommended for these data plots.

For the ACAR histogram contour plots, apparent electron momenta features are present or are starting to form. A larger number of counts would be helpful in adding to the features. While there are some features common to all or to two of the samples, each sample does contain its own unique features not present in the others. The most interesting and easily identifiable difference in features is the presence of a (0,0) feature in both the pure LTB and Cu:LTB plots, but no such feature in the Ag:LTB plot. This could be due to the irradiation of the Ag:LTB sample. Perhaps the electrons are in excited states known as excitons because of irradiation, which leads to unfilled electron shells and therefore asymmetry in the shells (less contribution from lower-momentum s-shell electrons). Another alternative explanation would be that the irradiation simply causes more positron-trapping defects to anneal out, thus lowering the frequency of annihilation with valence electrons, which are lower-momentum. A third possible explanation would be that the irradiation is actually causing defects which are not present in LTB without irradiation. The explanation cannot be determined without measurement of an

unirradiated Ag:LTB sample. Comparison with an irradiated pure LTB and irradiated Cu:LTB sample would be useful in this analysis.

The DBAR spectra produced from the various LTB samples also contain useful information. They offer an alternative vantage point into the material structure of the crystals, investigating electron states from an alternate plane. One interesting thing to note is the lineshape of the raw DBAR curves. Sometimes this process is referred to as S and W parameter analysis, which would require a more quantitative comparison of lineshapes from defect-free samples and samples with defects. For the purposes of this work, in which even the pure LTB was grown with some defects, it is more useful to generally look at the overall lineshapes: we notice immediately that the lineshape of the Cu-doped sample is narrower and more peaked than that of the pure sample. The lineshape of the pure sample is in turn narrower than the rather flat, broad Ag-doped lineshape. Typically, narrower and peaked lineshapes indicate a higher concentration of defects than broader, wider lineshapes for DBAR. This is because the central portion of the DBAR curve represents annihilations with valence electrons and the outer, or ‘wing’ portions represent annihilations with core electrons. The increased presence of negative defects will result in a larger number of annihilations with valence electrons (and less with core electrons) because more vacancies will expose more valence electrons to the positrons.

While all three samples have defects, the concentration appears to be higher in the Cu-doped sample, and the concentration of defects seems lower in the Ag-doped sample (perhaps because of the X-ray irradiation ‘resetting’ the lattice chemically)—this would be opposite of the intent of using the X-rays to possibly create defects. While the

statistical relevance of the data sets was not ideal because of long counting times required of this sort of experiment, the beginnings of real features appear to be present in the data. The detector-normalized average relative subpixel efficiency correction did seem to provide some confirmation of potential CDBAR curve features by boosting them—this efficiency correction provided less noisy data than the pixel-normalized correction and more useful data than the Williams efficiency matrix applied to this system.

The ACAR and DBAR information gained is applicable to LTB, Cu:LTB, and Ag:LTB only in the crystal orientation that was employed. A different crystal orientation could yield different results. All three samples were measured in the same manner, with the only possible deviation being the lack of shielding around the manipulator arm for the copper-doped sample. Measuring the samples with the (001) plane aligned with the detector faces will be a useful next step to develop a standard for LTB.

6.2 Comparison to Previous Work

As compared to the work of Lt. Col. Christopher Williams with 6H SiC, this experiment was accomplished more quickly. The work with SiC, which made use of the same basic techniques using a different experimental setup testing different materials, resulted in significantly longer counting times with higher full-energy coincident counting rates, longer efficiency and energy calibration runs, and overall more statistically sound data. The time-constrained nature of this research was a good step in the right direction for expanding upon not only the previous work performed with this particular experimental setup, but also upon the work of other researchers performing

different techniques on these samples. This characterization was an excellent follow-on to and use of the work of Capt. Stephen Jimenez.

6.3 Impact of Results

The nature of this experiment, although involving several quantitative assessments and calculations, ultimately becomes a more qualitative piece of work. Combined 2D ACAR and CDBAR require rather complicated experimental setups with advanced equipment and well-thought out procedures. The information gained about a sample that is tested has the potential to be useful with significant thought and analysis, but its immediate applicability to a practical situation is not entirely apparent. Although some information is gained about defect concentration, further analysis and combination with other spectroscopy techniques would be necessary for determination of defect types. The electron momentum features discerned in this work could very well be important to the further characterization of lithium tetraborate as a scintillating radiation detector. The techniques developed and data gathered in this work can be further enhanced and built upon to improve the significance of the results.

6.4 Further Work

6.4.1 Positron Beam

The use of the AFIT positron beam system (Appendix E) in conjunction with the target chamber in this experiment would contribute greatly to the overall scientific merit of the work done. Unfortunately, the beam setup was not completed in time for use with the testing of these samples. The 50 mCi ^{22}Na capsule source specially designed and ordered for the positron beam arrived in the end of November 2012 at AFIT, after several

transporting delays. It was manufactured by iThemba LABS of South Africa. The source was installed inside the lead shield of the beam system and the entire shield chamber was sealed and placed under vacuum. The next step is to connect the beam's trapping section to the target chamber by means of the solenoid tube and bellows extender connection. Upon completion of testing in this work, the target chamber was moved for proper connection with the beam. The detectors must be realigned with the new location of the chamber and the connection between the chamber and beam must be made.

After connecting the beam to the target chamber and bringing the whole system under a collective vacuum, work remains to be done in terms of properly powering the magnetic trap coils, getting the software to properly control the physical operating components in the beam and trap, and ensuring the beam trap correctly gathers the right energy population of positrons and then releases them with proper timing onto the sample. The beam would allow significantly faster data collection rates: a sample could be measured in days as opposed to weeks or months for statistically relevant datasets. The beam, or 'active' method of PAS would allow investigators to look at characteristics at a particular depth in a sample, depending on beam energy. This would allow for surface characterization and beam profiling, while the current 'passive' setup can only be used in characterizing the bulk of the sample.

6.4.1 *ThO₂ and U:ThO₂*

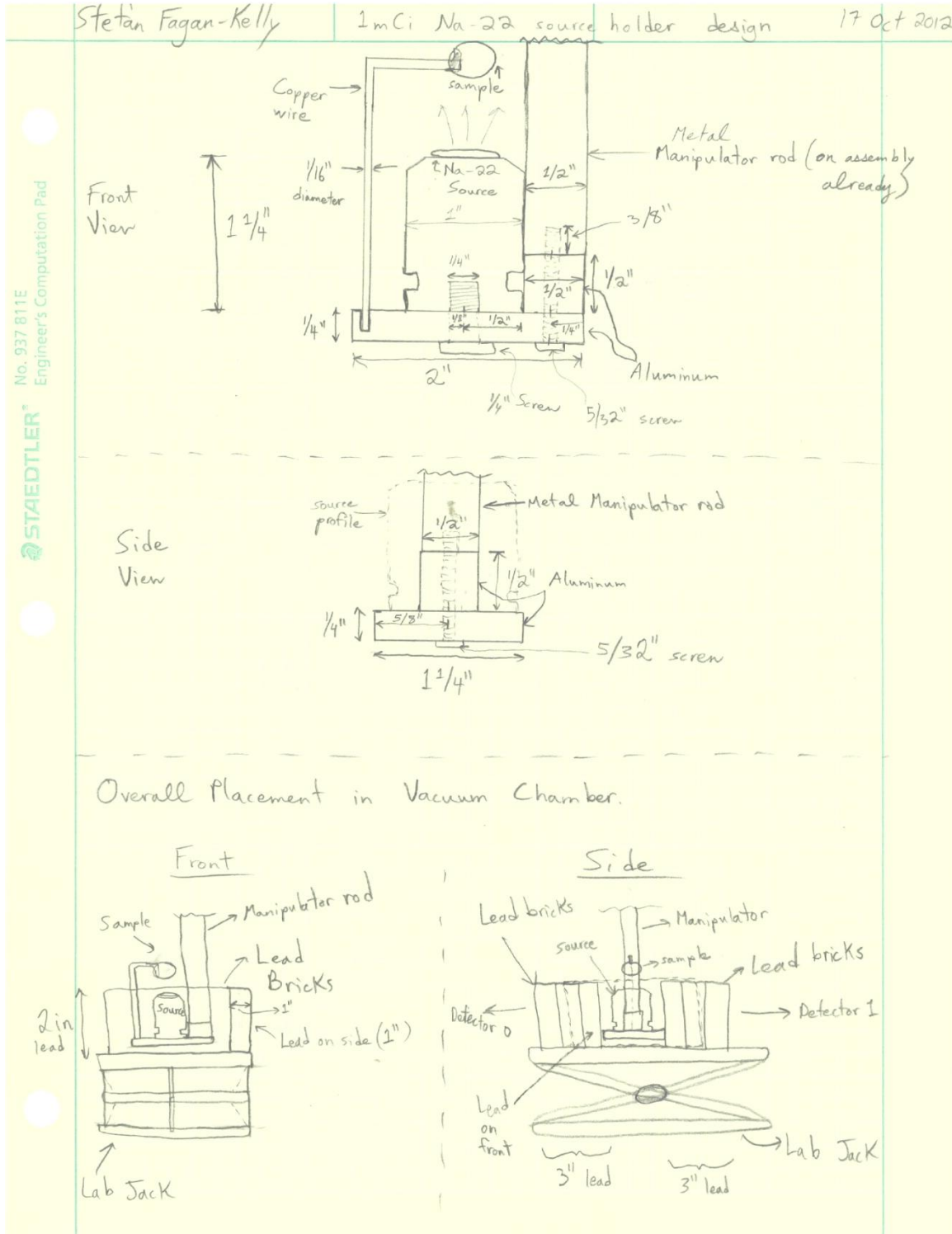
Testing of single-crystal undoped thorium oxide and uranium-doped thorium oxide is the next step for this experimental setup. Because of the high atomic number, or Z value, of thorium (90) and uranium (92), there is a larger number of electrons overall in each atom. This means that as the valence electrons are pushed further out from the

nucleus and more electrons are added in the core electron region, the core electrons become more tightly bound to the nucleus. This will result in a larger number of electrons with higher momentum towards the core as opposed to a lower-Z element such as lithium, boron, or oxygen. This means that positrons will interact and annihilate with larger numbers of higher-momenta electrons, which could show larger, more interesting features and designs on the ACAR and DBAR spectra for these crystals.

6.4.2 Data Analysis

Further work in terms of delving deeper into these datasets and developing new methods to analyze datasets in general using the PAS system at AFIT is necessary. Some areas for work include improved efficiency corrections, the application of plotting a DBAR curve using data constrained by features in the associated ACAR curve, the ability to utilize momentum sampling functions for ACAR spectra, the application of S and W parameter analysis for DBAR, the application of ratio curves in terms of quantitatively comparing defected samples with a pure sample (no defects), and a more quantitative method of choosing swath width and binning resolution for DBAR curves.

Appendix A: Source-Sample Mount Design



Appendix B: Data Parsing Code

Bash Script:

```
#!/bin/bash

#
# FilterEvents.sh (previously RemoveBackground2.sh)
#
# This script takes a Raw Event file from an Imager32/72
# and removes all events except for 2 or 4 events.
#
# Version History
#
# Tony Kelly          12/9/11
#   Script Creation
#   Takes 4 Event File
#
# Stephen Jimenez     12/16/11
#   Changed from 4 to 2 site events.
#
# Angelo Bonavita     08/16/12
#   Added capability to do a whole folder of files at once
#
#   Changed name from RemoveBackground2.sh to FilterEvents.sh

#clear

# First check that there are at least 2 arguments!
if [ $# -lt 2 ]
then
  echo "$0 : You must have at least 2 arguments: 1. # of events, 2. Name of File"
  exit 1
fi

echo
echo EventFilter Script
echo I am now filtering out all except $1 events.
echo ... One moment please ...
echo

# All additional arguments should be the file names to be filtered

#file_name=$2
#file_title=`echo $2|sed 's/\.\{3\}$//'^
#echo $file_title

# Using the fact that for implicitly loops over the arguments if you don't tell it what to loop over
for file_name;
do
  if [ $file_name == $1 ]
  then
    # Argument 1 should be a '2' or a '4', and tells the script which events to filter
    if [ $1 != 4 ] # -o [ $1 != 4 ]
    then
      echo "$0 : First argument must be a 2".          # OR statement needs fixing for a 4."
      echo "$0 : Your first argument was $1."
      exit 1
    fi
  fi
done
```

```

    fi
else
    # Remove extension from file name
    file_title=`echo $file_name|sed 's/\.\{3\}$//`

    # FILTER THE FILE!!!
    sed -n "/^[1-9].$1/p" ${file_title}.phd > ${file_title}_$1.phd

    echo "Done filtering file $file_title"
fi
done

echo Done!

##
# First verions of this file contained just this line!
#
# #sed -n '/^[1-9].4.[1-9].[1-9].[1-9].[481-541]/p' Cu_15min_120611_4.phd > Cu_15min_120611_4_E.phd
#

```

Matlab Parsing Code:

- Spect72 Raw Event Parser

```

%%% File Parser for PHDs Spec72 Energy Event Window Raw File
%%% Created on 1 Dec 2011 by smj
%%% Modifications:
%%% - 3 Feb 2012 by smj: Added NumSubStrips input so no longer hardcoded
%%% - 13 Nov 2012 by SFK: Fixed both 2 strip and 4 strip event case
%%%   matrix saving procedures at end
%%% Based on PHDs_EventWindowed_Reader.m created by 2nd Lt FitzGerald

function [SiteMat, SiteMatRaw, ttt]=Spec72Parser_RawEventv4(filename, EwinCent, deltaE,
NumSubStrips)
% % User Inputs
% filename - Takes *.phd raw event file from Imager72 Software
%           Format is [Event #, Event Count, Time, Slow Energy, Fast
%           Predecessor, Fast Successor]
% EwinCent - Center of Energy Window (keV) desired
% deltaE   - +/- of Center of Energy Window (keV)
% NumSubStrips - number of subpixel to interpolate the data

% % Outputs
% SiteMat   - matrix of parsed energy and subpixel locations
% SiteMatRaw - matrix raw but parsed data
% ttt      - time to read the entire file

% Calculates File Size
s = dir(filename);
filesize = s.bytes;
numlines = ceil(filesize / 28.2);

% Determines Energy Window Boundaries
E_low = EwinCent-deltaE;
E_high = EwinCent+deltaE;

% Skips Header
% Commented out since bash script removes the header - AMB
%Not commented out since this line is necessary to open the file. -SFK
fid = fopen(filename);

% Initialize Data Arrays

```

```

CaseInd = str2num(filename(end-4)); % Determines which part of switch
% statement that the File will look at.
if CaseInd==2
    OneSiteData=zeros(numlines,4);
    OneSiteData=zeros(1,4);
elseif CaseInd==4
    TwoSiteData=zeros(numlines,7);
    TwoSiteDataRow = zeros(1,7);
else
    disp('NOT A VALID FILE NAME!');
    disp('Run bash3 script named RemoveBackground.sh before analyzing data.');
```

end

```

linecount = 1;
writecount = 1;
writecountr = 1;

tic
%Loop through file. Look at each line (event) individually
while feof(fid) == 0

    %Make an array of 7 numbers from the given line
    % & Grab all events associated with first event.

    line_num = RawEventRead(fid);
    for i = 2:CaseInd;
        line_num(i,:) = RawEventRead(fid);
    end

    %Check to see if within the given energy range
    if ((line_num(:,5) >= E_low) & (line_num(:,5) <= E_high))

        switch CaseInd
            case 2 % The case for one-site events
                tBase = max(line_num(:,3));
                % if (tBase<=10 && line_num(1,3)~=line_num(2,3)); % doesn't look at
                events outside
                % of 200 ns (10 * time base which is 20 ns).
                OneSiteDataRow(writecountr:writecountr+1,:)=line_num;
                [Event2] =
                DPosCalc(NumSubStrips,line_num(:,4),line_num(:,5),line_num(:,6:7));
                if ((Event2(3) >= E_low) && (Event2(3) <= E_high))
                    OneSiteData(writecount,:) = [Event2 tBase];
                    writecount = writecount + 1;
                end
                writecountr = writecountr+2;
            end
            case 4 % The case for two strip charge sharing event or a one-site
                % event in each detector.
                tBase = max(line_num(:,3));
                % if (tBase<=10 && line_num(1,3)~=line_num(4,3)); % doesn't look at
                events outside
                % of 200ns (10 * time base which is 20 ns).
                TwoSiteDataRow(writecountr:writecountr+3,:)=line_num;
                [Event4] =
                DPosEng4Calc(NumSubStrips,line_num(:,4),line_num(:,5),line_num(:,6:7));
                if (Event4(3)>=E_low && Event4(3)<=E_high && Event4(6)>=E_low &&
                Event4(6)<=E_high)
                    TwoSiteData(writecount,:) = [Event4 tBase];
                    writecount = writecount + 1;
                end
                writecountr = writecountr + 4;
            end
            otherwise
        end
    end
end
end

```



```

linecount = linecount + line_num(1,2);
if mod(linecount,10000)==1
    percent = linecount/numlines*100;
    fprintf('%f percent complete\n',percent);
end
end
ttt = toc;
fclose(fid);
if CaseInd==2 %&& isempty(OneSiteDataRow)==0 && isempty(OneSiteData)==0)
    %indices = find(OneSiteData(1:3));
    %SiteMat = OneSiteData(1:length(indices)/3,:);
    %SiteMatRaw = OneSiteDataRow(2:end,:);
    SiteMat = OneSiteData;
    SiteMatRaw = OneSiteDataRow(2:end,:);
    ncol = 4;
    extenstr = '_1Site.mat';
elseif CaseInd == 4 %&& isempty(TwoSiteDataRow)==0 && isempty(TwoSiteData)==0)
    %indices = find(TwoSiteData(1:6));
    %SiteMat = TwoSiteData(1:length(indices)/6,:);
    %SiteMatRaw = TwoSiteDataRow(2:end,:);
    SiteMat = TwoSiteData;
    SiteMatRaw = TwoSiteDataRow(2:end,:);
    ncol=7;
    extenstr = '_2Site.mat';
else
    disp('NOT A VALID FILE NAME!');
    disp('How you got here is beyond me!');
end
if isempty(SiteMat)==0
%SiteMat = reshape(SiteMat,size(SiteMat,1)/ncol,ncol);
end
end
end

```

- Spect72 Multi Raw Event Files Parser Script

```

%% File Parse for PHDs Spec72 Energy Event Window Raw Files in a Single
%% Folder
%% Created on 13 Dec 2011 by smj
%% 13 Nov 2012 by SFK, fixed data matrix saving procedures at end
%% Based on FMSEAnalysis.m created by Capt Stephen M. Jimenez

function Spec72Parser_MultiRawEventFiles(Material, Energy, deltaE, CaseInd, NumSubs)
% % User Inputs
% Material - prefix of the file names desired to be analyzed to include the
%             underscore
%             - e.g.'CuSS_' for Copper Standard Source
% EwinCent - Center of Energy Window (keV) desired
% deltaE - +/- of Center of Energy Window (keV)
% CaseInd - suffix of the filed names desired to be analyzed
%             - 2 for 2-strip events or 4 for 4-strip events
% NumSubs - number of subpixel (substrips per pixel) to interpolate the data

% Determines file extension to look for depending on whether user wants to
% look at two or four site events.
Material='LTBAGIrr_';
Energy=511;
deltaE=12;
CaseInd=4;
NumSubs=5;

exten = ['_' num2str(CaseInd) '.phd'];

```

```

if CaseInd == 2
    ncol = 4;
elseif CaseInd ==4
    ncol = 7;

end

folder = uigetdir('/Users/sfagan-kelly/Desktop/LTBAgIrrCalc/8th calc');
s = dir(folder);
temp = struct2cell(s);
ind = find(strncmp(Material,temp,length(Material)));
temp = temp(ind);

% Displays all the *.exten files that are found in the folder specified
count = 1;
filenames = [];
disp(['Starting analysis of the following files in ' folder ':']);
for i=1:length(temp)
    fname = temp(i);
    fname = cell2mat(fname);
    if strcmp(fname(end-5:end),exten)
        filenames(count) = fname;
        disp(fname);
        count = count +1;
    end
end
innnput = input('Are these the files you wish to analyze?');

% Initalize final data matrices
Data = zeros(1000,ncol);
writecount = 1;
DataRow = zeros(1,7);

% Goes thru each file, parses it, and combines data into two matrices
for i = 1:length(filenames)
    tempfName = cell2mat(filenames(i));
    disp(['Beginning file: ' tempfName ]);
    [tempData, tempDataRow, time1(i)] = Spec72Parser_RawEventv4([folder '/'
tempfName],Energy,deltaE,NumSubs);
    blocksize = writecount+size(tempData,1)-1;
    Data(writecount:blocksize,:) = tempData;
    DataRow = [DataRow; tempDataRow];
    disp(['Time to run ' tempfName ' was ' num2str(time1(i)) '.']);
    writecount = blocksize+1;

% Saves Subpixel and Raw Data for all the files in two matrices - sep files
%ParseInfo = [filenames' num2cell(time1)']
SaveNameRaw = [folder '/' tempfName 'Raw_Data_Parsed_on_' date '.mat'];
SaveName = [folder '/' tempfName 'Subpixel_Data_Parsed_on_' date '.mat'];
%indices = find(Data);
%Data = Data(indices);
%Data = reshape(Data,size(Data,1)/ncol,ncol);
save(SaveName,'Data');
save(SaveNameRaw,'DataRow');

%Reset data matrices for next file
Data = zeros(1000,ncol);
writecount = 1;
DataRow = zeros(1,7);
end
end

```

Appendix C: Data Analysis Code

Mathematica Efficiency and Resolution Calculation:

DSSD Efficiency and Resolution Calculation

File: Detector 1 Calculation

Created by Angelo Bonavita
4 Sept 2012

Modified by Stefan Fagan-Kelly
9 Oct 2012

Summary of File

1. Import data from MATLAB
2. Bin data into a matrix of pixels and matrix of subpixels
3. Efficiency: Calculate mean efficiency across the detector along with standard deviation
4. Energy Resolution: Calculate mean energy collected and the standard deviation of the energy collected across detector
5. Individual Pixel Exploration

After data was collected from the DSSD, data that was detected in 2 strips simultaneously was extracted using a stream editor. The resulting 2 event only file was scanned through by MATLAB, and only those 2-strip events with energies in a user selected range (514 +/- 10 keV) were extracted. The code below imports those data points, sorts them into detector pixels (in a 16x16 detector), and calculates the FWHM of each pixel.

Importing Data & Setting up Detector Matrices

Import MATLAB file

```
(* matlabImport=Import["E:\Classes\WENG 612 - Adv Nuk Lab\Project\Det0\Sr85-Det0-5_2.sub.mat", "LabeledData"]; *)
```

```
matlabImport = Import["/Users/sfagan-kelly/Desktop/Sr85CalibrationFINAL/5x5 subpixel-parsed/Sr85_Det1EffCal19Oct_RawEventFile_2.phdSubpixel_Data_Parsed_on_23-Oct-2012.mat",  
"LabeledData"];
```

subData contains the subpixel information of each event sorted through by MatLab. subData[[2]] is an example of the subPixel data stored in the array.

```
subData = matlabImport [[1, 2]];  
subData [[2]]  
Length[subData]  
{88., 62., 513.42, 2.}  
486229
```

This next command should reduce subdata to JUST Detector 1 data, which will have subpixel channels below and including $32*5 = 160$.

```
subData = DeleteCases[subData, x_ /; x[[1]] > 160];  
subData [[2]]  
Length[subData]  
{88., 62., 513.42, 2.}  
483695
```

subData is a $N \times 4$ array of the description of each event by subpixel. Every row in the array has the structure {AC Subpixel, DC subpixel, Average Energy, Time Frame}. The original 16x16 pixel array was sub-divided into an 80x80 array, using the FOM of the charge transients to guide which subpixel the event occurred in. Each time frame represents a 20ns time window.

For this experiment, we are going to re-bin back into the 16x16 array, to get the energy resolution for each pixel. The first index of the Detector tensor is the DC pixel, and the second is the AC pixel. The third index will hold the average energy data of the event imported from MATLAB. The first element of the index will be a count of the number of rows of data it contains, up to (an arbitrarily chosen number). All subsequent elements of the third index will be the actual data.

The pixel that each row belongs to is just (SubPixel / #SubPixels/Pixel) when the indices are [0,15], but our array indices are [1,16], so add 1 to each subpixel index.

```

FullDetector = Table[0, {i, 1, 16*5}, {j, 1, 16*5}, {ct, 1, 1000}];
Detector = Table[0, {i, 1, 16}, {j, 1, 16}, {ct, 1, 5000}];
rowMax = Length[subData];
For[n = 1, n <= rowMax, n++,
  For[side = 1, side <= 2, side++,
    If[Floor[subData[[n]][[side]]/5] == subData[[n]][[side]]/5,
      tempPix = (subData[[n]][[side]])/5,
      tempPix = Floor[(subData[[n]][[side]])/5] + 1
    ];
    If[(subData[[n]][[side]]) <= (16*5),
      DCpix = tempPix; (* if true *)
      fDCpix = (subData[[n]][[side]]),
      ACpix = tempPix - 16; (* if false *)
      fACpix = (subData[[n]][[side]]) - 80
    ]
  ];
  count = Detector[[DCpix, ACpix]][[1]] + 1;
  Detector[[DCpix, ACpix]][[count + 1]] = subData[[n]][[3]];
  Detector[[DCpix, ACpix]][[1]] = count;

  fcount = FullDetector[[fDCpix, fACpix]][[1]] + 1;
  FullDetector[[fDCpix, fACpix]][[fcount + 1]] = subData[[n]][[3]];
  FullDetector[[fDCpix, fACpix]][[1]] = fcount;
];

```

Summary of File Contents

The third index of Detector and Full detector needs to be adjusted as the file sizes increase. An error occurs if more data points for a particular pixel exist than the length of this index allows for.

```

Max[Detector[[All, All, 1]]]
(* This is the maximum number of counts in any pixel *)
Max[FullDetector[[All, All, 1]]]
2441
899

```

The sum of the number of counts in each pixel of the matrix above is equivalent to the length of the imported MATLab matrix.

```

rowMax
483695
Total[Total[Detector[[All, All, 1]]]]
Total[Total[FullDetector[[All, All, 1]]]]
483695
483695

```

The Detector matrix is a representation of the detector as an array of 16x16 pixels, showing the number of incident particles in each. While there are 256 blocks, the '0' values in 24 blocks represents the corners where the strip detectors do not reach. (256-24) = 232 pixels where charge is suspected to be. The actual detector possesses 220 pixels -- areas where two strips intersect. This means that 12 "virtual" pixels are represented in this matrix due to interpolation.

```

MatrixForm[Detector[[All, All, 1]]]
ListPlot3D[Detector[[All, All, 1]]]

```

0	0	0	118	1232	2304	2265	2154	2218	2254	2193	1166	74	0	0	0
0	0	427	2182	2182	2181	2226	2200	2076	2194	2167	2151	2083	381	0	0
0	444	2263	2240	2248	2155	2229	2125	2128	2158	2125	2182	2162	2221	369	0
75	2205	2215	2400	2289	2344	2282	2327	2241	2309	2358	2256	2269	2207	2043	27
1060	2221	2250	2193	2327	2402	2302	2265	2257	2312	2312	2291	2291	2167	2233	902
2105	2183	2219	2198	2388	2350	2240	2387	2312	2279	2223	2338	2386	2362	2261	1764
2136	2247	2283	2370	2338	2271	2304	2364	2272	2368	2279	2253	2306	2284	2309	1836
2152	2405	2231	2274	2327	2249	2332	2333	2313	2359	2260	2313	2249	2303	2382	1892
2106	2296	2310	2320	2322	2337	2441	2344	2390	2428	2356	2325	2329	2283	2267	1888
2110	2327	2300	2293	2323	2395	2325	2400	2337	2367	2337	2363	2272	2314	2290	1837
2049	2375	2265	2261	2296	2391	2359	2353	2161	2309	2318	2411	2395	2379	2431	1804
1149	2266	2264	2374	2222	2418	2325	2265	2243	2355	2316	2279	2292	2412	2341	894
66	2226	2298	2244	2337	2226	2392	2276	2263	2286	2335	2310	2326	2401	2041	14
0	427	2237	2267	2218	2281	2289	2291	2280	2379	2359	2311	2298	2350	325	0
0	0	450	2236	2213	2366	2253	2229	2229	2220	2232	2283	2065	380	0	0
0	0	0	104	1349	2252	2286	2261	2197	2286	2202	1187	60	0	0	0

```
ListContourPlot[Detector[[All, All, 1]]]
```

In Steve Jimenez's MATLab code, each pixel can be sub-divided into user defined subpixels. For this run, 5 subpixels per detector was selected. The Matrix below represents the charge distribution as determined by Steve's code if each pixel was represented by a 5x5 subpixel matrix.

```
MatrixForm[FullDetector[[All, All, 1]]];
```

```
ListPlot3D[FullDetector[[All, All, 1]]]
```

```
ListContourPlot[FullDetector[[All, All, 1]], PlotLabel -> "Subpixel Counts - Detector 1", BaseStyle -> {FontSize -> 16}]
```

Efficiency

It is desired to calculate the Efficiency of each individual pixel of the detector. We have already collected a count of the number of full energy incident particles on each pixel. The efficiency could be calculated relative to the maximum count, to get an efficiency relative to each other, or it can be calculated based on the number of incident particles expected from the source. The following is the later. This count ignores less energy counts that ended up compton scattering.

Variable Initialization

First, I need to setup variables associated with the geometry of the system.

```
d = 457.2;
```

```
(* distance on centerline from source to detector [mm]*)
```

```
g = 0.25; (* gap between strips on detector [mm]*)
```

```
w = 4.75; (* width of each strip on detector [mm]*)
```

Second, I need to setup variables associated with the strength of the source

```
A0 = 100.8;
```

```
(*μCi*)
```

```
A0 = A0 (10-6) (3.7 × 1010); (* Convert from μCi to Bq or dps*)
```

```
tHalf = 64.84; (* Half-Life of source. 64.84 days for Sr-85 *)
```

```
dateCalib = {2012, 07, 1, 12, 0, 0}; (* This is the date the source is calibrated - listed on source *)
```

```
dateExp = {2012, 10, 19, 12, 0, 0}; (* This is the date that the experiment took place *)
```

```
tMeas = 480 * 60; (* time of measurement or count time [min converted to seconds] *)
```

Also, the following functions are useful for evaluation...

```
GaussSpec[x_] :=  $\frac{1}{\sigma\sqrt{2\pi}} e^{-\frac{(x-\mu)^2}{2\sigma^2}}$ ;
```

```
std[x_List] := Which[(Length[x] == 1) || (Length[x] == 0), 0, True, StandardDeviation[x]] (* Define Std Dev of 1 as 0 - just in case *)
```

Solid Angle Calculation

Each strip is 5mm wide, making each square pixel 5^2 mm^2 . The source was placed 30 cm from the face of the detector. The solid angle (Ω) is the ratio of the area of interest to the 4π area. Thus a pixel on the centerline would have a solid angle of:

$$\Omega_{cl} = \frac{w^2}{4\pi d^2};$$

Pixels off centerline have a reduced solid angle, because the normal to the surface is not the same as the vector to the source. Multiplying Ω_{cl} by the $\text{Cos } \theta$ between the centerline, and the vector from the source to the pixel gets the appropriate solid angle. The equation is in terms of a pixel (n,m) where the centerline is between strips 8 and 9. The shift of -8 allows the use of the convention that strip 1 is the left-most strip, which is the 8th strip from the centerline.

$$\Omega[n_, m_] := \Omega_{cl} \frac{d}{\sqrt{d^2 + (g+w)^2 \left(((n-8) - 0.5)^2 + ((m-8) - 0.5)^2 \right)}};$$

Source Activity at time of experiment

The solid angle needs to be multiplied by the source. We could use a normalized source of 1, but we will use the actual activity of the source.

```
tDecay = DateDifference[dateCalib, dateExp] (* days *)
110
A = A0 Exp[-Log[2] tDecay / tHalf] (* Bq *)
1.15072 × 106
```

Efficiency of Across the Detector

Loop through every pixel in the detector. Calculated the expected count from the specific solid angle of the pixel. Use counts measured to find efficiency. Create a matrix containing the efficiency of each pixel.

```
effData = Table[0, {i, 1, 16}, {j, 1, 16}];
For[i = 1, i ≤ 16, i++,
  For[j = 1, j ≤ 16, j++,
    If[Detector[[i, j, 1]] > 0, (* This IF isn't needed *)
      TotCnts = A Ω[i, j] tMeas; (* Calc expected counts based on Ω of specific pixel *)
      effData[[i, j]] = Detector[[i, j, 1]] * 100 / TotCnts; (* Calc efficiency using the counts measured [%] *)
    ];
  ];
MatrixForm[effData];
ListPlot3D[effData]

ListContourPlot[effData, ContourLabels → All, PlotLabel → "Detector 1 Efficiency [%]", BaseStyle → {FontSize → 16}]
```

The Distribution of the Efficiency

The mean efficiency and the standard deviation of the efficiency is desired. However,

```
Average = Mean[Flatten[effData]]
STDDEV = StandardDeviation[Flatten[effData]]
0.665079
0.28447
denseEff = Take[effData, {3, 14}, {3, 14}];
MatrixForm[denseEff];
ListPlot3D[denseEff]

μ = Mean[Flatten[denseEff]]
σ = StandardDeviation[Flatten[denseEff]]
start = Min[denseEff];
end = Max[denseEff];
Plot[GaussSpec[x], {x, start, end}]
Histogram[Flatten[denseEff], 20]
0.808994
```

0.0229583

Energy Resolution

We can now figure out the energy resolution for each pixel above by simply looping through each pixel, and calculating the mean energy and its standard deviation. I will create a 16x16 array, like detector above, which will store an ordered pair consisting of the average energy and standard deviation of the incident radiation on that pixel. The third entry contains the FWHM for convenience since that is often desired over the σ .

```
GaussSpec[x_] :=  $\frac{1}{\sqrt{2\pi}\sigma} e^{-\frac{(x-\mu)^2}{2\sigma^2}}$ ;
std[x_List] := Which[(Length[x] == 1) || (Length[x] == 0), 0, True, StandardDeviation[x]] (* Define Std Dev of 1 as 0 - just in case *)
pixelData = Table[0, {i, 1, 16}, {j, 1, 16}, {op, 1, 3}];
pixelSpectra = Table[0, {i, 1, 16}, {j, 1, 16}];
pixelShort = Table[0, {i, 1, 16}, {j, 1, 16}];
For[i = 1, i ≤ 16, i++,
  For[j = 1, j ≤ 16, j++,
    If[Detector[[i, j, 1]] > 0,
      pixelSpectra[[i, j]] = Take[Detector[[i, j]], {2, Detector[[i, j, 1]]}];
      pixelShort[[i, j]] = DeleteCases[pixelSpectra[[i, j]], x_ /; x < 512.0];
      pixelData[[i, j, 1]] = Mean[pixelSpectra[[i, j]]]; (* μ *)
      (* pixelData[[i, j, 1]] = Mean[pixelShort[[i, j]]]; *) (* μ *)
      (* pixelData[[i, j, 2]] = std[pixelSpectra[[i, j]]]; *) (* σ *)
      pixelData[[i, j, 2]] = std[pixelShort[[i, j]]]; (* σ *)
      pixelData[[i, j, 3]] = 2  $\sqrt{2 \text{Log}[2]}$  pixelData[[i, j, 2]], (* FWHM *)
    ];
  ];
];
```

Weighted Energy at Peak

```
Mean[Flatten[pixelSpectra[[All, All]]]]
StandardDeviation[Flatten[pixelSpectra[[All, All]]]]
513.92
3.82503
```

Using the Short List

```
Mean[Flatten[pixelShort[[All, All]]]]
StandardDeviation[Flatten[pixelShort[[All, All]]]]
514.138
3.80741
```

Table of Standard Deviation

```
sigmaArray = pixelData[[All, All, 2]];
(* Table of Standard Deviations *)
MatrixForm[sigmaArray];
```

With the mean and standard deviation data, we can plot a gaussian representing the energy peak using...

Table of FWHM

```
FWHMArray = pixelData[[All, All, 3]];
```

```
(* Table of FWHM *)
```

```
MatrixForm[FWHMArray]
```

```

0      0      0      1.7365  2.11671  2.01629  2.00945  2.03758  1.80921  1.85559  1.88609  1.94632  1.90787  0      0      0
0      0      1.91711  1.7448  1.87238  1.81839  1.85719  1.85832  1.77195  1.88609  1.79501  1.7553  1.8251  1.98075  0      0
0      2.19474  1.75839  1.70468  1.79227  1.81193  1.8549  1.83919  1.75706  1.9184  1.63935  1.706  1.74542  1.79047  2.01358  0
1.79604 1.86402 1.77846 1.82906 1.73465 1.85601 1.85203 1.76498 1.8836 1.77805 1.64645 1.71955 1.82624 1.68303 1.95317 2.06611
1.83186 1.77596 1.7583 1.63167 1.74588 1.71581 1.83544 1.79186 1.71012 1.71463 1.62935 1.82354 1.73845 1.79465 1.9275 2.0067
1.79703 1.80793 1.67525 1.73735 1.70096 1.9387 1.9879 1.8388 1.73788 1.7065 1.75071 1.73396 1.60695 1.83117 1.95934 2.03564
1.80243 1.66829 1.85819 1.65465 1.89745 1.72667 1.78575 1.85456 1.86121 1.85224 1.73228 1.74918 1.80288 1.75314 1.98957 2.00423
1.93086 1.65544 1.6423 1.7668 1.70675 1.79387 2.07956 1.83885 1.7554 2.04402 1.65702 1.80033 1.70821 1.66471 1.90849 1.9984
1.86235 1.80937 1.83083 1.7364 1.7053 1.7325 1.80948 1.84588 1.93486 1.80122 1.75927 1.771 1.75276 1.83887 1.84389 1.90422
1.95238 1.87081 1.75794 1.70918 1.81137 1.8229 1.8866 1.92332 1.8669 1.75627 1.69074 1.82066 1.72583 1.76989 1.88857 1.91652
1.97289 1.84593 1.75257 1.75365 1.69943 1.72605 1.83131 1.70895 1.68498 1.73374 1.84133 1.6872 1.62925 1.67416 1.78678 1.72446
1.74956 1.86822 1.67708 1.71582 1.72904 1.8764 1.84805 1.70348 1.8482 1.89639 1.62372 1.74116 1.73067 1.80161 1.86565 1.83942
1.91787 1.88163 1.71232 1.76582 1.64627 1.67159 2.05952 1.67494 1.67939 1.6977 1.68253 1.67818 1.78018 1.70912 1.82747 2.19233
0      1.78898 1.71566 1.86791 1.7949 1.79502 1.7939 1.82023 1.8774 1.69927 1.62106 1.62501 1.79898 1.81752 2.03457 0
0      0      2.03423 1.7703 1.89684 1.81739 1.89911 1.72567 1.83313 1.78666 1.71167 1.89818 1.92568 2.11157 0 0
0      0      0      1.84517 1.82871 1.72509 1.86493 1.75113 1.84283 1.96994 1.9225 2.00395 1.85061 0 0 0

```

```
ListPlot3D[FWHMArray]
```

```
ListContourPlot[FWHMArray, ContourLabels -> All, PlotLabel -> "Detector 1 Resolution as FWHM [keV]", BaseStyle -> {FontSize -> 16}]
```

Let's take a look at the FWHM data as an average over the entire detector. First, I need to remove the zeroes from the data, or it will broaden my distribution

Distribution of the Full Width Half Max

This section calculates the average FWHM across the center of the detector. Since the strips on the ends show significant differences, I am removing the data from strips 1,2,15, & 16 from both AC and DC sides. The following average only applies to the 10x10 array of strips closest to the center of the detector.

First, we discover the maximum and minimum FWHM for any individual pixel.

```

Max[FWHMArray]
Min[DeleteCases[Flatten[FWHMArray], x_ /; x == 0]]
2.19474
1.60695
denseFWHM = Take[FWHMArray, {3, 14}, {3, 14}];
MatrixForm[denseFWHM];
μ = Mean[Flatten[denseFWHM]]
σ = StandardDeviation[Flatten[denseFWHM]]
start = Min[denseFWHM];
end = Max[denseFWHM];
Plot[GaussSpec[x], {x, start, end}]
Histogram[Flatten[denseFWHM], 20]
1.7691
0.087792

```

Distribution of the Full Width Half Max (No minipulation)

This section calculates the average FWHM across the entire detector, in contrast with the calculation above. It does not however remove the zero values in the corner of the matrix that represent coordinates which the circular detector does not reach. I kept this in place so that I could remind myself how much this skews the results.

```

μ = Mean[Flatten[FWHMArray]]
σ = StandardDeviation[Flatten[FWHMArray]]
start = Min[FWHMArray];
end = Max[FWHMArray];
Plot[GaussSpec[x], {x, start, end}]
Histogram[Flatten[FWHMArray], 20]

```


1.64258
0.539841

Individual pixel Exploration

Choose a pixel...

i = 7;
j = 8;

Efficiency of Pixel

```
TotCnts = A $\Omega$ [i, j] tMeas  
Eff = Detector[[i, j, 1]] * 100 / TotCnts (* As a percent *)  
284618.  
0.830587
```

Energy Resolution

The following calculates the mean and standard deviation of the energy about the 514keV peak measured in this particular pixel. The histogram is the data this curve is based upon.

NOTE: An error occurs if a pixel that registered NO counts was selected to explore.

```
 $\mu$  = pixelData[[i, j]][[1]];  
 $\sigma$  = pixelData[[i, j]][[2]];  
start = Min[pixelSpectra[[i, j]]];  
end = Max[pixelSpectra[[i, j]]];  
gPlot = Plot[GaussSpec[x], {x, start, end}, PlotRange -> {Full, {0, 0.6}}];  
hPlot = Histogram[pixelSpectra[[i, j]], 50, "PDF"];  
Show[gPlot, hPlot, PlotRangeClipping -> False]
```

Matlab Efficiency Correction Calculation:

```
%% Simultaneous 2D-ACAR and CDBAR Experiment Data Analysis tool for 3DPASS  
%% using AFRM Vacuum Chamber and two PHDs high purity germanium (HPGe)  
%% 16x16 double sided strip detectors (DSSDs).  
%% Created on 12 Dec 2011 by smj  
%% Based on Williams Dissertation Section 4.9 Simultaneous 2D ACAR and  
%% CDBAR Experiment  
  
%% Creates the average relative efficiency matrices for each detector to  
%% be used in the ThreeDPASSCalc3.m  
%% Created on 26 Jan 2012 by smj  
%% Based on Williams Dissertation Section 4.9: Simultaneous 2D ACAR and  
%% CDBAR Experiment  
  
%% Modified by SFK 17 DEC 2012  
%% Attempt to debug for new detector setup with Det 1 rotated around by  
%% 180 degrees  
  
function ThreeDPASSEfficiencyCalc(Data, EwinCent, deltaE, timevar, subsperpixel, plotind)  
% % User Inputs  
% Data - Parsed file output from Spec72Parser_RawEventv2.m or from  
% Spec72Parser_WinEvent.m including only 2-strip events with the  
% following formats as of 17 Dec 2012:  
% Raw Format = [AC Pixel, DC Pixel, Energy, Time Stamp (number of 20ns ticks)]  
% Win Format = [AC Pixel, DC Pixel, Energy]  
% EwinCent - Center of Energy Window (keV) desired  
% deltaE - +/- of Center of Energy Window (keV)  
% timevar - number of 20ns time intervals to limit data.  
% subsperpixel - how many subpixels to use in the program; usually use 5  
% plotind - logical if plots are desired to be seen.  
  
%load([pwd '/Efficiencynoswap.mat']);
```

```

%EwinCent=514;
%deltaE=10;
%timevar=4;
%subsperpixel=5;
%plotind=true;

% Defines number of subpixels
NumSubStrips = subsperpixel*16;
stripwidth = 4.75;      % PHDs DSSD strip width in mm
gapwidth = 0.25;       % PHDs DSSD gap width in mm

% Filter data to include only specific energies
ind = find(Data(:,3)>=(EwinCent-deltaE) & Data(:,3)<=(EwinCent+deltaE));
Data = Data(ind,:);

% Filter data to include only time differences
indt=find(Data(:,4)<=timevar);
Data = Data(indt,:);

% Filter Data into separate matrices for each detector
% Swapped '<=' and '>' to match equipment setup - AMB
% Swapped last 3 lines, 'Det0' for 'Det1' - AMB
% Further corrected ind and Det variable definitions to more accurately use
% the subpixel values of the new setup. -SFK
ind0 = find(Data(:,1)>NumSubStrips*3);
ind1 = find(Data(:,2)<=NumSubStrips);
Det0 = Data(ind0,:);
Det1 = Data(ind1,:);
Det1(:,1) = Det1(:,1)-NumSubStrips;
Det0(:,2) = Det0(:,2)-NumSubStrips*2;
Det0(:,1) = Det0(:,1)-NumSubStrips*3;

% Filter outermost strips from data because they do not have a physical
% momentum
ind00 = find(Det0(:,1)<76 & Det0(:,1)>5);
Det0=Det0(ind00,:);
ind00 = find(Det0(:,2)<76 & Det0(:,2)>5);
Det0=Det0(ind00,:);
ind11 = find(Det1(:,1)<76 & Det1(:,1)>5);
Det1=Det1(ind11,:);
ind11 = find(Det1(:,2)<76 & Det1(:,2)>5);
Det1=Det1(ind11,:);

% Creates Distance Vector of the center of each subpixel based on the total
% number of subpixels for a single face of the detector
[ThetaRefX] = SubPixelCenters(subsperpixel,stripwidth,gapwidth,NumSubStrips,0);
[ThetaRefY] = SubPixelCenters(subsperpixel,stripwidth,gapwidth,NumSubStrips,0);

% Creates Distance Vector that defines the edges of the subpixels to be
% used for the histogram plots
[DetectDistRef] = SubPixelEdges(subsperpixel,stripwidth,gapwidth,NumSubStrips);
DetectDistRef = DetectDistRef(subsperpixel+2:end-(subsperpixel+1));
UsableDetectDist = cell(1,2);
UsableDetectDist{1} = DetectDistRef;
UsableDetectDist{2} = DetectDistRef;

% % Detector 0

Det0(:,1) = ThetaRefX(Det0(:,1)); %AC subpixel
Det0(:,2) = ThetaRefY(Det0(:,2)); %DC subpixel

% % Detector 1

Det1(:,1) = ThetaRefX(Det1(:,1)); %AC subpixel
Det1(:,2) = ThetaRefY(Det1(:,2)); %DC subpixel

% Creates a histogram of the number of counts in each subpixel of each detector.
Det0Res = hist3(Det0(:,1:2), 'Edges', UsableDetectDist);
Det1Res = hist3(Det1(:,1:2), 'Edges', UsableDetectDist);

```

```

% Creates a mask of 1's and 0's that determines what pixels to use from the
% detector response histograms
mask = PHDsMask(size(Det0Res), subsperpixel);

% Masks the subpixels that are not desired from the detector response
% histograms.
Det0Res = Det0Res.*mask;
Det1Res = Det1Res.*mask;

% Saves the masked detector response histogram and the mask file to be used
% by ThreeDPASSCalc3.m
save([pwd '/Detector0EfficiencyCounts.mat'],'Det0Res');
save([pwd '/Detector1EfficiencyCounts.mat'],'Det1Res');
save([pwd '/DetectorMask_' num2str(subsperpixel) '.mat'],'mask');

Det0Res = EffNormCalc(Det0Res,subsperpixel);
Det1Res = EffNormCalc(Det1Res,subsperpixel);

save([pwd '/Detector0NormalizedEfficiency.mat'],'Det0Res');
save([pwd '/Detector1NormalizedEfficiency.mat'],'Det1Res');

if plotind
figure('Color','w','OuterPosition',[12 660 1400 560]);
subplot(1,2,1); pcolor(DetectDistRef,DetectDistRef,Det0Res);
title('Detector0 - Response');
shading flat; xlabel('Vertical Axis [mm]'); ylabel('Beam Axis [mm]');
colorbar;axis square;
caxis([0 1]);
colormap hot;

subplot(1,2,2); pcolor(DetectDistRef,DetectDistRef,Det1Res);
title('Detector1 - Response');
shading flat; xlabel('Vertical Axis [mm]'); ylabel('Beam Axis [mm]');
colorbar;axis square;
caxis([0 1]);

figure('Color','w','OuterPosition',[12 100 1400 560]);
subplot(1,2,1); pcolor(DetectDistRef,DetectDistRef,Det0Res);
title('Detector0 - Response');
shading flat; xlabel('Vertical Axis [mm]'); ylabel('Beam Axis [mm]');
colorbar;axis square;
caxis([0 1]);
colormap jet;

subplot(1,2,2); pcolor(DetectDistRef,DetectDistRef,Det1Res);
title('Detector1 - Response');
shading flat; xlabel('Vertical Axis [mm]'); ylabel('Beam Axis [mm]');
colorbar;axis square;
caxis([0 1]);
end
end

```

Matlab Combined ACAR / DBAR Calculation:

```

%%% Simultaneous 2D-ACAR and CDBAR Experiment Data Analysis tool for 3DPASS
%%% using AFRL Vacuum Chamber and two PHDs high purity germanium (HPGe)
%%% 16x16 double sided strip detectors (DSSDs) that also corrects for
%%% subpixel efficiencies using average relative efficiency matrices that
%%% come from ThreeDPASSEfficiencyCalc.m
%%% Created on 12 Dec 2011 by smj
%%% Modifications:
%%% - 13 Nov 2012 by SFK and AMB; accounted for having detector 1 flipped
%%% around and having cables swapped

```

```

%%% -28 DEC 2012 by SFK, changed values in filtering of nonreal pixels to
%%% match detector setup
%%% Based on Williams Dissertation Section 4.9 Simultaneous 2D ACAR and
%%% CDBAR Experiment

function ThreeDPASSCalc3(Data, EwinCent, deltaE, timemax, DetectSourceDist, subsperpixel)
% % User Inputs
% Data - Parsed file output from Spec72Parser_RawEventv2.m or from
%       Spec72Parser_WinEvent.m with the following formats as of 12 Dec
%       2011: Raw Format = [D0 AC Pixel, D0 DC Pixel, D0 Energy, D1 AC
%       Pixel, D1 DC Pixel, D1 Energy, Time Stamp (number of 20ns ticks)]
%       Win Format = [D0 AC Pixel, D0 DC Pixel, D0 Energy, D1 AC
%       Pixel, D1 DC Pixel, D1 Energy]
% EwinCent - Center of Energy Window (keV) desired
% deltaE - +/- of Center of Energy Window (keV)
% timemax - number of 20ns time intervals to limit data.
% DetectSourceDist - distance to each detector in m
% subsperpixel - how many subpixels to use in the program

% load(['pwd '/Cu_Align_5DECC2140_RawEvent_4.phdRaw_Data_Parsed_on_07-Dec-2012.mat']);
%
% EwinCent=511;
% deltaE=15;
% timemax=4;
% DetectSourceDist=2.0;
% subsperpixel=5;

%% 2D-ACAR Calculation

NumSubStrips = subsperpixel*16;
stripwidth = 4.75; % PHDs DSSD strip width in mm
gapwidth = 0.25; % PHDs DSSD gap width in mm

% Filter data to include only specific energies
ind = find(Data(:,3)>=(EwinCent-deltaE) & Data(:,3)<=(EwinCent+deltaE));
Data = Data(ind,:);

% Filter data to include only time differences
indt=find(Data(:,7)<=timemax);
Data = Data(indt,:);

% Filter outermost strips from data because they do not have a physical
% momentum
%This removes exactly one strip from each of the four edges -SFK
%Changed filter values to match new detector setup. -SFK
ind = find(Data(:,1)~=NumSubStrips*3+subsperpixel &
Data(:,2)~=NumSubStrips*2+subsperpixel & Data(:,4)~=NumSubStrips+subsperpixel &
Data(:,5)~=subsperpixel & Data(:,1)~=NumSubStrips*4-subsperpixel+1 &
Data(:,2)~=NumSubStrips*3-subsperpixel+1 & Data(:,4)~=NumSubStrips*2-subsperpixel+1 &
Data(:,5)~=NumSubStrips-subsperpixel+1);
Data = Data(ind,:);

% Creates Distance Vector of the center of each subpixel based on the total
% number of subpixels for a single face of the detector
[ThetaRefX0] = SubPixelCenters(subsperpixel, stripwidth, gapwidth, NumSubStrips, 0);
[ThetaRefX1] = SubPixelCenters(subsperpixel, stripwidth, gapwidth, NumSubStrips, 0);
[ThetaRefY0] = SubPixelCenters(subsperpixel, stripwidth, gapwidth, NumSubStrips, 0);
[ThetaRefY1] = SubPixelCenters(subsperpixel, stripwidth, gapwidth, NumSubStrips, 0);

% Creates Distance Vector that defines the edges of the subpixels to be
% used for the histogram plots
[DetectDistRef] = SubPixelEdges(subsperpixel, stripwidth, gapwidth, NumSubStrips);
DetectDistRef = DetectDistRef(subsperpixel+2:end-(subsperpixel+1));
DetectDistAvg = (DetectDistRef(2:end)+DetectDistRef(1:end-1))/2;
UsableDetectDist = cell(1,2);
UsableDetectDist{1} = DetectDistRef;
UsableDetectDist{2} = DetectDistRef;

% Creates Vector which defines the edge bins for the Deviation from colinearity
% of the coincident gamma rays to be used for the histogram plots

```

```

SubPixelRes = (stripwidth+gapwidth)/subspixel/DetectSourceDist;
% % Subpixel Angular not accounting for the 0.25mm gap in [mrad]
DevColinRef = min((DetectDistRef-
gapwidth/2)/DetectSourceDist)*2:SubPixelRes:max((DetectDistRef+gapwidth/2)/DetectSourceDist)*2;
DevColinEdges = cell(1,2);
DevColinEdges{1} = DevColinRef;
DevColinEdges{2} = DevColinRef;

% Load and Format Masked Efficiency Count Matricies
% % one for each detector
% load([pwd '/Detector0EfficiencyCounts.mat']);
% load([pwd '/Detector1EfficiencyCounts.mat']);
% load([pwd '/Detector0EfficiencyCounts_Sr.mat']);
% load([pwd '/Detector1EfficiencyCounts_Sr.mat']);
load([pwd '/Detector0NormalizedEfficiency.mat']);
load([pwd '/Detector1NormalizedEfficiency.mat']);
% load([pwd '/Detector0WilliamsEfficiency.mat']);
% load([pwd '/Detector1WilliamsEfficiency.mat']);

indr = subspixel+1:subspixel+1:(subspixel+1)*14;
Det0Temp = removerows(Det0Res,indr);
Det0Temp = removerows(Det0Temp',indr)';
Det1Temp = removerows(Det1Res,indr);
Det1Temp = removerows(Det1Temp',indr)';

% Load and Format mask file to analyze data
% % if one doesn't exist for the number of subpixels, then one is created
try
    load([pwd '/DetectorMask_' num2str(subspixel) '.mat']);
catch
    mask = PHDsMask(size(Det0Res), subspixel);
end
maskTemp = removerows(mask,indr);
maskTemp = removerows(maskTemp',indr)';

% Apply Mask to Filter Eff Data
Det0Temp = Det0Temp.*maskTemp;
Det1Temp = Det1Temp.*maskTemp;

% Try to see if there is a difference in mean, mode, and max evaluation
% Mean method
% MaskFactor = sum(sum(maskTemp));
% EffFactor0 = sum(sum(Det0Temp))/MaskFactor;
% EffFactor1 = sum(sum(Det1Temp))/MaskFactor;
% % Mean method times number of strips
%
% % Max method
% EffFactor0 = max(max(Det0Temp));
% EffFactor1 = max(max(Det1Temp));
%
% Det0Temp = Det0Temp./EffFactor0; %% tested to see if mask then efficiency calc matters.
% Det1Temp = Det1Temp./EffFactor1;

% Format and Assign relative efficiencies to Coincident events
Det0Eff = zeros(NumSubStrips,NumSubStrips);
Det1Eff = zeros(NumSubStrips,NumSubStrips);
Det0Eff(subspixel+1:NumSubStrips-subspixel,subspixel+1:NumSubStrips-
subspixel) = Det0Temp;
Det1Eff(subspixel+1:NumSubStrips-subspixel,subspixel+1:NumSubStrips-
subspixel) = Det1Temp;
RelEffs = zeros(size(Data,1),2);
%for n = 1:size(Data,1)
%    RelEffs(n,1) = Det0Eff(Data(n,1),Data(n,2)-NumSubStrips);
%    RelEffs(n,2) = Det1Eff(Data(n,4)-NumSubStrips*2,Data(n,5)-NumSubStrips*3);
%end
%This loop above was changed below to represent the new detector setup, with the format:
% Det0Eff(DC subpixel, AC subpixel) for (row, column) -SFK
for n = 1:size(Data,1)
    RelEffs(n,1) = Det0Eff(Data(n,2)-NumSubStrips*2,Data(n,1)-NumSubStrips*3);

```

```

        RelEffs(n,2) = Det1Eff(Data(n,5),Data(n,4)-NumSubStrips);
    end
    % % % X-Direction (AC Direction)
    % % % % Positive X Direction is from the center of the detector faces towards
    % the side of the room where the positron beam is located.
    % Swapped XTheta0 and XTheta1, since detector cords got swapped.- AMB
    % Data(:,1) is AC on Det1, Data(:,4) is AC on Det0 (higher channels)
    XTheta0 = ThetaRefX0(Data(:,1)-NumSubStrips*3);
    XTheta1 = -ThetaRefX1(Data(:,4)-NumSubStrips);
    figure('Color','w','OuterPosition',[570 600 600 500]);
    subplot(2,1,1);
    ncount = histc(XTheta0,DetectDistRef); bar(DetectDistRef, ncount, 'histc');
    title('Detector0 - Horizontal Axis');
    xlabel('Distance from Center of Crystal, [mm]');
    ylabel('Counts, [#]');
    subplot(2,1,2); ncount = histc(XTheta1,DetectDistRef); bar(DetectDistRef, ncount,
    'histc');
    title('Detector1 - Horizontal Axis');
    xlabel('Distance from Center of Crystal, [mm]');
    ylabel('Counts, [#]');

    figure('Color','w','OuterPosition',[570 600 600 500]);
    subplot(2,1,1);
    [ncount ncounteff] = histldw(XTheta0,DetectDistRef,RelEffs(:,1));
    bar(DetectDistAvg,ncounteff,'histc'); title('Detector0 - Horizontal (Beam) Axis');
    xlabel('Distance from Center of Crystal, [mm]');
    ylabel('Counts, [#]');
    subplot(2,1,2); [ncount ncounteff] = histldw(XTheta1,DetectDistRef,RelEffs(:,2));
    bar(DetectDistAvg,ncounteff,'histc'); title('Detector1 - Horizontal (Beam) Axis');
    xlabel('Distance from Center of Crystal, [mm]');
    ylabel('Counts, [#]');

    % % % Y-Direction (DC Direction)
    % % % % Positive DC Direction is from Center of either DSSD toward the table,
    % % on which the detectors are resting.
    % Corrected YThetas for current cord configuration. SFK
    YTheta0 = ThetaRefY0(Data(:,2)-NumSubStrips*2);
    YTheta1 = ThetaRefY1(Data(:,5));
    figure('Color','w','OuterPosition',[570 100 600 500]);
    subplot(2,1,1);
    ncount = histc(YTheta0,DetectDistRef); bar(DetectDistRef, ncount, 'histc');
    title('Detector0 - Vertical Axis');
    xlabel('Distance from Center of Crystal, [mm]');
    ylabel('Counts, [#]');
    subplot(2,1,2); ncount = histc(YTheta1,DetectDistRef); bar(DetectDistRef, ncount,
    'histc');
    title('Detector1 - Vertical Axis');
    xlabel('Distance from Center of Crystal, [mm]');
    ylabel('Counts, [#]');

    figure('Color','w','OuterPosition',[570 100 600 500]);
    subplot(2,1,1);
    [ncount ncounteff] = histldw(YTheta0,DetectDistRef,RelEffs(:,1));
    bar(DetectDistAvg,ncounteff,'histc'); title('Detector0 - Vertical Axis');
    xlabel('Distance from Center of Crystal, [mm]');
    ylabel('Counts, [#]');
    subplot(2,1,2); [ncount ncounteff] = histldw(YTheta1,DetectDistRef,RelEffs(:,2));
    bar(DetectDistAvg,ncounteff,'histc'); title('Detector1 - Vertical Axis');
    xlabel('Distance from Center of Crystal, [mm]');
    ylabel('Counts, [#]');

    % % % Coincident Response from the detectors
    figure('Color','w','OuterPosition',[12 100 560 1000]);
    subplot(2,1,1); hist3([XTheta0 YTheta0], [14 14]);
    title('Detector0 - Coincident Response');
    shading flat; xlabel('Horizontal Axis [mm]'); ylabel('Vertical Axis [mm]');
    set(gcf,'renderer','opengl');
    view(gca,[90 90]); colorbar; axis([-35 35 -35 35]);
    set(get(gca,'child'),'FaceColor','interp','CDDataMode','auto');

```

```

subplot(2,1,2); hist3([XTheta1 YTheta1], [14 14]);
title('Detector1 - Coincident Response');
shading flat; xlabel('Horizontal Axis [mm]'); ylabel('Vertical Axis [mm]');
set(gcf,'renderer','opengl');
set(get(gca,'child'),'FaceColor','interp','CDataMode','auto');
view(gca,[90 90]); colorbar; axis([-35 35 -35 35]);

figure('Color','w','OuterPosition',[12 100 560 1000]);
subplot(2,1,1); hist3([XTheta0 YTheta0], 'Edges', UsableDetectDist);
title('Detector0 - Coincident Response');
shading flat; xlabel('Horizontal Axis [mm]'); ylabel('Vertical Axis [mm]');
set(gcf,'renderer','opengl');
view(gca,[90 90]); colorbar; axis([-35 35 -35 35]);
set(get(gca,'child'),'FaceColor','interp','CDataMode','auto');
subplot(2,1,2); hist3([XTheta1 YTheta1], 'Edges', UsableDetectDist);
title('Detector1 - Coincident Response');
shading flat; xlabel('Horizontal Axis [mm]'); ylabel('Vertical Axis [mm]');
set(gcf,'renderer','opengl');
set(get(gca,'child'),'FaceColor','interp','CDataMode','auto');
view(gca,[90 90]); colorbar; axis([-35 35 -35 35]);

Det0 = hist3([XTheta0 YTheta0], 'Edges', UsableDetectDist);
Det1 = hist3([XTheta1 YTheta1], 'Edges', UsableDetectDist);
Det0 = Det0.*mask;
Det1 = Det1.*mask;

figure('Color','w','OuterPosition',[570 100 560 1000]);
subplot(2,1,1); pcolor(DetectDistRef,DetectDistRef,Det0);
title('Detector0 - Masked Coincident Response');
shading flat; xlabel('Horizontal Axis [mm]'); ylabel('Vertical Axis [mm]');
colorbar;axis square;
caxis([0 35]);
subplot(2,1,2); pcolor(DetectDistRef,DetectDistRef,Det1);
title('Detector1 - Masked Coincident Response');
shading flat; xlabel('Horizontal Axis [mm]'); ylabel('Vertical Axis [mm]');
colorbar;axis square;
caxis([0 35]);

figure('Color','w','OuterPosition',[12 100 560 1000]);
subplot(2,1,1); pcolor(DetectDistRef,DetectDistRef,Det0./Det0Res);
title('Detector0 - Coincident Response');
shading flat; xlabel('Horizontal Axis [mm]'); ylabel('Vertical Axis [mm]');
colorbar;axis square;
caxis([0 1.5]);
subplot(2,1,2); pcolor(DetectDistRef,DetectDistRef,Det1./Det1Res);
title('Detector1 - Coincident Response');
shading flat; xlabel('Horizontal Axis [mm]'); ylabel('Vertical Axis [mm]');
colorbar;axis square;
caxis([0 1.5]);

%% Deviation from Colinearity

% Changed as suggested by smj, Neg in ThetaX calc for flipping Detector 1 around - AMB
% Left + sign in for ThetaX, instead placed a minus sign where XTheta1 is
% defined above -SFK

ThetaX = (XTheta0+XTheta1)/DetectSourceDist;
ThetaY = (YTheta0+YTheta1)/DetectSourceDist;
ACARData = [ThetaX ThetaY];

figure('Color','w','OuterPosition',[1170 100 600 500]); subplot(2,1,1);
ncount = histc(ThetaX,DevColinRef); bar(DevColinRef,ncount,'histc');
title('Horizontal Axis - Both Detectors');
xlabel('Deviation from Colinearity, [mrad]');
subplot(2,1,2); ncount = histc(ThetaY,DevColinRef); bar(DevColinRef,ncount,'histc');
title('Vertical Axis - Both Detectors');
xlabel('Deviation from Colinearity, [mrad]');
ylabel('Counts, [#]');

figure('Color','w','OuterPosition',[1170 100 600 500]); subplot(2,1,1);

```

```

DevColinAvg = (DevColinRef(2:end)+DevColinRef(1:end-1))./2;
[nccount, ncounteff] = hist1dw(ThetaX,DevColinRef,RelEffs(:,1).*RelEffs(:,2));
bar(DevColinAvg,ncounteff,'histc');
title('Horizontal Axis - Both Detectors');
xlabel('Deviation from Colinearity w/ Efficiency Correction, [mrad]');
subplot(2,1,2); [nccount, ncounteff]=
hist1dw(ThetaY,DevColinRef,RelEffs(:,1).*RelEffs(:,2));
bar(DevColinAvg,ncounteff,'histc');
title('Vertical Axis - Both Detectors');
xlabel('Deviation from Colinearity w/ Efficiency Correction, [mrad]');
ylabel('Counts, [#]');

figure('Color','w','OuterPosition',[1170 600 600 528]);
hist3(ACARData,'Edges',DevColinEdges);
ACARCount = hist3(ACARData,'Edges',DevColinEdges);
title('ACAR Deviation from Colinearity');
shading flat; xlabel('\theta [mrad]'); ylabel('Vertical Axis
{\theta} [mrad]');
set(gcf,'renderer','opengl');
set(get(gca,'child'),'FaceColor','interp','CDataMode','auto');
view(gca,[90 90]); colorbar; axis([-35 35 -35 35]);
caxis([0 35]);

[ACARCount2, ACARDatawEff] = hist2dw(ACARData,DevColinRef,DevColinRef,RelEffs);
figure('Color','w','OuterPosition',[1170 600 600 528]);
pcolor(DevColinAvg, DevColinAvg, ACARDatawEff);
shading flat; colorbar; axis([-35 35 -35 35]);
title('ACAR Deviation from Colinearity w/ Efficiency Correction');
xlabel('Horizontal (Beam) Axis {\theta} [mrad]'); ylabel('Vertical Axis {\theta}
[mrad]');
caxis([0 700]);

ind = find(RelEffs(:,1)~=0 & RelEffs(:,2)~=0);
RelEffsFilt = RelEffs(ind,:);
ACARDataFilt = ACARData(ind,:);
[ACARCount2Filt, ACARDatawEffFilt] =
hist2dw(ACARDataFilt,DevColinRef,DevColinRef,RelEffsFilt);
figure('Color','w','OuterPosition',[1170 100 600 500]);
DevColinAvg = (DevColinRef(2:end)+DevColinRef(1:end-1))./2;
pcolor(DevColinAvg, DevColinAvg, ACARDatawEffFilt);
shading flat; colorbar; axis([-35 35 -35 35]);
title('ACAR Deviation from Colinearity w/ Efficiency Correction & Filtered Pixels');
xlabel('Horizontal (Beam) Axis {\theta} [mrad]'); ylabel('Vertical Axis {\theta}
[mrad]');
caxis([0 700]);
%% CDBAR Calculation
EnergyRes = 0.9;

Evec = (EwinCent-deltaE):EnergyRes:(EwinCent+deltaE);
EvecAvg = (Evec(2:end)+Evec(1:end-1))./2;
EvecCell = cell(1,2);
EvecCell{1} = Evec;
EvecCell{2} = Evec;
DBARData = [Data(:,3) Data(:,6)];

figure('Color','w','OuterPosition',[1770 100 600 500]);
subplot(2,1,1);
nccount = histc(Data(:,3),Evec); bar(Evec,nccount,'histc');
title('Detector0 - Energy Plot');
xlabel('Energy, [keV]');
ylabel('Counts, [#]');
subplot(2,1,2);
nccount = histc(Data(:,6),Evec); bar(Evec,nccount,'histc');
title('Detector1 - Energy Plot');
xlabel('Energy, [keV]');
ylabel('Counts, [#]');

figure('Color','w','OuterPosition',[1770 100 600 500]);
subplot(2,1,1);

```



```

[nccount, ncounteff] = histldw(Data(:,3),Evec,RelEffs(:,1));
bar(EvecAvg,ncounteff,'histc');
title('Detector0 - Energy Plot w/ Efficiency Correction');
xlabel('Energy, [keV]');
ylabel('Counts, [#]');
subplot(2,1,2);
[nccount, ncounteff] = histldw(Data(:,6),Evec,RelEffs(:,2));
bar(EvecAvg,ncounteff,'histc');
title('Detector1 - Energy Plot w/ Efficiency Correction');
xlabel('Energy, [keV]');
ylabel('Counts, [#]');

figure('Color','w','OuterPosition',[1770 600 600 528]);
hist3(DBARData, EvecCell);
title('Raw DBAR Results for both Detectors');
xlabel('Energy Detector 0 [keV]'); ylabel('Energy Detector 1 [keV]');
%set(gcf,'renderer','opengl');
shading flat;
set(get(gca,'child'),'FaceColor','interp','CDataMode','auto');
view(gca,[90.5 90]); colorbar; axis([500 522 500 522]);
caxis([0 10]);

[DBARCount, DBARDatawEff] = hist2dw(DBARData, Evec, Evec,RelEffs);
figure('Color','w','OuterPosition',[1770 600 600 528]);
pcolor(EvecAvg,EvecAvg,DBARDatawEff); shading flat; colorbar;
shading flat; colorbar; axis square;
title('DBAR Energy Plot w Efficiency Correction');
xlabel('Energy Detector 0 [keV]'); ylabel('Energy Detector 1 [keV]');
caxis([0 1200]);

DBARDataFilt = DBARData(ind,:);
[DBARCount2Filt, ACARDatawEffFilt] = hist2dw(DBARDataFilt,Evec, Evec,RelEffsFilt);
figure('Color','w','OuterPosition',[1770 100 600 500]);
pcolor(EvecAvg,EvecAvg,DBARDatawEff); shading flat; colorbar;
shading flat; colorbar; axis square;
title('DBAR Energy Plot w Efficiency Correction & Filtered Pixels');
xlabel('Energy Detector 0 [keV]'); ylabel('Energy Detector 1 [keV]');
caxis([0 1200]);

delta = 4; %half-width of 45 degree swath across DBAR plot

DBARDataFilt(:,3) = RelEffsFilt(:,1).*RelEffsFilt(:,2);
DBARDataFilt(:,4) = DBARDataFilt(:,1)+DBARDataFilt(:,2)-1022;
DBARDataFilt(:,5) = DBARDataFilt(:,1)-DBARDataFilt(:,2);
indE = find(DBARDataFilt(:,4)>=-delta & DBARDataFilt(:,4)<=delta);
DBARDataEFilt = DBARDataFilt(indE,:);

EvecLine = Evec-511;
[DBARCountLine, DBARCountLinewEff] =
histldw(DBARDataEFilt(:,5),EvecLine,DBARDataEFilt(:,3));
EvecLine = (EvecLine(2:end)+EvecLine(1:end-1))/2;
figure('Color','w','OuterPosition',[1770 600 600 528]);
semilogy(EvecLine,DBARCountLine,'-k',EvecLine,DBARCountLinewEff,'-b')
%plot(EvecLine,DBARCountLine,'-k')
axis([min(EvecLine) max(EvecLine) 0 160000]);
title('Correlated DBAR for {\Delta}=4 keV Swath, 0.9 keV Bin Resolution');
ylabel('Counts'); xlabel('Difference in Energy, [keV]');

end

```

Appendix D: Equipment and Source Data

Specific Equipment Used

Item	Make	Model	Part Number	Serial Number
Vacuum Pump	Pfeiffer	HiCube HiPace 80 Eco Pump	PM P03 941	15126337
Vacuum Gauge Controller	Varian	XGS-600	XGS600H0M1C1	LI1109L512

Radioactive Sources Available

Source	Original Number	AFIT Designation	Nominal Activity	Assay Date
⁸⁵ Sr	1613-11	T-145	100.8 µCi	July 2012
²² Na	B009	T-147	1.0 mCi	10 January 2012
²² Na	B008	T-146	100 µCi	10 January 2012
²² Na	115163	T-149	30 µCi	1 October 2007
²² Na	115162	T-148	20.5 µCi	1 October 2007
²² NaCl	CuSS	T-141	23.3 µCi	18 January 2012

Appendix E: Additional Information on Positron Beam

Positron Beam

Although the current system allows only passive positron spectroscopy by placing the positron source right next to the sample of interest, soon the active method of using the positron beam to send a large flux of positrons directly onto the sample will be operational, once the beam setup is completed. The low-energy positron beam system produced by First Point Scientific, Inc. utilizes a Penning-Malmberg moderator-trap [21]. The assembly consists of the positron source and moderator system (RGM-1), the advanced positron beam source (APBS), associated support electronics, and LabView control software.

Placing a high-activity ^{22}Na source inside the beam generator allows for creation of positrons as long as the source retains a sufficient level of activity for the strength of the beam that is required. The positron beam generates a high flux beam of low-energy (<50 eV), focused positrons on a sample material inside the target vacuum chamber [22]. The beam's ^{22}Na source is 50 mCi which can provide a pulsed positron flux of 8 million particles per second. The relatively short half-life of ^{22}Na (2.6 years) gives it a high specific activity, which means that its actual radiation output is high per unit of activity as compared to isotopes with longer half-lives.

The beam source and moderator system (RGM-1) uses a two-stage cold head (cryopump which traps vapors by condensing them on a cold surface) to grow a solid neon moderator on the surface of a cone near the source. The solid neon moderator, grown in 20 minutes via computer control, has a moderation efficiency of 1%. After moderation, the positron beam is magnetically transported to the advanced positron beam

source (APBS) where it is cooled and trapped. The APBS uses N₂ as a buffer gas and SF₆ as a cooling gas. Proper trapping and guiding of the beam, along with a good vacuum and very quick beam generation and manipulation allow a useful number of positrons to make it out of the beam exit prior to annihilation.

The entire experiment is kept under high vacuum in order to allow for deep cooling of the gases involved and for generation and transport of the positrons. Cryopumps are used to keep the system cold (20-40 K) and the pressure very low (10⁻⁸ Torr), which is close to ultra-high vacuum (UHV) (UHV is lower than about 10⁻⁹ Torr). The positron beam enters the target chamber through one of the 4-in openings perpendicular to the detector axis. Two large Helmholtz coils surrounding the target chamber on opposite sides create a magnetic trap for the positrons near the center of the chamber. The positrons are guided towards the location of the sample using this trap.

Bibliography

- [1] Swinney, M.W., McClory, J.W., Petrosky, J.C., Yang, S., Brant, A.T., Adamiv, V.T., Burak, Y. V., Dowben, P.A., and Halliburton, L.E. "Identification of electron and hole traps in lithium tetraborate ($\text{Li}_2\text{B}_4\text{O}_7$) crystals: Oxygen vacancies and lithium vacancies." *Journal of Applied Physics*, 107(11):113715-113715-9, (2010).
- [2] Williams, C. S., Burggraf, L.W., Adamson, P.E., Petrosky, J.C. "Three-dimensional Electron-Positron Momentum Distribution Of O^{3+} -Irradiated 6H SiC Using Two Positron Spectroscopy Techniques Simultaneously." *Journal of Physics: Conference Series*, 2011, Vol 262, 012064, 1-5.
- [3] Williams, Christopher S. "Three Dimensional Positron Annihilation Momentum Measurement Technique Applied to Measure Oxygen-Atom Defects in 6H Silicon Carbide." AFIT PhD Dissertation. AFIT/DS/ENP/10-M02, (Mar 2010)
- [4] Charlton, M., and Humberston, J.W. *Positron Physics*. Cambridge Monographs on Atomic, Molecular, and Chemical Physics. Cambridge, U.K.: Cambridge University Press, 2001, p. 264.
- [5] Krause-Rehberg, Reinhard and Hartmut S. Leipner. *Positron Annihilation in Semiconductors*. Springer, 1999.
- [6] PALS Tutorial. Nanopos: University of Michigan Positron Research Website. <http://positrons.physics.lsa.umich.edu/current/nanopos/PALS-intro/psitronphysics.htm> Accessed 6 Mar 2013.
- [7] Chehab, R. "Positron sources." Cern European Organization For Nuclear Research-Reports-Cern, 643, 1994.
- [8] University of Toronto. Environmental Health and Safety. <http://www.ehs.utoronto.ca/services/radiation/radtraining/nuclideinformation.htm> Accessed 27 Dec 2012.
- [9] Jean, Y.C., Mallon, P.E., and Schrader, D.M. *Principles and Applications of Positron and Positronium Chemistry*. Singapore: World Scientific Publishing Co., 2003, pp. 185–189.
- [10] McKelvey, John P. *Solid State Physics for Engineering and Materials Science*. Malabar, Florida: Krieger Publishing Company, 1993.
- [11] Amarendra, G., Baldev Raj, and Manghnani, M.H., Eds. *Advances in Materials Characterization*. Hyderabad: Universities Press, 2007.
- [12] Holmes-Siedle, Andrew, and Adams, Len. *Handbook of Radiation Effects*. 2nd Ed. New York: Oxford University Press, 2007.

- [13] Holbert, Keith E. "Radiation Effects and Damage." Arizona State University: Course notes for EEE 560.
<http://holbert.faculty.asu.edu/eee560/RadiationEffectsDamage.pdf> Accessed 6 Jan 2013.
- [14] Buchanan, Douglas A. "EPR and ENDOR Studies of Point Defects in Lithium Tetraborate." AFIT PhD Dissertaion. AFIT/DS/ENP/12-11, (Dec 2012)
- [15] Corradi, G., Nagirnyi, V., Kotlov, A., Watterich, A., Kirm, M., Polgar, K., Hofstaetter, A., and Meyer, M. "Investigation of Cu-doped $\text{Li}_2\text{B}_4\text{O}_7$ single crystals by electron paramagnetic resonance and time-resolved optical spectroscopy," *Journal of Physics: Condensed Matter*, 20, 025216 (2008).
- [16] Kananen, B. E., Brant, A.T., Buchanan, D.A., Murari, M.K., McClory, J. W. "Analysis of Neutron Induced Defects in Silver Doped Lithium Tetraborate", 2011 IEEE Nuclear Science Symposium Conference Record, NP1.M-212, 427-430.
- [17] Adamson, Paul E. "Quantum Mechanical Prediction of Experimental Observables of Positron-Vacancy Complexes in Silicon Carbide." Ph.D. dissertation, Air Force Institute of Technology, 2005.
- [18] Jimenez, Stephen M. "Design and Characterization of the Three-Dimensional Positron Annihilation Spectroscopy System using a Low Energy Positron Beam", AFIT Thesis, 2012.
- [19] Kruseman, A.C. *Two-Dimensional ACAR and Low-Background DBAR Studies on Materials with Defects*. Delft, The Netherlands: Delft University of Technology, 1999.
- [20] Baranowski, A., J. Beliczynski, M. Kostrzewa, and M. Szuszkiewicz. "A two detector spectrometer for measurements of Doppler broadened positron annihilation spectra". *Nuclear Instruments and Methods in Physics Research Section A: Accelerators, Spectrometers, Detectors and Associated Equipment*, 526(3):420-431, 2004.
- [21] Surko, C., and Greaves, R. "A multicell trap to confine large numbers of positrons" *La Jolla: Radiation Physics and Chemistry*, 2003, Vol. 68. 419-425.
- [22] Greaves, R. G. and Surko, C. M. "Technological applications of trapped positrons". *AIP Conference Proceedings*, 19-28. IOP INSTITUTE OF PHYSICS PUBLISHING LTD, 1999.

Vita

Stefan B. Fagan-Kelly was born in Queens, New York and grew up in Brooklyn and Amityville, New York. After graduating from St. Francis Xavier High School in Manhattan, he attended the United States Air Force Academy in Colorado Springs, Colorado and graduated with the class of 2009 with a Bachelor of Science in Physics with a concentration in Space Physics and Astronomy, and a minor in German. He then proceeded to work for the Space Vehicles Directorate of the Air Force Research Laboratory at Hanscom Air Force Base, Massachusetts, contributing to research in Cold Atom Navigation and Laser Cooling. He is currently a Master's student studying Nuclear Engineering at the Air Force Institute of Technology at Wright-Patterson Air Force Base, Ohio. His next projected assignment is with the Air Force Technical Applications Center at Patrick Air Force Base, Florida.

REPORT DOCUMENTATION PAGE			<i>Form Approved OMB No. 074-0188</i>		
<p>The public reporting burden for this collection of information is estimated to average 1 hour per response, including the time for reviewing instructions, searching existing data sources, gathering and maintaining the data needed, and completing and reviewing the collection of information. Send comments regarding this burden estimate or any other aspect of the collection of information, including suggestions for reducing this burden to Department of Defense, Washington Headquarters Services, Directorate for Information Operations and Reports (0704-0188), 1215 Jefferson Davis Highway, Suite 1204, Arlington, VA 22202-4302. Respondents should be aware that notwithstanding any other provision of law, no person shall be subject to any penalty for failing to comply with a collection of information if it does not display a currently valid OMB control number.</p> <p>PLEASE DO NOT RETURN YOUR FORM TO THE ABOVE ADDRESS.</p>					
1. REPORT DATE (DD-MM-YYYY) 21-03-2013		2. REPORT TYPE Master's Thesis		3. DATES COVERED (From - To) 20 Jun 2011 - 21 Mar 2013	
4. TITLE AND SUBTITLE Three Dimensional Positron Annihilation Momentum Spectroscopy Of Lithium Tetraborate Crystals			5a. CONTRACT NUMBER		
			5b. GRANT NUMBER		
			5c. PROGRAM ELEMENT NUMBER		
6. AUTHOR(S) Fagan-Kelly, Stefan B., First Lieutenant, USAF			5d. PROJECT NUMBER N/A		
			5e. TASK NUMBER		
			5f. WORK UNIT NUMBER		
7. PERFORMING ORGANIZATION NAMES(S) AND ADDRESS(S) Air Force Institute of Technology Graduate School of Engineering and Management (AFIT/EN) 2950 Hobson Way, Building 640 WPAFB OH 45433			8. PERFORMING ORGANIZATION REPORT NUMBER AFIT-ENP-13-M-09		
9. SPONSORING/MONITORING AGENCY NAME(S) AND ADDRESS(ES) Air Force Office of Scientific Research Dr. Michael R. Berman 875 North Randolph Street, Suite 325, Room 3112 Arlington VA 22203 Tel.: (703)696-7781, DSN: 426-7781, FAX: (703)696-7320, michael.berman@afosr.af.mil			10. SPONSOR/MONITOR'S ACRONYM(S) AFOSR / RSA		
			11. SPONSOR/MONITOR'S REPORT NUMBER(S)		
12. DISTRIBUTION/AVAILABILITY STATEMENT DISTRIBUTION STATEMENT A. APPROVED FOR PUBLIC RELEASE; DISTRIBUTION UNLIMITED.					
13. SUPPLEMENTARY NOTES					
14. ABSTRACT Previous endeavors in positron annihilation spectroscopy (PAS) at AFIT have resulted in the design and characterization of a second-generation three-dimensional positron annihilation momentum spectroscopy system (3DPAMSS) which combines two-dimensional angular correlation of annihilation radiation (2D ACAR) and coincident Doppler broadening of annihilation radiation (CDBAR) in order to measure electron momentum distributions in samples and thus characterize material defects. The focus of this particular research is to nondestructively measure negative defects in the crystal lattice of copper-doped, silver-doped, and undoped lithium tetraborate by 3DPAMSS spectroscopy using a Na-22 source and two high-purity germanium (HPGe) position-resolvable strip detectors. Lithium tetraborate is a candidate material for novel neutron detectors and characterizing its crystal structure is necessary to fully understand its properties. Several angular deviation and differential energy features are noted, which are translated to potential electron momentum distribution features and crystal defect characteristics.					
15. SUBJECT TERMS Positron Annihilation Spectroscopy, Lithium Tetraborate, ACAR, DBAR, Negative Defect Analysis, HPGe Strip Detectors, Thorium Oxide					
16. SECURITY CLASSIFICATION OF:			17. LIMITATION OF ABSTRACT	18. NUMBER OF PAGES	19a. NAME OF RESPONSIBLE PERSON
a. REPORT	b. ABSTRACT	c. THIS PAGE			19b. TELEPHONE NUMBER (Include area code)
U	U	U	UU	151	Burggraf, Larry, W., PhD (937) 255-3636, x 4507 (larry.burggraf@afit.edu)

Standard Form 298 (Rev. 8-98)
Prescribed by ANSI Std. Z39-18